Title
Flash Sintering of LaPO4-Al2O3 Ceramic Composites: Eutectic Microstructures and Sapphire Crystals

Author
Yang, Yingjie

Publication Date
2021

UNIVERSITY OF CALIFORNIA,
IRVINE

Flash Sintering of $LaPO_4$-Al_2O_3 Ceramic Composites: Eutectic Microstructures and Sapphire Crystals

DISSERTATION

submitted in partial satisfaction of the requirements
for the degree of

DOCTOR OF PHILOSOPHY

in Materials Science and Engineering

by

Yingjie Yang

Dissertation Committee:
Professor Martha L. Mecartney, Chair
Associate Professor Daniel R. Mumm
Assistant Professor Will J. Bowman
Assistant Professor Sarah Finkeldei

2021

DEDICATION

To my family

For lifting me up to see the world

To ZYB

For being my anchor and my light

TABLE OF CONTENTS

LIST OF FIGURES

LIST OF TABLES

ACKNOWLEDGEMENTS

I would like to express my greatest appreciation to my committee chair, Prof. Martha Mecartney. She shared with me her passion for science, excitement for teaching, and spirits of scholarship. It is my distinct honor to have her as my advisor, for without her support, guidance, and inspiration this dissertation would not have been possible.

Thank you to Prof. Mumm, for his encouragement, support and mentorship. He shared his knowledge of microscopy and materials science, as well as his love for the field. I appreciate greatly his insights and advising. I would also like to thank my committee members, Prof. Bowman and Prof. Finkeldei, for their support and insight on my research.

Special thanks to members of the Irvine Materials Research Institute, Dr. Zheng, Dr. Lin, Dr. Tran, Dr. Toshi Aoki, Dr. Liu, Dr. Li and Dr. Xu, they kindled my passion for microscopy/characterization, encouraged me, and supported my growth. Their expertise taught me my skills, but they have taught me so much more. It has been the greatest pleasure to work with the students and staff members at IMRI.

I would like to acknowledge Dr. Longsheng Feng, for collaborations on calculating the simulated phase diagrams, who wrote the Matlab program for finding the common tangent of the Gibbs free energies and plotted the simulated diagrams.

Thank you to all of my past and present peers in the Mecartney group, I had awesome mentors and great friends to support me throughout my journey, and I'm grateful for their patience, kindness and guidance.

I would also like to thank the faculty and staff members of the library and the Materials Science and Engineering Department, for their efforts and support.

Sincere thank you to my family and friends who have been by my side, for all you have done to support me.

Finally, thank you to the National Science Foundation for the funding provided throughout the course of my dissertation (Grant No. CMMI 1662791).

VITA

Education

PhD, Materials Science and Engineering, University of California, Irvine (UCI) 2021
MS, Materials Science and Engineering, University of California, Irvine 2017
B.Eng., Materials Science and Engineering, *Minor* in Media and Design
Shanghai Jiao Tong University (SJTU) 2016

Research Projects

Flash sintering of composites including Al_2O_3, $LaPO_4$ and 8 wt% Y_2O_3 stabilized ZrO_2

Graduate student researcher at UCI 2017-2021

Advisors: Prof. Martha L. Mecartney and Prof. Daniel R. Mumm

- Eutectic composition of Al_2O_3 and $LaPO_4$ was discovered and characterized
- Studied the processing-microstructure-property relationship of multi-phase ceramics with electrical-current assisted sintering – flash sintering
- Explored the interfacial energy, orientation relationships, and mechanical properties of the different structures

Thermal conductivity and mechanical properties of high entropy rare-earth zirconates and monazites

Graduate student researcher at UCI 2020-2021

Advisors: Prof. Martha L. Mecartney and Prof. Daniel R. Mumm

- Acquired and analyzed data to characterize the phase separation and elemental distributions

Professional Experience

Analytical characterization of material structures and properties

Lab assistant at the Irvine Materials Research Institute (IMRI) at UCI 2018-2021

Supervisors: Jian-Guo Zheng, Toshihiro Aoki, Qiyin Lin, Ich Tran, and Xiaofeng Liu

- Conducted micron- to nano-scale imaging, elemental analysis, site-specific deposition and milling, etc. on materials including metals, ceramics and polymers
- Trained and provided consultation to academic and industrial users on techniques including SEM imaging, EDS, FIB operation and XRD characterization
- Carried out basic routine maintenance of instruments and consumable supplies

Publications

- **Yingjie Yang**, Daniel R. Mumm and Martha L. Mecartney. "Flash sintering produces eutectic microstructures in Al_2O_3-$LaPO_4$versus conventional microstructures in 8YSZ-$LaPO_4$" *Journal of the American Ceramic Society* 104.8 (2021): 3895-3909.
- **Yingjie Yang**, Daniel R. Mumm and Martha L. Mecartney. (2021) Eutectic Phase Diagram for Al_2O_3-$LaPO_4$. Manuscript in preparation.
- Nadjia Motley, **Yingjie Yang**, Daniel R. Mumm and Martha L. Mecartney. (2021) The role of interfaces in modifying thermal conductivity of multiphase ceramics. Manuscript in preparation.
- Nadjia Motley, **Yingjie Yang**, Daniel R. Mumm and Martha L. Mecartney. (2021) Thermal conductivity and mechanical properties of high entropy RE zirconates. Manuscript in preparation

Skills

Characterization: Scanning electron microscopy (**SEM**) (SE and BSE imaging, EDS mapping, EBSD mapping, FIB depositing and milling); X-ray powder diffraction (**XRD**) measurement and phase identification; Transmission electron microscopy (**TEM**) (bright-field imaging, dark field imaging, selected area electron diffraction, EDS), Scanning transmission electron microscopy (**STEM**) (bright-field imaging, dark field imaging, EDS), Atomic force microscopy (**AFM**), thermal analysis (**TGA**, **DSC**), porosity analysis (pycnometry), etc.

Instrument experience - FEI Thermo Fisher Scientific: Magellan SEM, Quanta SEM/FIB, **Tescan**: GAIA3 SEM/FIB, **Hitachi**: Regulus8230 SEM, **Philips**: XL30 SEM, CM-20 TEM, **JEOL**: JEM-2100F TEM, 2800 TEM, JEM-ARM300F Grand ARM TEM, **Oxford** EDS and EBSD detectors, **Gatan** cameras, **Rigaku**: Smart lab XRD, Ultima III, **Aton-Paar**: Tosca AFM, and **NETZSCH**: STA 449 F3 Jupiter

Experimental: Conventional sintering, pressing (isostatic press, hydraulic uniaxial press), binder addition and burnout, milling (ball mill, attrition mill), direct precipitation & solid-state reaction synthesis, mechanical tests **Other Software:** Microsoft Office, LATEX, CrystalMaker, Adobe Photoshop, Dreamweaver, etc

Teaching Experience

Pedagogical training: Developing Teaching Excellence course, Improv for Teaching certificate program at the UCI Graduate Division, workshops offered by the UCI Division of Teaching Excellence and Innovation

Teaching assistant for the Department of MSE at UCI 2018-2021

Courses: Introduction to Materials Science and Engineering, Ceramic Materials, Materials Kinetics and Phase Transformations, and Diffusion and Heat Transport in Materials

- Guest-lectured in class and assisted in organizing routine lectures and in-class demonstrations
- Conducted weekly discussion sessions, held office hours and hosted review sessions for up to 80 students
- Organized midterms and final exams, graded homework assignments and exams of 50-80 students

Conference Presentations

Oral presentations

- **Yingjie Yang** and Martha L. Mecartney. (May 2019). *Eutectic Structure Induced by Flash Sintering* $LaPO_4/Al_2O_3$ *Composites.* International Conference on High-Performance Ceramics
- **Yingjie Yang** and Martha L. Mecartney. (Apr. 2019). *Novel Microstructures Produced by Flash Sintering* $LaPO_4/Al_2O_3$ *Composites.* Southern California Society for Microscopy and Microanalysis

Poster presentations

- **Yingjie Yang** and Martha L. Mecartney. (Aug. 2019). *Novel Microstructures Produced by Flash Sintering* $LaPO_4/Al_2O_3$ *Composites.* Microscopy and Microanalysis
- Rukmini Gorthy, Martha Mecartney, **Yingjie Yang**, Mingjie Xu, Toshihiro Aoki, Jian-Guo Zheng, *et al*, Susan Krumdieck. (Jun. 2019). *Nanostructure Generation and Surface Area Enhancement in Biphase* TiO_2 *Based Photocatalytic Coatings by pp-MOCVD.* the EuroCVD 22-Baltic ALD 16 Conference

- **Yingjie Yang**, David Kok, and Martha L. Mecartney. (Aug. 2018). *Flash Sintering of Multi-component Ceramics.* Gordon Research Conference and Gordon Research Seminar

Conference Proceeding

- **Yingjie Yang** and Martha L. Mecartney. (2019) "Novel Microstructures Produced by Flash Sintering $LaPO_4/Al_2O_3$ Composites" *Microscopy and Microanalysis*, 25.S2, 2406-2407.

Trainings and Certifications

Trainings

High Resolution Electron Microscopy (HREM) Winter School at Arizona State University	2020
The UCI School for Transmission Electron Microscopy	2019
European Ceramic Society Summer School and Conference	2017

Certifications

Industry Insights for STEM Scientists	2021
Management Beyond the Classroom	2020
Visualizing Science	2020
Activate to Captivate	2019
Mentoring Excellence	2019
Excellence in Engineering Communications	2018

Honors & Awards

2nd place in the Ceramographic Competition in Scanning Electron Microscopy at MS&T	2019
The Henry Samueli Fellowship in the Department of Chemical Engineering and Materials Science	2017
Chun-Tsung scholarship at SJTU (funded by Nobelist Tsung-Dao Lee)	2014-2016

Current Professional Association Membership

American Ceramic Society Global Graduate Researcher Network
Southern California Society for Microscopy and Microanalysis
Microscopy Society of America and Microanalysis Society

Leadership & Outreach Activities

Regional liaison of the Microscopy Society of America Student Council (the MSA StC)
Co-chair of the Educational Outreach Committee of the MSA StC 2019-2021

- Community building for graduate and undergraduate students in relevant fields
- Co-organizing webinars with members of StC to expand regional influence
- Moderated in events co-hosted by the StC and local facilities such as the Women in Microscopy Conference 2021

Outreach & Community Service Chair of Graduate Student Assoc. of MSE 2019-2020

- Managed outreach events with an audience aged 5-16 to spark their interests in STEM subjects and taught them how to apply basic scientific approaches
- Organized outreach panel in local community college Orange Coast College to share graduate school experiences
- Contributed to fundraising events, social events, department orientations, other information sessions, etc

Mentor of Graduate InterConnect Program at UCI 2018-2020

- Served as a **senior peer mentor** to assist the Graduate Division in organizing events such as the orientation
- Facilitated the transition of incoming international students by sharing personal experiences and connecting them with their peers

Member of Girls Engineering Change at UCI 2018-2019
Mentor for the summer outreach program with Breakthrough in the Mecartney group 2018

ABSTRACT OF THE DISSERTATION

Flash Sintering of $LaPO_4$-Al_2O_3 Ceramic Composites:

Eutectic Microstructures and Sapphire Crystals

by

Yingjie Yang

Doctor of Philosophy in Materials Science and Engineering

University of California, Irvine, 2021

Professor Martha L. Mecartney, Chair

Flash sintering directly applies an electric field to ceramic green bodies in order to quickly densify at low furnace temperatures, a process that has great potential for saving energy and reducing production costs during manufacturing. This novel manufacturing method has been proven effective for a number of ceramics, especially 8 mol % yttria-stabilized zirconia (8YSZ). In the past, primarily single-phase materials or composites that include 8YSZ have been the focus of flash sintering studies, while research on other composites has been lacking. This study investigated the phenomena of flash sintering applied to a novel monazite ($LaPO_4$) single phase system and the $LaPO_4$-Al_2O_3 system with comparisons to the $LaPO_4$-8YSZ system. The processing-microstructure-properties relationship between composition/time/furnace temperature/applied voltage/current limit and the resultant microstructures are investigated. While $LaPO_4$ and Al_2O_3 could not flash sinter under the highest voltage and currents used, the composite $LaPO_4$-Al_2O_3 system experienced flash sintering at the highest applied voltages, and as expected, the composite $LaPO_4$-8YSZ easily flashed due to presence of 8YSZ. Eutectic microstructures were prominent in the $LaPO_4$-Al_2O_3 system, and abnormal grain growth of both phases could be produced under suitable flash sintering conditions. Large facetted sapphire crystals formed with unique wetting characteristics with respect to monazite. The formation of an intertwined eutectic microstructure was attributed to the elevated local temperatures during flash and demonstrated the potential of flash sintering for high temperature processing without high temperature furnaces and crucibles. This study proved $LaPO_4$-Al_2O_3 to be a eutectic-forming system, and the solid solubility, eutectic temperature, and eutectic composition were explored to construct a eutectic phase diagram for $LaPO_4$-Al_2O_3. In addition, the hardness of the eutectic microstructure were also characterized and found superior compared to polycrystalline microstructures with the two phases. In summary, this work shows that flash sintering can be utilized to produce unconventional microstructures with improved mechanical properties in certain binary systems.

CHAPTER 1 INTRODUCTION

1.1 Composite ceramic materials of $LaPO_4$, Al_2O_3 and 8YSZ

Alumina is one of the most widely used ceramic for electronic packing, cutting tools, ceramic matrix composites, military armor, automotive parts, etc.[1–5] 8 mol% yttria-stabilized zirconia (8YSZ) is known for applications in solid oxide electrolytes and oxygen sensors, nuclear waste disposal materials, and dental ceramics.[6–9] Monazite ($LaPO_4$) has several major applications, including high temperature coatings, diffusion barriers and matrix material for fiber-reinforced composites, among others.[10–13] Monazite is also a proton conduction material if doped and a potential nuclear waste form candidate for nuclear waste disposal.[14,15]

$LaPO_4$ is known to be phase compatible without reacting with alumina and 8YSZ at high temperatures up to 1600°C. [16–19] P.D. Morgan *et al.*[18] found that the addition of interphase $LaPO_4$ to an Al_2O_3 matrix reinforced with sapphire fibers greatly improved the fracture resistance due to reduced crack propagation through the fibers, by crack deflection and debonding along the weak $LaPO_4$–Al_2O_3 interface. Similar effects were observed in multilayered 3YSZ–$LaPO_4$ composites, and persisted up to 1600°C,[19] and also in YSZ–$LaPO_4$ to 1000°C.[20,21] Composites with at least 30 wt. % $LaPO_4$ in Al_2O_3 and at least 25 % $LaPO_4$ in ZrO_2 enable them to be machined by WC tooling due to the weak interfaces as monazite does not bond well to oxide ceramics.[22–24]

The use of monazite as a matrix in ceramic matrix composites therefore has great potential. [25,26] Al_2O_3–$LaPO_4$ composites have high machinability, good biocompatibility, and high thermal shock resistance,[27–29] and 8YSZ–$LaPO_4$ composites have been investigated for their improved corrosion resistance behavior as thermal barrier coatings.[17,30] 8YSZ–Al_2O_3 composites have been proposed for improved thermal shock in oxygen sensors.[31] Al_2O_3–$LaPO_4$ composites have great promise as a high temperature structural ceramic material.[32,33] ZrO_2–$LaPO_4$ has been proposed for thermal barrier coating applications.[34]

Since the Al_2O_3–$LaPO_4$ composite system has great promise as a high temperature structural ceramic material, [32,33] and ZrO_2–$LaPO_4$ has been proposed for thermal barrier coating applications,[34] it is worthwhile to select these materials for further study with the new process of flash sintering as will be detailed in this dissertation.

1.2 Electric-field-assisted sintering

1.2.1 Challenges of conventional sintering

Conventional sintering processing and microstructure development of these high-temperature ceramics and composites has been widely studied. For Al_2O_3, $LaPO_4$ and 8YSZ single phase systems, temperatures between 1400-1600°C and dwell times longer than a few hours are usually required to reach full density.[35–38] Conventional processing requires high-temperature furnaces to fire and densify the materials. This energy consumption cost can account to up to 75% of the total production cost in some ceramic products in the European ceramics industry.[39,40]

Studies have shown that reducing the furnace temperature from 1600°C to 1200°C can half the energy consumption for sintering alumina.[40] The ceramics industry is also more and more concerned about the greenhouse gas emission and CO_2 footprint during fabrication processes. Major sources for thermal energy include combustion of natural gas and electricity from the use of fossil fuel; both lead to the products that cause global warming.[41] Because of the large energy consumption due to the high temperature and long times, a more economical and efficient method of densification would both lower manufacturing costs and reduce greenhouse gas emission from energy sources.[39–41] The motivation of this study is to reduce energy consumption and lessen the environmental impact of ceramic fabrication.

Challenges in conventional sintering not only lies in the high energy consumption and environmental aspects but the volatility of some components of ceramic materials, such as in relaxor dielectric ceramics and proton conducting materials such as Sr-doped $LaPO_4$.[42,43]

1.2.2 Flash sintering

Flash sintering is a sintering method that includes the direct application of an external electrical field to a green body while sintering without applied pressure.[44] In past studies, flash sintering has been demonstrated to greatly lower the sintering temperature and shortened the sintering time for many single-phase ceramics.[44–52] Flash sintering studies have been reported on a number of oxide materials: ionic conductors such as yttria-stabilized zirconia; semiconductors and insulators such as alumina, barium titanate, strontium titanate, boron carbide; as well as metallic-like ceramics such as ZrB_2.[46] The range of materials studied include ceramic materials that conduct electricity with ions, protons, electrons, and covalent semiconductor materials.[53] The applied electric field assists densification and lowers the furnace temperature needed, in some cases, for more than 500°C.

In the past studies, flash sintering has been proven to accelerate sintering and for not only single-phase materials,[29-37, 41, 42] but binary and ternary composite systems.[56–58] For example, Kok *et al.* observed densification in 3 seconds with a composite of α-Al_2O_3, $MgAl_2O_4$ spinel, and cubic 8 mol% Y_2O_3-stabilized ZrO_2 (8YSZ), while flash sintering of single-phase Al_2O_3 or spinel required much longer time and higher furnace temperature to reach similar density.[56] However, flash sintering of composite systems has not been extensively studied, especially composites without YSZ.[46] YSZ is a special ceramic that easily flash sinters and was the first material to demonstrate the phenomenon of flash sintering.[44] It has been suggested that the flash phenomenon may be enhanced using composite systems, as inter-phase interfaces might be the cause of promoted flash sintering in composite systems,[58,59] but the mechanism is yet to be verified.[60–62]

Variations for flash sintering include pulsed electrical fields,[63] alternating current,[64] different geometries of the samples,[49,60,65] different electrode materials,[66,67] etc. . , but the main parameters used in every flash sintering experiment are the minimum temperature of the furnace when flash sintering will occur, the voltage applied to the cross section, the current density, and the time the current flows through the sample.

The process of flash sintering includes three stages of development.[68] Stage I is the pre-flash incubation period, where the current in the system increases slowly due to the insulating nature of ceramic materials. Stage II is the transient period where onset of flash happens, the current increase accelerated and spikes, leading to a power spike and flash of light from the material. The onset of flash is also accompanied by a temperature spike locally. This stage includes the peak in power dissipation[68] and the power supply switches to current control. Stage III is a quasi-steady state where the sample continues to flash during the hold time of the electric field, and where rapid densification happens accompanied by fast grain growth. The three stages during the flash sintering process is illustrated in Figure 1.1.

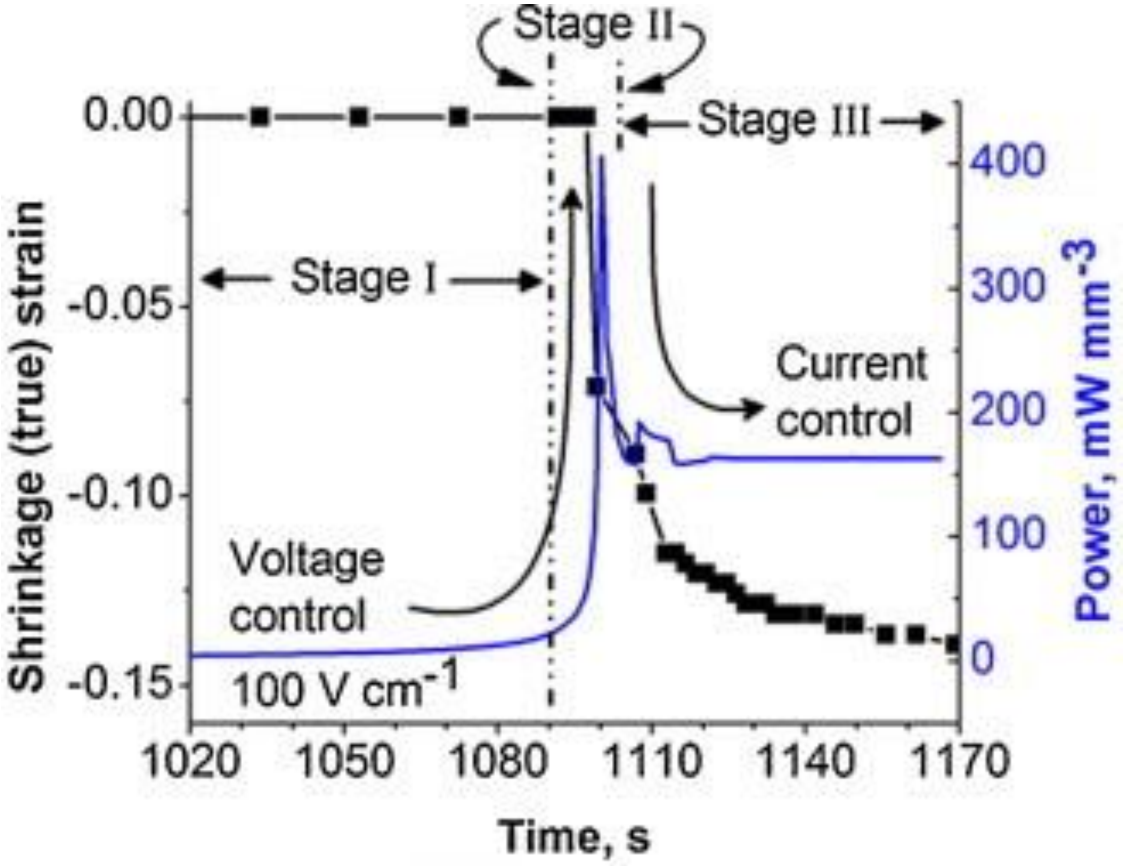

Figure 1.1 Power density and shrinkage strain as function of time for flash sintering of 3YSZ under 100 V/cm[68]

1.2.3 *Mechanisms for flash sintering*

There is no universally accepted answer to what the mechanism is for flash sintering that explains all of the physical phenomena, but there are a few possible explanations.

Evidence suggests that rapid heating alone can cause the accelerated densification observed in flash sintering experiments.[69] However, in rapid heating experiments, the temperature needed to sinter the sample within in similar time frame to flash sintering is up to 600 °C higher than the estimated sample temperature.[61] Joule heating can also be attributed as the reason of flash sintering due to thermal runaway caused by the rapid reduction of resistivity.[60,70,71] Other aspects of joule heating have been proposed to explain flash sintering, such as temperature increase at the grain boundaries, [44,72–74] and localized melting promoting conductivity.[72,75] Another possible explanation for flash sintering is that Frenkel defect pairs in the material nucleates and ionizes into charge neutral vacancies and interstitials, as well as electron-hole pairs. [32,5876,77] This is also a likely explanation of the electroluminescence phenomena during flash sintering. This theory, however, is also conflicted by counter evidence. *Naik et al.*[68] concluded that defect mobility does not change during flash sintering, because there is no change in the activation energy for diffusion in YSZ and alumina composites. It is therefore proposed that defect concentration increases drastically due to the electric field, instead of change in defect mobility.

Other theories for the mechanism of flash sintering points directly to the effects of the electric field. Weak electrical fields and electromagnetic radiation can enhance sintering as well, as observed in sintering experiments with a field as low as 20 V/cm.[78] Electric field effect can also be applied to flash sintering through electrochemical reduction, especially for ionic conductors, where the movement of oxygen vacancies and electrons promote conductivity.[79]

This dissertation will evaluate how the parameters for flash affect the resultant microstructure for composite systems containing monazite. In addition, as there is little documented data on the mechanical properties of flash sintered ceramics, the mechanical properties of the composite will also be studied.

CHAPTER 2 EXPERIMENTAL

2.1 Materials

The following raw materials were used to fabricate the samples: α-Al_2O_3 powders (99.99%, Taimei TM-DAR, Japan), 8 mol% Y_2O_3 stabilized cubic ZrO_2 powders (TZ-8YS, Tosoh, USA) and hydrated $LaPO_4$ rhabdophane powders ($LaPO_4 \cdot xH_2O$, Strem Chemicals, USA). The hydrated $LaPO_4$ powders were annealed at 1000°C for 1 hour to ensure removal of any hydrate and generate the monazite phase of $LaPO_4$.

2.2 Experimental setup and procedures

2.2.1 Ceramic processing

Composites of alumina and monazite were prepared by mixing in certain volume percentages (25%, 50%, 75%) alumina with the monazite powders, and mixed by attrition mill (HD-01, Union Process, Akron, OH) with isopropyl alcohol for 8 hours to ensure uniform distribution. Similarly, composites of 8YSZ and monazite were prepared with 25 vol.% and 50 vol.% 8YSZ. Media used for milling was 0.5-mm high-wear-resistant zirconia grinding media (YTZ Grinding Media, Tosoh, USA) for composites containing 8YSZ, or 0.5-mm alumina grinding media (99.5%, Union Process, USA) for composites containing Al_2O_3. Milling was done with 1 kg of media to 35 g of powders. Mixtures were dried with a rotary evaporator, 2.5 wt% of dissolved polyvinyl alcohol (PVA) was then added to the dried powders. The slurry was then dried again below 80°C, the product ground with a mortar and pestle, and sieved to 106 μm.

To prepare green bodies for both conventional and flash sintering, powders were pressed in a dog-bone shaped mold in a uniaxial press (Carver, USA) at 260 MPa for 5 minutes. After PVA binder was burnt out in an ashing furnace at 600°C for 1 hour, the relative green body density was 50±2%. Dog-bone samples were made with a hole at each end with a gauge length of 13.5 mm, and a cross section of approximately 3.5 mm × 1.6 mm.

Conventional sintering was conducted in a bottom loading furnace (Thermal Fisher Scientific, USA), with a dwell temperature of 1550°C and a dwell time of 5 hrs.

2.2.2 Flash sintering set-up

A typical flash sintering experiment is conducted with the sample in the hot zone of a furnace, each end in contact with a pair of Pt hooks that lead to a power supply,[44] as shown in Equation 2.1. A camera is usually set up to observe and record the process in real-time.

As shown in Figure 2.1, samples in this work were placed in a horizontal tube furnace (ATS, USA), with a pair of Pt hooks that connect the holes at the ends of the dog-bone samples with the resistance wires (Kanthal, Sweden) that lead to the power supply (Glassman High Voltage, USA) outside of the furnace controlled by a computer. Platinum paste was applied around the connection to ensure good conduction. The computer also records the voltage and current measured by a multimeter (Newark, USA), and records videos of the flash sintering experiments taken by a CCD camera (The Imaging Source, USA).

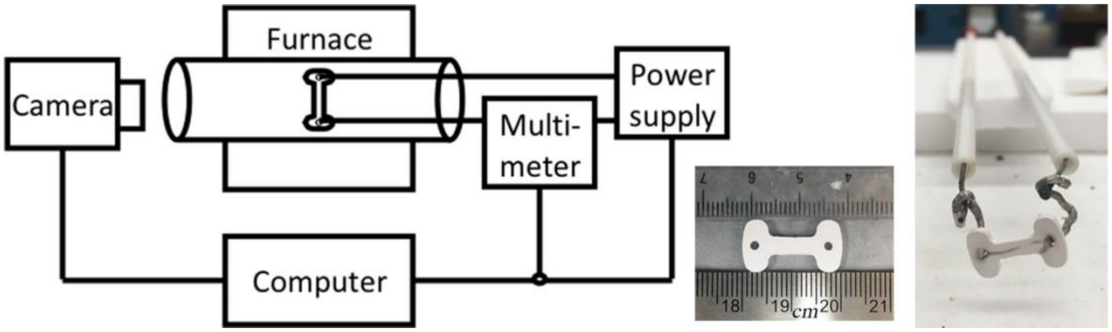

Figure 2.1 Sketch of experimental setup for flash sintering, photographs of a green dog-bone sample and a flashed dog-bone sample with electrodes attached

The onset of the flash phenomenon is controlled by the furnace temperature and the applied voltage. An initial voltage is set to the sample, with a low current passing through the sample, with the furnace temperature ramped up.

The flash of the sample is marked with this sudden spike in the measured current, when the power supply then automatically switches to current control when the preset current limit was reached. The current limit was set to avoid power overshoot and to tailor the microstructure of the sample as the current multiplied by the voltage equals the power input into the sample. This would also be the point that we observe a flash of light in the camera. The flash is then held for a certain amount of time and the voltage turned off after.

Voltage applied on the sample was determined by the potential drop over the initial length between the two electrical contacts. The current density limit applied on the sample was calculated by the current divided by the initial cross-sectional area of the gauge section. In this study, the furnace is ramped up from room temperature to 1450°C or until flash, whichever is sooner. A voltage of 250 V/cm is applied from the beginning of the ramp. If the temperature reaches 1450°C without the sample flashing, it is held for 5 min to stabilize the temperature throughout the sample. The voltage was then turned up step by step with 100 V/cm increment per 2 min, to reach a stabilized new temperature without significant densification. When flash occurs, the current spikes up and the power supply switches to current control to avoid power overshoot. The applied electric field was then held for around 10 seconds and shut down together with the furnace with the sample cooling inside until room temperature. Figure 2.2 shows the schematics of conventional and flash sintering experiments in this study.

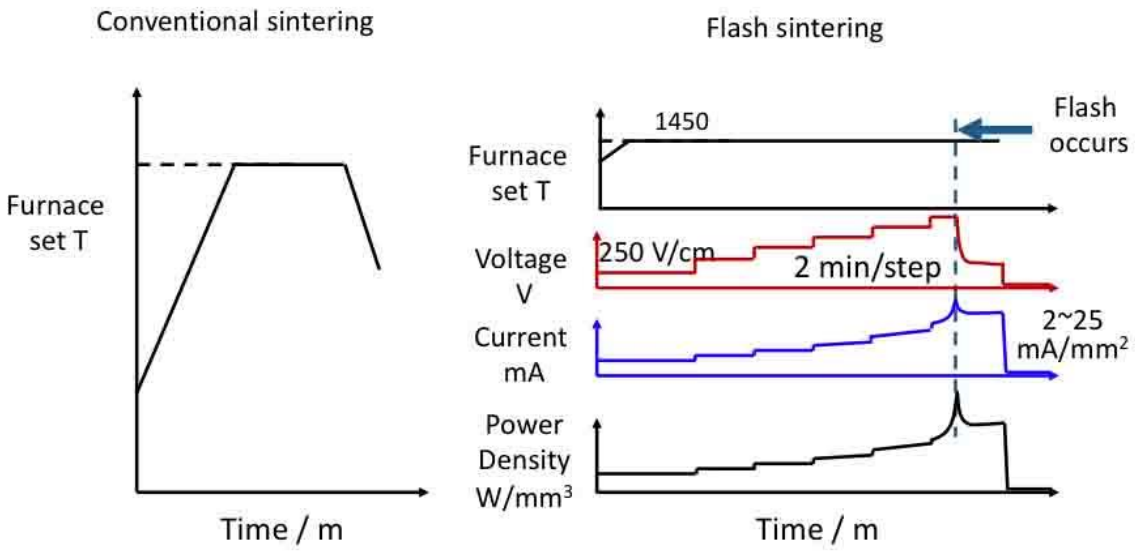

Figure 2.2 Temperature, voltage, current and power density profile of flash sintering experiments

2.3 Sample temperature estimation

Sample temperature is estimated through the black body radiation model.[61,75] Assuming the emissivity of the samples to be unity, the sample temperature T in relations to the furnace temperature T_0 and power input W is given by:

$$\frac{T}{T_0} = \left[1 + \frac{W_v}{e_m \sigma {T_0}^4}\left(\frac{V}{A}\right)\right]^{1/4} \qquad \text{Equation 2.1}$$

In the equation, $\sigma = 5.67 \times 10^{-8} Wm^2K^{-4}$ is a physical constant, A = 379 mm^2 is the area of the sample. The equation is derived from the Stefan Boltzmann law for black body radiation by Yang *et al.*[78] The Stefan Boltzmann law states that a black body absorbs and emits radiation at the same time, and the emission is proportional to the emissivity of the object and the fourth power of the temperature.[80] For simplicity's sake, we often assume the emissivity value to be unity. Because the emissivity value of ceramics is usually less than 1, and the channeling during flash is often concentrated in the central region of the sample, we often underestimate the flash region temperature.[61]

2.4 Characterization techniques

X-ray diffraction (XRD, Rigaku SmartLab, Japan[81]) was used to confirm the phase consistency of the single phase ceramics and the composites, before and after sintering.

The samples were coated as-is with C (EM ACE200, Leica, Germany) or Iridium (Q150T, EMS, USA) for SEM analysis. Secondary electron (SE) imaging, backscatter electron (BSE) imaging, and elemental analysis were done with FEI Magellan XHR SEM (Hillsboro, OR, USA) with Oxford energy dispersive x-ray spectroscopy detector (EDS, Oxford Instruments, United Kingdom). Transmission electron microscopy (TEM) imaging and diffraction analysis was done on Philips CM-20 (United States) and

TEM/STEM conducted on the JEOL JEM-2800 TEM (Japan), with samples cut with focused ion beam (FIB) system on Tescan GAIA SEM (Czech Republic) and FEI Quanta 3D FEG (USA).[82]

Electron backscatter diffraction (EBSD) (Tescan GAIA3 SEM-FIB, Czech Republic) and transmission Kikuchi diffraction (TKD) (FEI Quanta 3D FEG, USA) were conducted to analyze the orientation of the microstructures. Euler angle is used in both to represent the correlation between crystallographic orientations of the microstructures and the sample orientations in physical space (e.g., rolling direction).[83,84]

CHAPTER 3 FLASH SINTERING PRODUCES EUTECTIC MICROSTRUCTURES IN Al_2O_3–$LaPO_4$ VERSUS CONVENTIONAL MICROSTRUCTURES IN 8YSZ–$LaPO_4$

3.1 Abstract

While monazite ($LaPO_4$) does not flash sinter even at high fields of 1130 V/cm and temperatures of 1450°C, composite systems of 8YSZ–$LaPO_4$ and Al_2O_3–$LaPO_4$ have been found to more readily flash sinter. 8YSZ added to $LaPO_4$ greatly lowered the furnace temperature for flash to 1100°C using a field of only 250 V/cm. In these experiments, α-Al_2O_3 alone also did not flash sinter at 1450°C even with high fields of 1130 V/cm, but composites of Al_2O_3–$LaPO_4$ powders flash sintered at 900-1080 V/cm at 1450°C. Alumina–monazite (Al_2O_3–$LaPO_4$) composites with compositions ranging from 25 vol% to 75 vol% Al_2O_3 were flash sintered with current limits from 2-25 mA/mm^2. Microstructures were evaluated by scanning electron microscopy (SEM) and transmission electron microscopy (TEM). A eutectic microstructure was observed to form in all flash sintered Al_2O_3–$LaPO_4$ composites. With higher power (higher current limits), eutectic structures with regular lamellar regions were found to coexist in the channeled region (where the both current and the temperature were the highest) with large hexagonal-shaped α-Al_2O_3 grains (up to 75 μm) and large irregular $LaPO_4$ grains. With lower power (lower current limits), an irregular eutectic microstructure was dominant, and there was minimal abnormal grain growth. These results indicate that Al_2O_3–$LaPO_4$ is a eutectic-forming system and the eutectic temperature was reached

locally during flash sintering in regions. These eutectic microstructures with lamellar dimensions on the scale of 100 nm offer potential for improved mechanical properties.

3.2 Introduction

Flash sintering applies an electrical field across a ceramic green body, while heating it in a furnace.1–3 As the material sinters, the current induces joule heating, which assists in fast densification or enhanced reaction mixing. Over the past decade, flash sintering has shown promise in reducing sintering costs, increasing densification efficiency, promoting reaction sintering, etc.4 In the current era of energy conservation to preserve the environment, it is important to find a way to reduce energy consumption for material processing.[39,85] Due to its nature of fast transformation and densification, flash sintering can induce non-equilibrium transitions and lead to unconventional microstructures which may have interesting thermal and mechanical properties.[44,61,86]

The prerequisite conditions and phenomena of flash sintering are material specific.[44,55,69] 8 mol% Y2O3-stabilized ZrO2 (8YSZ) has been well established to flash sinter easily at low temperatures and low voltages.[31,44] The presence of 8YSZ can assist flash sintering for other materials in a composite.[56,87–89] Some single phase ceramics such as alumina are difficult to flash sinter,[66] but can flash easier when a constituent of a composite or through reaction sintering.[51,52,57]

The applied electric field during flash sintering generates a current that heats the sample far above the furnace temperature but other phenomena may also be involved, including enhanced flash sintering by the presence of heterointerfaces.[90]

Research on flash sintering of binary structural ceramic composite systems which contain heterointerfaces is limited[57,91–94] and will be addressed in this chapter.

The specific systems studied include monazite $LaPO_4$, 8YSZ and Al_2O_3 as single phases and as composites. $LaPO_4$ may be utilized as an interphase coating in ceramic fiber-matrix composites providing low-toughness interfaces, which can greatly enhance the damage tolerant behavior.[19,95]

3.3 Experimental

3.3.1 Flash Sintering

Flash sintering experiments were carried out with resistance furnace heat and an electrical field applied to the sample at the same time. For comparison, some samples were conventionally sintered at 1500°C for 5 hours.

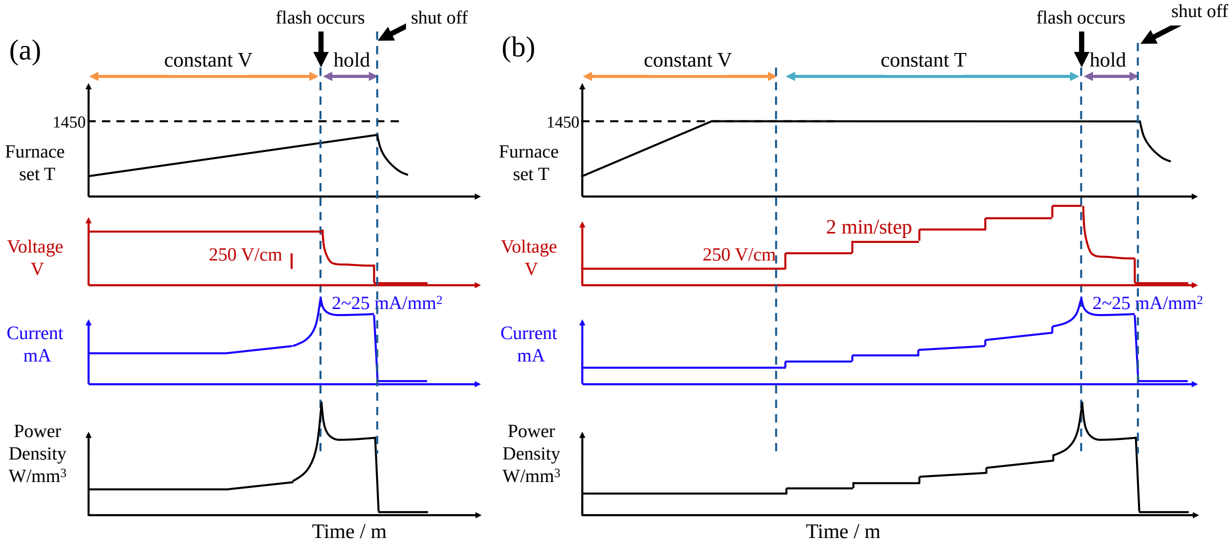

Figure 3.1 Two types of flash sintering conditions: (a) constant 250 V/cm is applied and the temperature is ramped up to 1450°C or the temperature that flash occurs and (b) temperature ramp to 1450°C with 250 V/cm then the voltage is increased by steps until flash occurs

The flash sintering experiments were conducted by first heating with constant voltage applied, then voltage increase with constant temperature (if needed), and a hold of the flash under current control. At the start of the experiment, an electrical field with a constant voltage density of 250 V/cm was applied to the sample in the furnace. The furnace temperature was ramped up from room temperature to 1450°C or until flash occurs. If flash occurred at a furnace temperature below 1450°C, it was held for 8-30 seconds, then both the power supply and the furnace were turned off, as shown in Figure 3.1(a). If flash did not occur with 250 V/cm when the temperature reached 1450°C, this condition was held for 5 min to stabilize the temperature throughout the sample and then the voltage was increased with increments of 100 V/cm every 2 minutes to a maximum of 1130 V/cm, as shown in Figure 3.1(b). If the sample flashed below the maximum capacity of the power supply was reached (1130 V/cm), this condition at the flash onset was held for 5.5-10 seconds before the furnace and power supply were shut off. In all cases, the samples were cooled in the furnace to room temperature after the power was turned off.

3.3.2 Characterization

The phase composition, elemental composition, and microstructure of the flash sintered samples were characterized. XRD was used to confirm complete phase transformation from hydrate $LaPO_4$ to monazite, verify the purity of alumina and 8YSZ, and the compositions and crystallographic structures of the composites. The analysis was also done on the dog-bone samples after flash sintering. SEM was used to image the sample surface with both secondary and backscatter electrons, after sputter coating it with iridium. EDS was conducted on samples coated with carbon. EBSD and TKD were used to analyze crystallographic orientations. TEM and diffraction were used to investigate crystalline microstructure with samples prepared by FIB.

3.4 Results

3.4.1 *The onset condition for flash is dependent on composition*

The flash conditions are summarized in Table 3.1 for the different compositions, average onset voltages (ranging from 250 V/cm to 1130 V/cm), current limits (2 mA/mm^2 to 25 mA/mm^2), furnace temperatures at onset of flash (780°C to 1450°C), estimated sample temperatures from joule heating, and general features of the resultant microstructures.

Table 3.1 Compositions, parameters, and microstructures of the flash-affected regions (estimated sample temperatures are calculated with the black-body radiation (BBR) model in Equation 2.1 using emissivity values of 1 and 0.4 as explained in Discussion)

Compo-sition (vol %)	**Flash?**	**Mean E-field (V/cm) ±SD**	**Current limit (mA /mm^2)**	**Mean maximum $T_{Furnace}$ (°C)**	**BBR $T_{estimated}$ (°C)**	**Flash hold time (s)**	**Microstructural features**
8YSZ	Yes	250	25	777 ± 9	1390 -1670	10	Enhanced sintering
50%-50% 8YSZ–$LaPO_4$	Yes	250	25	1110	1510 -1750	9-30	Enhanced sintering, uniform grains of both phases, minor cracking
25%-75% 8YSZ–$LaPO_4$	Yes	250	25	1393 ± 24	1670 -1860	10	Enhanced sintering, uniform grain size, minor cracking
Al_2O_3	No	1130	25	1450	N/A	N/A	No significant enhanced sintering
$LaPO_4$	No	1130	25	1450	N/A	N/A	No significant sintering

25%-75% Al_2O_3–$LaPO_4$	Yes	990 ± 42	25	1450	2150 -2510	8	Eutectic (regular), equiaxed $LaPO_4$ grains
50%-50% Al_2O_3–$LaPO_4$	Yes	1080 ± 53	25	1450	2190 -2570	8	Eutectic (regular & irregular), bigger hexagonal Al_2O_3, $LaPO_4$ grain growth
	Yes		15	1450	1970 -2270	6	Eutectic (regular & irregular), hexagonal Al_2O_3, $LaPO_4$ grain growth
	Yes		5	1450	1680 -1840	8	Eutectic (regular & irregular), smaller hexagonal Al_2O_3, $LaPO_4$ grain growth
	Yes		2	1450	1560 -1650	10	Eutectic (mostly irregular)
75%-25% Al_2O_3–$LaPO_4$	Yes	900 ± 71	5	1450	1640 -1800	8	Eutectic (no long-term order), equiaxed Al_2O_3 grains

Pure 8YSZ samples and composite samples containing 8YSZ all flashed at temperatures below 1450 °C with a constant applied voltage of 250 V/cm. The onset temperature of flash increased when the concentration of 8YSZ decreased (see Table 3.1). Pure 8YSZ samples flashed at an average temperature of 780°C; when 50% 8YSZ–50% $LaPO_4$ composites were tested, the samples flashed at around 1110°C. Dropping the amount of 8YSZ from 50 vol.% to 25 vol.% required a higher furnace temperature of 1379°C.

In this study, single phase monazite $LaPO_4$ or Al_2O_3 samples were not able to flash at 1450°C, even with applied voltages as high as the maximum capability of the power supply (1130 V/cm). However, samples of Al_2O_3–$LaPO_4$ composites were able to flash at lower voltages even at the same maximum furnace temperature of 1450°C. For samples containing 50% Al_2O_3–50% $LaPO_4$, the average onset voltage was 1080 V/cm. The average onset voltages for samples with other compositions were noticeably lower, 980 V/cm for samples with 25% Al_2O_3 and 935 V/cm for 75% Al_2O_3.

During the flash, the gauge sections of the dog-bone samples started to visibly brighten coinciding with the current spike, providing visualization of the flash region. Flash phenomena in all samples started with a nearly straight pathway that connected the two electrodes, shown in Figure 3.2. In all samples containing 8YSZ, the flash quickly propagated across the gauge section to form a continuous brightness with a gradient to the lateral edges. In samples containing Al_2O_3 and monazite, in contrast, the bright flash regions had abrupt boundaries and regions where the current was concentrated and channeled. The sharp boundaries of flash in those samples correlate with an abrupt change in the final microstructure across the gauge section, as will be shown later. In some cases, the channeling traveled from the front to the back through the thickness of the sample and connected the two electrodes on the opposite surfaces, as shown in Figure 3.2 (c).

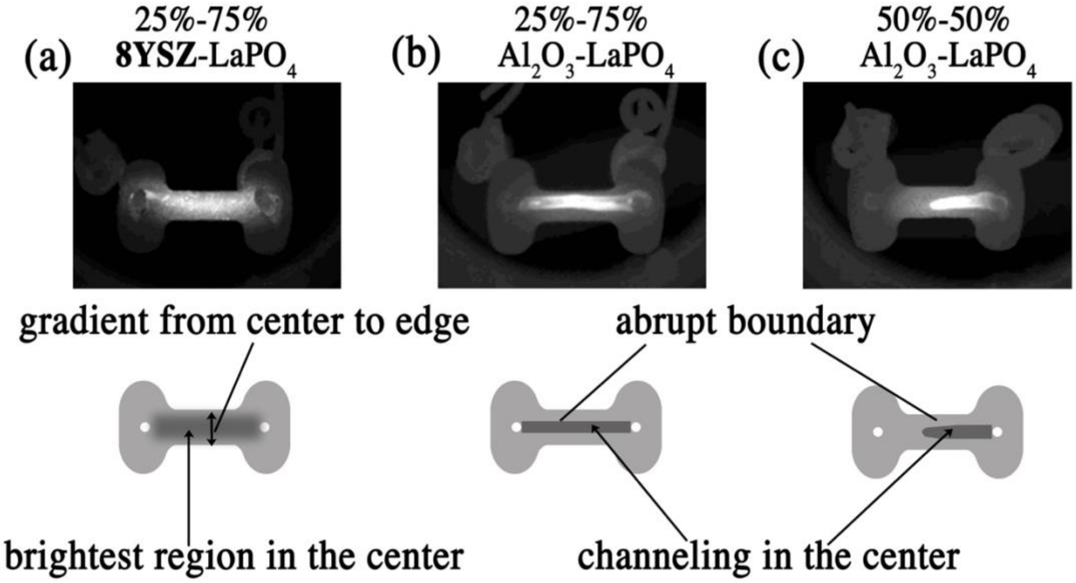

Figure 3.2 Photos of samples during flash and sketches of the flash region

3.4.2 Microstructure depends on the flash condition and composition

No new phases were formed, comparing XRD of the original powder mixtures to flash sintered samples.

For 8YSZ–LaPO$_4$ composites, flash sintered samples show polycrystalline morphology similar to conventionally sintered samples. The flash sintered dog-bone samples show equiaxed grains across the gauge section without significant channeling or boundaries, with slightly larger grains at the center and slightly smaller grains on the lateral edges of the gauge section, as shown in Figure 3.3. This agrees with the flash phenomenon shown in Figure 3.2, as the brightness where the current would be highest is higher at the center, lower at the gauge section lateral edges, and continuous across the gauge section. Under the imaging conditions utilized, the backscattering coefficients for 8YSZ and monazite are similar, such that negligible backscatter electron (BSE) imaging contrast exists between the two phases and no visual differentiation of the two can be directly observed.

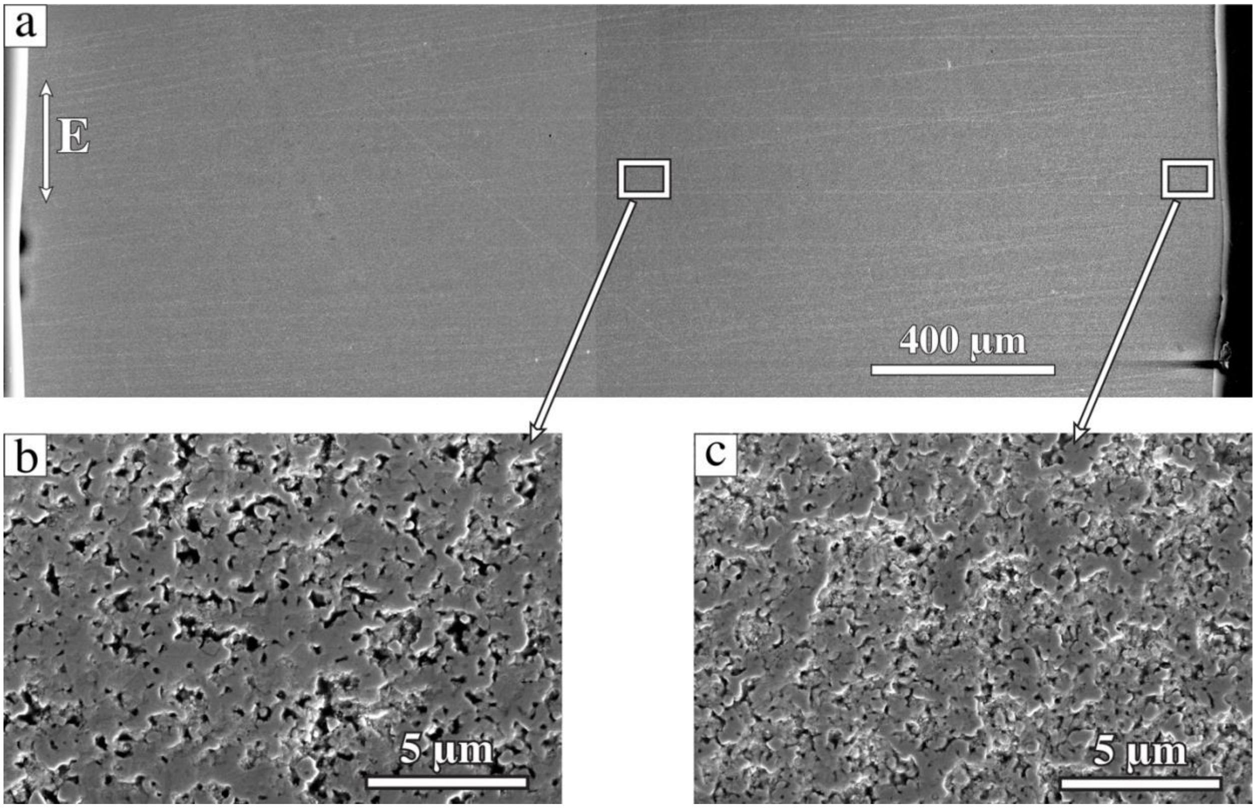

Figure 3.3 SEM images of the polished top surface in a 50-50 vol.% 8YSZ–$LaPO_4$ sample (250 V/cm, 25 mA/mm2, 30 s, 1110°C) showing (a) uniform structure across the gauge section at low magnification, (b) polycrystalline grains in the center region and (c) polycrystalline grains on the lateral edge. (The sample did not fully densify due to the short time and low temperature but the images demonstrate a fairly uniform structure with some slight differences in grain size and pore size from the center to the lateral edge.) The direction of the electric field is marked by the vertical arrows with an "E" label.

Flash sintered samples of Al_2O_3–$LaPO_4$ composites, in contrast, show drastically different morphologies compared to the 8YSZ–$LaPO_4$ composites. At the lateral edges, the microstructure consists of randomly oriented polycrystalline grains of both phases. A grooved region in the center can be observed macroscopically with abrupt boundaries on the sample surface, corresponding to the distinct brightened region during the flash shown in Figure 3.2. In the channeled regions, there is virtually no equiaxed polycrystalline microstructure for Al_2O_3–$LaPO_4$ composites. Instead, the channeled regions contain eutectic microstructures, highly faceted large grains, and grains with abnormal grain growth. Figure 3.4 illustrates the general regions where the corresponding microstructures are found.

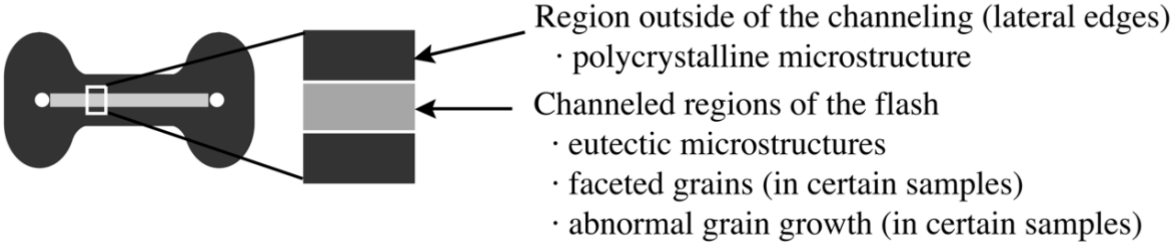

Figure 3.4 Sketch of a dog-bone sample and the locations of different structures that exist across the gauge section

The contrast difference for Al_2O_3 (ρ = 4 g/cm^3) and $LaPO_4$ (ρ = 5 g/cm^3) in BSE imaging clearly reveals each phase (Figure 3.5) on the surface of the sample. Images in Figure 3.5 are taken from the channeled regions as indicated in Figure 3.4. In this case, the backscattering coefficients of these two phases are quite distinct, and readily facilitate contrast differentiation. Alumina grains show a darker contrast because of the lower Z contrast while monazite grains show lighter contrast under the current backscatter imaging conditions. Eutectic structures show an intermediate grey contrast at low magnification due to the intertwined morphology of finely layered eutectic. Polycrystalline regions at the lateral edges show a clear mixture of randomly arranged bright and dark grains (polycrystalline structure in Figure 3.5).

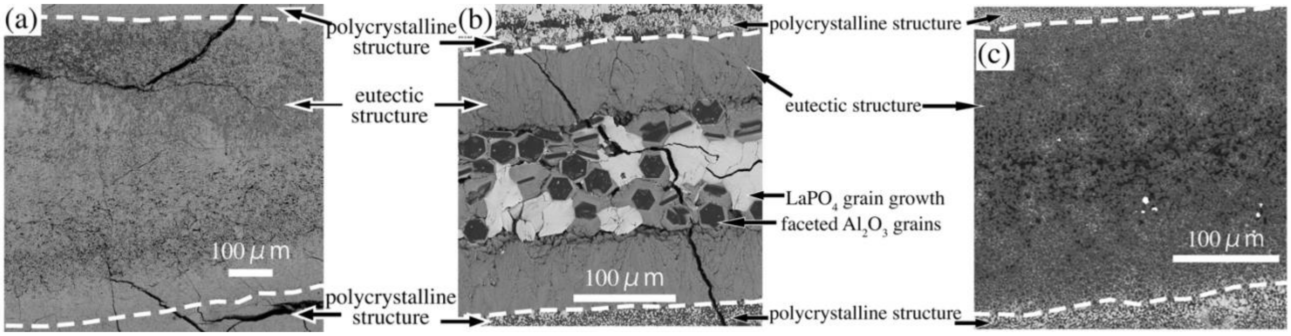

Figure 3.5 Channeled regions (bounded by lines) are similar on the surfaces in flash sintered $Al_2O_3/LaPO_4$ samples made under the same current limits (5 mA/mm^2) but with different alumina content: (a) 25-75% Al_2O_3–$LaPO_4$ (1000 V/cm 8 s) (b) 50-50% Al_2O_3–$LaPO_4$ (1050 V/cm 8 s) showing hexagonal alumina grains and large irregular shapes of monazite (c) 75-25% Al_2O_3–$LaPO_4$ (850 V/cm 8 s) flashed at a comparatively lower voltage

Distinct boundaries can be seen on the surface of Al_2O_3–$LaPO_4$ composites, marked by the contrast change that represent the abrupt change of microstructure from eutectic to polycrystalline (dotted lines in Figure 3.5). The center region that shows eutectic microstructure corresponds to the channeled region shown in Figure 3.2. Highly faceted alumina grains and monazite grains with abnormal grain growth appear in the center region on the surface, embedded in the eutectic structure, when a high current density is applied. Figure 3.5(a) clearly shows hexagonal and elongated faceted Al_2O_3 grains on the surface in the centermost region of the gauge section, as well as large irregular monazite grains, found on the surface of a 50% Al_2O_3–50% $LaPO_4$ sample. Adjacent to the centermost region is a grey contrast that represents the eutectic structure, which will be shown in detail later. On the edge of samples for all three compositions, a polycrystalline microstructure was observed that was similar to conventionally sintered Al_2O_3–$LaPO_4$. Large cracks from thermal shock can be seen throughout the sample as the flash sintering parameters and the cooling rate were not optimized.

3.4.3 Eutectic microstructures

Eutectic microstructures are represented by a gray contrast at low magnification. When observed closely, two types of eutectic structures coexist due to varying thermal profiles that can exist during flash sintering, and they form domains in the channeled regions. Figure 3.6 (a) shows regular lamellar eutectic structures that are parallel layers of alternating Al_2O_3 and $LaPO_4$ grains. The monazite grains can spherodize in the alumina matrix and form a dashed line. A different type of eutectic microstructure, the "irregular" eutectic structure (also characterized as anomalous[96,97]) that shows randomized orientation and no long-term order, exists on the sample surface as well, as shown in Figure 3.6 (b). These two morphologies can form domains and coexist in the channeled region, as shown later.

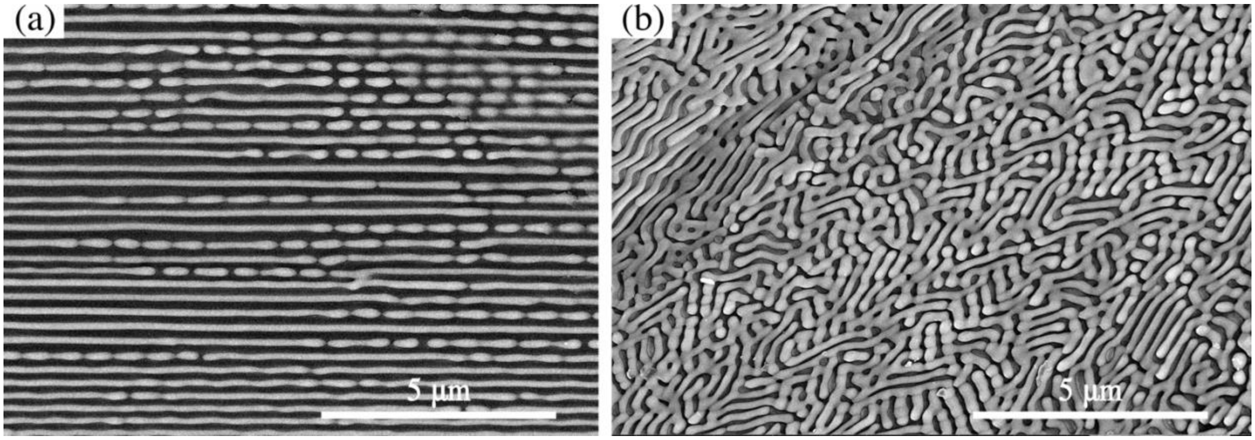

Figure 3.6 BSE images of the different eutectic microstructures on the surface of a 50-50% Al_2O_3–$LaPO_4$ sample (1100V/cm, 25 mA/mm^2, 8 s) (a) regular lamellar eutectic-like structure (b) irregular eutectic-like structure: dark grains are alumina, bright grains are monazite

When the flashed composition is not 50-50% Al_2O_3–$LaPO_4$, the eutectic structure is found to exist in areas between grains of the dominant phase, as presented in Figure 3.7. In samples with Al_2O_3 content reduced to 25%, the center region of the gauge section is dominated by a brighter $LaPO_4$ phase, the rounded grains are surrounded by eutectic microstructures, as shown in Figure 3.7(a). When Al_2O_3 content was increased to 75%, the center region of the image was dominated by darker faceted Al_2O_3 grains, with eutectic structures at the grain boundaries, as shown in Figure 3.7(b).

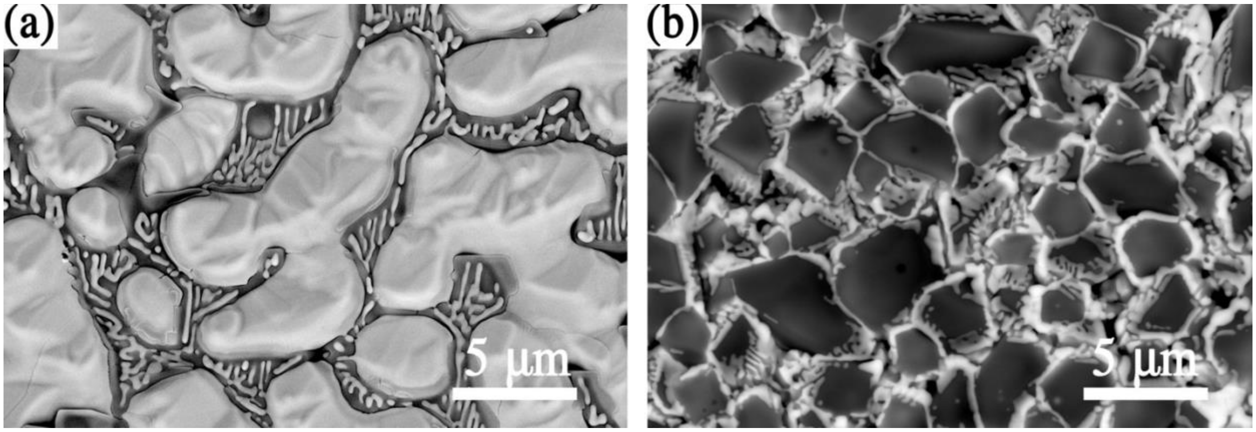

Figure 3.7 BSE images of the eutectic microstructures between grains of the dominant phase on the surface of (a) 25-75% Al_2O_3–$LaPO_4$ (1050V/cm, 25 mA/mm^2, 8 s) (b) 75-25% Al_2O_3–$LaPO_4$ (950V/cm, 5 mA/mm^2, 8 s)

Colonies formed by the eutectic can be observed from the cross section of the samples, as shown in Figure 3.8. The region with eutectic microstructure is within a roughly semicircle shape on the cross section, indicating that the flash channeled region was concentrated in a semi-cylindrical shaped volume along the gauge section. (The flash channeled region sometimes connects from the top to the bottom of the sample from one end to the other.) The borders of the colonies seen in the interior are marked by coarser alumina and monazite grains.

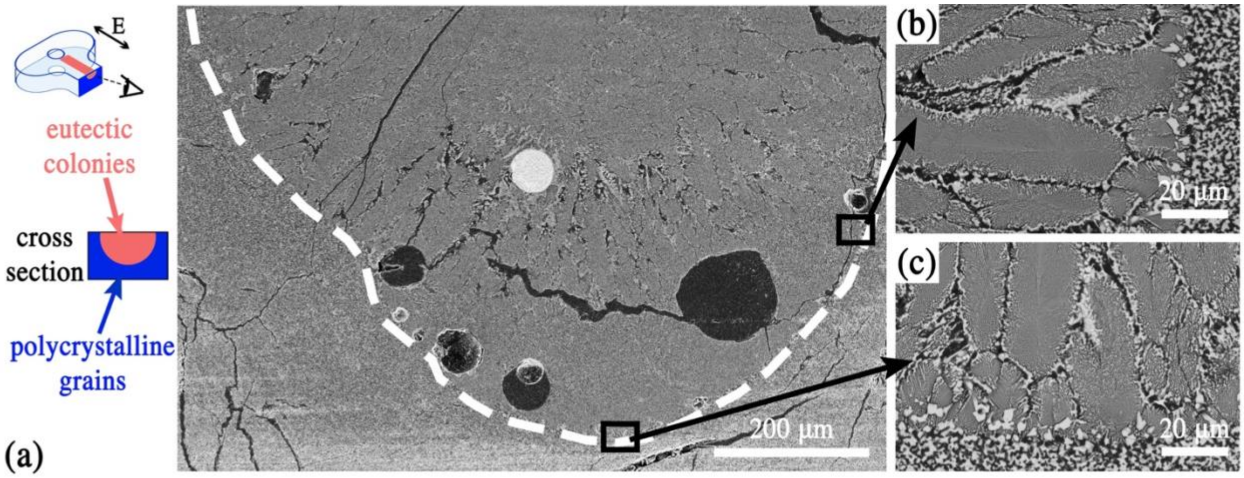

Figure 3.8 BSE images of a polished cross-section of a flash-sintered 50-50% Al_2O_3–$LaPO_4$ sample (25 mA/mm^2, 950 V/cm, 18 s) that (a) shows channeling does not span the entire sample thickness. (b) and (c) show the interior region that has eutectic colonies which appear to solidify normal to the polycrystalline regions of the randomly oriented alumina and monazite grain which did not melt. (The bright circular region in the center is a drop of Pt, black circular regions are pores filled with epoxy.) The dotted line is a guide to the eye for the flash channeled region of the sample.

3.4.4 Hexagonal alumina grains

The other type of unique microstructural feature present in the flashed region of the Al_2O_3–$LaPO_4$ composites is highly faceted alumina grains observed on the surface. Many alumina grains have a hexagonal shape close to a geometrically regular hexagon that is both equilateral and equiangular. Other large alumina grains have an elongated hexagonal shape that is close to equiangular. The faceted alumina grains, the thicknesses of which are estimated to range between 0.5 - 3 μm, are on the surface of a matrix of eutectic structures and monazite grains.

Figure 3.9 (a) and (b) shows the surface of 50-50% Al_2O_3–$LaPO_4$ samples made with current limits 25 mA/mm^2, (c) and (d) shows a sample made with 5 mA/mm^2, respectively. Comparing the grain sizes of

Figure 3.9 (a) and (b) or (c) and (d), the size of the hexagonal grains is much smaller when the current limit is reduced from 25 to 5 mA/mm^2. The diameters of the regular hexagonal single crystals of alumina reach 75 μm when the sample is flash sintered by 25 mA/mm^2, but only half that size with 5 mA/mm^2. When the current limit was set to 2 mA/mm^2, no faceted alumina grains or large monazite grains was observed.

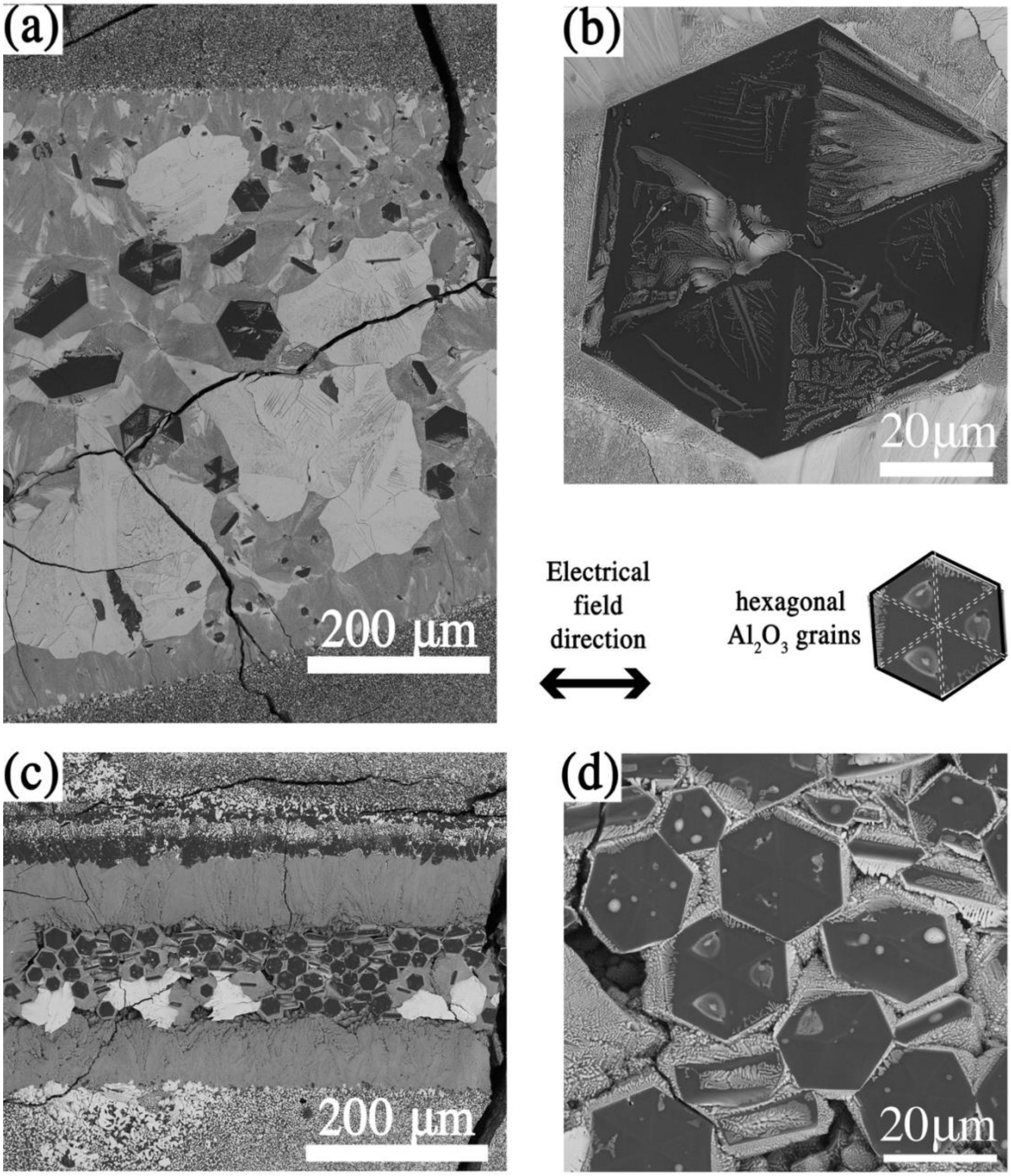

Figure 3.9 BSE image of the different grain sizes existing on the surface obtained by flash sintering 50-50% Al_2O_3–$LaPO_4$ with changing the current; (a) and (b) processed with a current limit of 25 mA/mm2 (950 V/cm, 5.5 s), (c) and (d) processed with a current limit of 5 mA/mm2 (1050 V/cm, 8 s). A higher current density, which results in higher power, creates larger grains of both hexagonal alumina and monazite.

The equiangular appearance of the Al_2O_3 crystals can be attributed to the crystalline orientations of the hexagonal grains. Figure 3.10 (a) shows the TEM sample made from milling perpendicular to one of the edges of a hexagonal alumina grain. The alumina large crystals are surrounded by a eutectic microstructure. TEM diffraction confirms that the surface of the hexagonal-shaped grains is normal to [0 0 0 1], so it is the basal plane of the pseudo-hexagonal lattice. The grain edges are normal to $<1\ 1\ \overline{2}\ 0>$. EBSD scans confirmed the same orientation throughout a hexagonal grain on the surface indicating it is a single crystal of sapphire (Figure 3.10 (b)). This grain was located on the side of the center groove and appears slanted because tilting in the SEM was limited by the EBSD configuration. It is worth noting that transmission Kikuchi diffraction results show that the Al_2O_3 grains in the eutectic microstructures near the single-crystal Al_2O_3 have similar orientations as the faceted grain.

The other commonly observed microstructural feature is that the hexagonal alumina crystals can be seen as a collection of six triangles with monazite on the surface of half of them (

Figure 3.9). The regions with monazite correspond to rough surfaces with a lower EBSD signal as well (Figure 3.10). FIB sectioning showed no existence of monazite inside the hexagonal alumina grains.

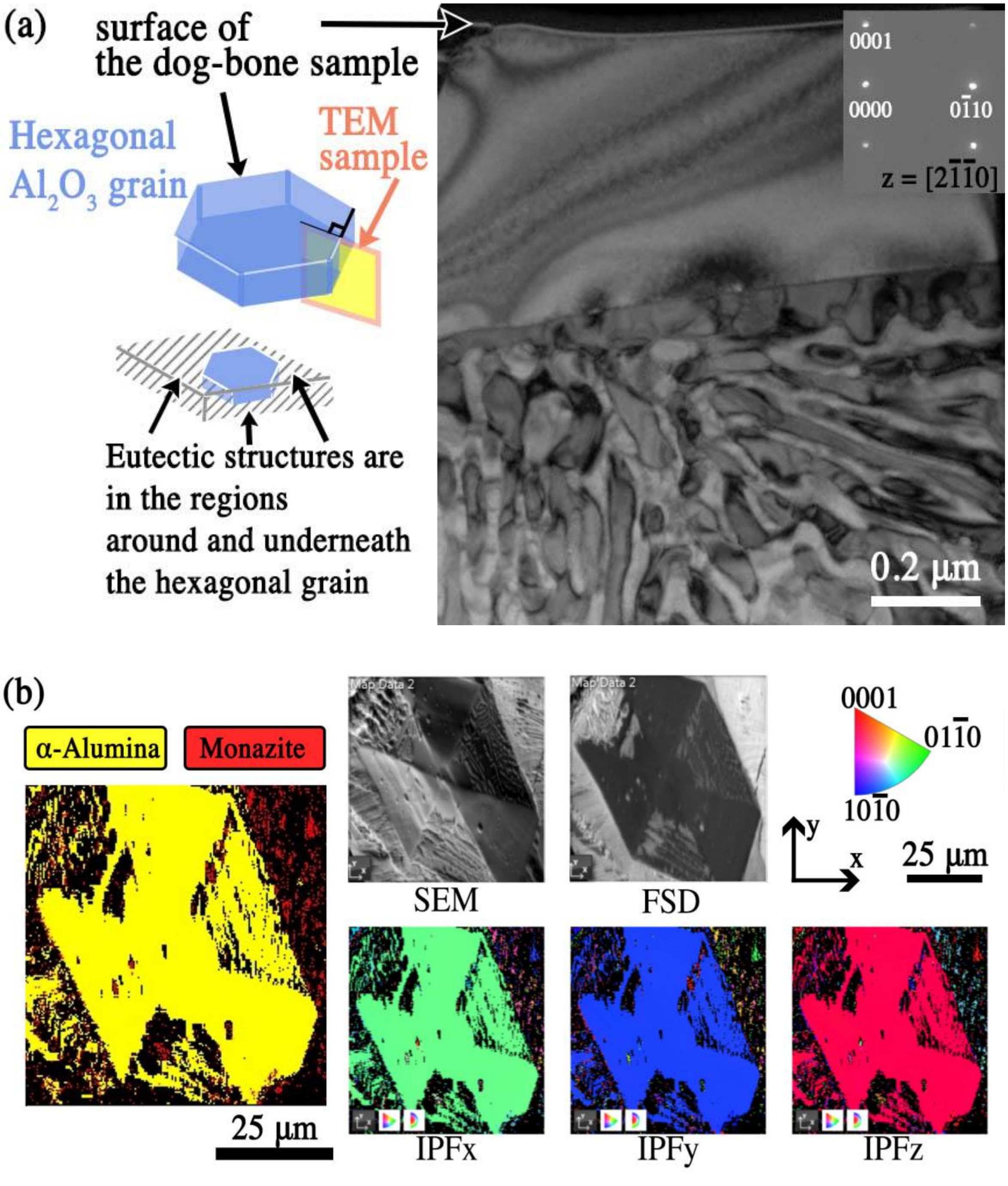

Figure 3.10 the orientation of the hexagonal alumina grains (a) image and diffraction pattern of a cross-section showing the (0 0 0 1) surface orientation of the hexagonal Al_2O_3 grain and eutectic microstructure underneath and (b) EBSD patterns showing that the large hexagonal Al_2O_3 grains on the surface are primarily one orientation (FSD images are obtained by a forward-scattered electron detector that collect backscattered electrons; graphs labeled IPFxyz show the crystalline orientation in the x, y, and z direction respectively, by coloring the maps with inverse pole figure color schemes)

3.4.5 Increased current limit increases power density and affects microstructure

The onset temperature and voltage required for flash vary depending on sample composition but did not greatly affect the microstructure of the flash sintered samples. However, the current limit of flash sintering has a significant influence on the width of the channeled region and the microstructure of the samples. Figure 3.5 shows two samples of different compositions flash sintered with the same current limit. The sizes of the center flash sintered region are nearly the same, indicating similar thermal profiles across the gauge section.

When samples with the same composition are flashed with different current limits, it is clear that the width of the channeled region that corresponds to flash increases with a higher applied current. Figure 3.11 shows the low-magnification images of 50-50% Al_2O_3–$LaPO_4$ samples flash sintered with maximum current limits of 25 mA/mm^2, 5 mA/mm^2 and 2 mA/mm^2. All samples have polycrystalline microstructure on the outside of the gauge section and eutectic microstructure at the center. The width of the channeled region that was subjected to melting and resolidification is the largest (920 μm) when the sample was flashed with the highest current limit 25 mA/mm^2, but only 260 μm when flash sintered with 5 mA/mm^2, and then even lower at 100 μm with 2 mA/mm^2. It has also been found that when the current limit is constant, but the increasing flash hold time was increased, the width of the channeled region increases as well.

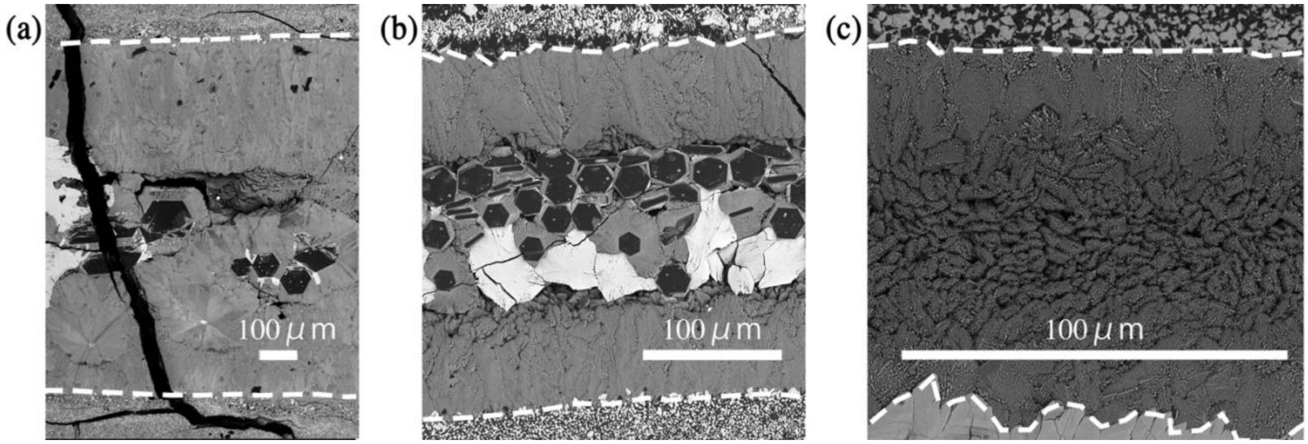

Figure 3.11 BSE images of flash sintered 50-50% Al_2O_3–$LaPO_4$ sample surfaces with different current limits of (a) 25 mA/mm2 (1100 V/cm 8 s), (b) 5 mA/mm2 (1050 V/cm 8 s), and (c) 2 mA/mm2 (1136 V/cm 10 s); the higher the current, the wider the channeled region (note that the scale bar is different for each image). The electrical field is in the horizontal direction of the photo.

Changing the current limit also changes the morphology of the microstructure. A low current limit of 2 mA/mm^2 does not produce large hexagonal alumina grains or abnormally large monazite grains with abnormal grain growth but creates only the eutectic microstructure (Figure 3.11(c)), in contrast with samples flash sintered with a higher enough current limit ($\geq$ 5 mA/mm^2 in this study).

Moreover, the morphologies of the eutectic microstructure can be tailored by changing the current limit of the flash. Both regular lamellar and irregular eutectic structures appear in samples processed with higher currents (

Figure 3.12 (a)). When the current limit is reduced to 5 mA/mm^2, irregular eutectic structure is the primary morphology throughout the channeled region (

Figure 3.12 (b)), more typical of coupled growth with the lower current.

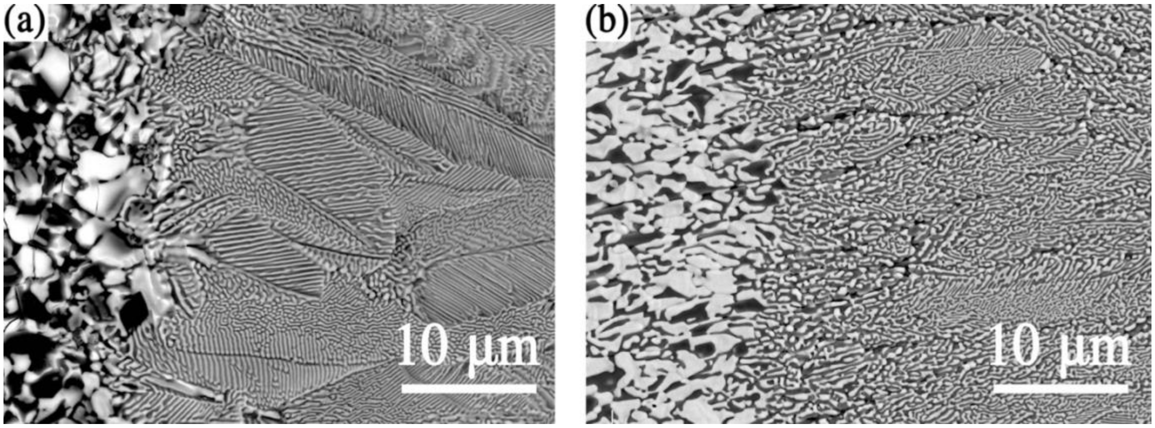

Figure 3.12 BSE images of eutectic structures on the surfaces of 50-50% Al_2O_3–$LaPO_4$ samples that depend on the current density showing (a) more regular eutectic-like structure that is produced under high current limit 25 mA/mm2 (950V/cm, 18 s), and (b) more irregular eutectic-like structure under low current limit 5 mA/mm2 (1100 V/cm, 10 s). These images are from the edge of the channeled region, next to the polycrystalline structure, randomly oriented alumina and monazite grains are seen on the left of each image.

3.5 Discussion

3.5.1 What promotes flash?

The onset conditions for flash sintering are different for the different compositions, as would be expected.[98] All 50-50% Al_2O_3–$LaPO_4$ composites flashed within ± 50 V. When the composition changed to 25-75% Al_2O_3–$LaPO_4$ and 75-25% Al_2O_3–$LaPO_4$, the onset voltage of flash is noticeably lower (up to 100 V), as shown in Table 3.1. At first glance, it is unclear where the voltage difference comes from. Without the presence of 8YSZ that facilitates a conductive pathway, [99] low ionic and electrical conductivity of Al_2O_3 or $LaPO_4$ single phases inhibit the current flow. One reasonable hypothesis is that the bi-material interface in the green body can facilitate flash sintering, which could potentially be attributed to the highly defective structure of such bi-material grain boundaries. Alternatively, it could be doping by cations that would increase conductivity, but this needs to be further studied to be confirmed.[32] Other composites have been shown to flash easier than the single-phase materials without the presence and assistance of 8YSZ.[87] The 50-50% Al_2O_3–$LaPO_4$ composites would have the maximum number of bi-material interfaces compared to other vol% compositions for the same particle sizes.

3.5.2 What is the sample temperature during flash and how is it related to current?

It has been well known that the electrical field can elevate the sample temperature to be higher than the furnace temperature.[100] According to the black body radiation model (BBR)[61,101] which assumes the sample is a black body, the elevation in sample temperature (ΔT) can be calculated based on the furnace temperature (T_0 in K), the input power density (W_v equals voltage density times current density, in units of W m^{-3}), the volume of the sample (V with the value of 225 mm^3), material emissivity (e_m), the surface area of the sample (A with the value of 380 mm^2 including all surface area), and a universal physical constant (σ with the value of 5.67×10^{-8} W m^{-2} K^{-4}). The normal total emissivity of 8YSZ is estimated to be 0.4 around 1800°C [102] (0.9 at room temperature) [103] and Al_2O_3 is 0.3-0.5 at 1470 °C.[104]

$$\frac{T}{T_0} = \left[1 + \frac{W_v}{e_m \sigma {T_0}^4}\left(\frac{V}{A}\right)\right]^{1/4} \qquad \text{Equation 2.1}$$

However, experimental data is lacking on composites and there is no known emissivity data for $LaPO_4$, hence the calculations used emissivity values of unity[61] and 0.4 to estimate the range of possible sample temperatures (see Table 3.1 under column "BBR $T_{estimated}$"). The usage of unity can underestimate the sample temperature[61] by hundreds of degrees, having eliminated the emissivity in the denominator in Equation

2.1, giving the lower bound of the possible sample temperature range; the upper bound of the temperature range is given by using 0.4 as the emissivity value, which likely results in an overestimation of the sample temperature because of heat loss from the sample and the unknown emissivity value of $LaPO_4$.

The melting temperature of Al_2O_3 is 2030°C and 2070°C for monazite.[105,106] If a eutectic exists, the eutectic temperature would be even lower. With some of the estimated temperatures as high as 2190°C, and considering the underestimation of the lower bound calculation, it is reasonable for the actual sample temperature during flash to be higher than the melting point and the energy would be sufficient to cause melting. Also, the variable localized current observed on the surface (Figure 3.5) would cause inhomogeneous temperatures that are higher than the predicted average temperature. Furthermore, the area of the channeled region on the cross-section in Figure 3.8, corresponding to the high current pathway, is significantly smaller than the gauge section – concentrating the heating further. It is also possible that a small amount of eutectic liquid can form at the interfaces which would enhance sintering as well as the local current.[107,108]

3.5.3 How do current, temperature, and channeling affect the microstructure?

The low thermal conductivity of $LaPO_4$ [22] can preclude effective heat transfer; although Al_2O_3 has higher thermal conductivity than 8YSZ in the monazite materials, the lower electrical conductivity in alumina contributes to a current flow that is less uniform. This created a molten and resolidified zone with distinct boundaries where the temperatures are higher. The abrupt boundaries can also be attributed to the temperature profile created by intense joule heating caused by the power spike. Heat can dissipate through conduction and convection due to the temperature difference within the sample and the elevation of sample temperature above the furnace temperature, but the abrupt boundaries of the channeled region are indications that the intense heat has not dissipated, and melting and rapid solidification only occurs within the boundaries. Research on flash sintering of Al_2O_3-$Y_3Al_5O_{12}$ (YAG) has shown the formation of similar eutectic microstructures but the paper postulates that melting does not occur.[94] The Al_2O_3/YAG system is similar to Al_2O_3–$LaPO_4$ in that YAG also has low conductivity [109] and is also observed to be difficult to flash sinter (1350°C, 900 V/cm).[94]

The estimated temperature correlated with the power input can qualitatively explain the trend of the channeled region widths. When the current density limit or the voltage density of the flash increases, the power increases – and as shown by Table 3.1, the highest temperature in the channeled region caused by the power spike also increases, leading to more material melting.

It was observed that higher current limit also promotes abnormal grain growth and leads to the large single crystals forming in the channeled region (

Figure 3.9). As the flash region temperature increases with the current, more time is needed to cool down whereby the crystals can grow quickly in what is possibly a eutectic liquid. There can also be a change in the nucleation rate that comes with the temperature change. At higher temperatures, one possible scenario is that the nucleation rate decreases while the growth rate increases, leading to fewer but larger crystals in the eutectic matrix.

Cracking has been observed in many samples produced in this study. During the experiment, the power supply and furnace were shut down right after the flash hold.

This may induce thermal shock of the samples. It should be noted that when the samples were annealed at 1450°C after completion of the 11 s flash hold instead of instantaneously cooling, crack formation was minimized.

3.5.4 How do surface and interfacial energy affect the resultant microstructure?

Al_2O_3 and $LaPO_4$ are highly immiscible. The XRD peaks of each phase do not shift before and after flash sintering, indicating no significant solid solubility. These materials do not react to form any new phases up to 1600°C, as proven by Marshall *et al.*,[110] and the present study shows that to be true up to melting, which is useful information for the high-temperature applications of the material system.

The tendency to minimize the interfacial area between Al_2O_3 and $LaPO_4$ can be observed by the spherodized monazite in the lamellae (Figure 3.6(a)) and on the surface of alumina crystals, consistent with the predicted high interfacial energy between the two phases.[19] The sides of the faceted alumina crystals are also low-index planes that have high symmetry and low surface energy.[111] The facets may be evidence of crystallization from a melt that exists when alumina starts to nucleate and grow. The apparent 3-fold rotational symmetry shown by the monazite arrangement on the surface of the alumina grains (Figure 3.9) is linked to the crystallographic structure and inherent symmetry of the α-alumina crystal (with space group #167, $R\bar{3}c$) and corresponds directly to the primary 3-fold roto-inversion axis aligned along the c-axis of sapphire.[112] This observation portends that there is growth direction dependent variations, such that the prismatic planes are not all equivalent and alternate according to the 3-fold roto-inversion symmetry. Future work is in progress to explore details of the interfacial energy considerations in this material system.

3.5.5 What factors may control the microstructure evolution of the eutectic?

The mechanism of forming regular and irregular eutectics in this material system is unknown. Even though directional cooling is evident in the orientation of the colonies growing perpendicular to the polycrystalline region in Figure 3.8, it is highly likely that more than one mechanism is at play due to the complicated thermal profiles of the molten and resolidified region.

The other possible cause of the "irregular eutectic" microstructure is that the phase transition has entered the region for spinodal transformations. The microstructures in Figure 3.6 (b) are reminiscent of spinodal decomposition, however, it would be necessary to capture the initial phase segregation in the liquid to differentiate between nucleation and growth and processes and spinoidal decomposition.

According to past literature, the discontinuity and structural faults in the regular lamellar structure can be caused by several different reasons, including liquid/solid interface shape instability, lattice strain, or sudden change in the growth conditions, etc.[96,97] Lamellar eutectic-like structures usually represent fast coupled growth of the crystallization front, the rate of which is a function of the undercooling in the composite system.[113] At the same time, it is known that drastically increasing the amount of undercooling can change the type of eutectic structure formed.[114] In theory, the irregular eutectic structures can be an indication of different growth velocities.

Although it is not clear which mechanism dominates, it is obvious that higher power applied from high currents promotes regular lamellar eutectic microstructures. These eutectic microstructures, with a characteristic lamellae thickness on a scale of 100 nm, have the potential for interesting mechanical properties promoting crack arrest.[115,116] Current work is on-going to evaluate the mechanical properties of such microstructures.

3.6 Conclusion

As expected, composites of monazite and 8YSZ can be easily flash sintered due to the enabling presence of 8YSZ which allows uniform heating of the composite. Although higher amounts of 8YSZ lowered the furnace flash temperature, 25 vol% 8YSZ was sufficient to create a uniform microstructure.

Single phase Al_2O_3 and $LaPO_4$ did not flash under the maximum temperature and voltage used here, but the binary composites did, indicating that heterointerfaces may play a significant role in flash sintering as pathways for high current density.

Regions in the Al_2O_3–$LaPO_4$ sample where the temperature was close to the furnace temperature produced microstructures similar to conventionally sintered polycrystalline samples; channeled regions with the higher current that reached the highest temperature show nucleation and growth of large crystals of faceted alumina and non-faceted monazite; with lower current and lower temperature, large regions of relatively uniform eutectic microstructures can be formed in the channeled regions, presumably nucleated from the liquid phase.

More regular regions of the eutectic tend to form when the current density is higher while irregular eutectic forms when it is lower.

There is immiscibility of alumina and monazite even at elevated temperatures with a high interfacial energy between the two phases, as demonstrated by the eutectic microstructure. Flash sintering may have great potential in making eutectic structures without requiring ultra-high temperature melting in non-reactive crucibles.

CHAPTER 4 INVESTIGATION ON THE ALUMINA HEXAGONAL SINGLE CRYSTALS PRODUCED BY FLASH SINTERING

4.1 Abstract

The hexagonal alumina grains produced by flash sintering are investigated through electron microscopy characterization in this chapter, and crystallographic information obtained. The regular hexagonal alumina grains have been proven to be single crystal sapphire that facet on low-energy planes and grow along low-energy directions. The surface of equiangular and equilateral hexagonal grains are the basal planes of the hexagonal lattice, with the c-axis perpendicular to the viewing plane. The sides of the hexagonal grains grew to be pyramidal planes of the hexagonal crystal structure, which is the fast-growing direction for alumina crystals, contributing to the low aspect ratio of the crystals. Elongated hexagonal grains were found to have orientations that deviate from the c-axis, and the amount of deviation can be inferred from the grain morphology. Preferential wetting between monazite and the sapphire crystals, which presents as a pattern with three-fold symmetry, is due to the three-fold symmetry of the crystal structure of α-alumina.

4.2 Introduction

Al_2O_3 and $LaPO_4$ are good components for a composite material because the composite retains its refractory properties and has a higher fracture toughness than alumina. Flash sintering, a novel manufacturing technique, is used to densify composites of Al_2O_3 and $LaPO_4$. Results find that the system is a eutectic-forming system that also produces abnormally large sapphire crystals under suitable suitable conditions.

Alumina platelets have been added to composite materials as a strengthening mechanism due to their anisotropy and high strength. In the past, alumina platelets are synthesized or purchased and then added prior to sintering.[117,118] Alumina platelets with specific orientations have also been used to study the rate of grain growth along different crystallographic orientations.[119–121]

The results presented in this chapter investigate the crystallography and morphology of the highly faceted alumina crystals produced by flash sintering, and shed light on the growth process of this highly faceted crystal with asymmetric wetting of monazite.

4.3 Experimental

4.3.1 Flash sintering

The samples were processed from 50-50 vol.% $LaPO_4$-Al_2O_3 green bodies with flash sintering. Details of the flash sintering process are introduced in the previous chapter. Specifically, the current for flash sintering is controlled within an appropriate range (5-25 mA/mm^2) so that hexagonal alumina crystals will be produced. The furnace temperature was 1450°C and onset voltage was around 1080 V/cm.

4.3.2 Microstructure characterization

EBSD analysis in the SEM was done on alumina grains that formed on the surface, samples were coated with a few nanometers of carbon for this purpose, since metallic coatings led to weak signals and were not optimal. During EBSD, a 70° pre-tilt holder was used, and tilt correction was applied to the images.

FIB was used to cut out TEM samples for determining the orientation of the side planes of the crystals. Multiple samples shown in this chapter were cut out from the same hexagonal alumina grain from different orientations.

4.4 Results

Figure 4.1shows a BSE image of the surface of a 50-50 vol.% $LaPO_4$-Al_2O_3 flash sintered sample with typical microstructures, from both sides to the center of the image: polycrystalline region, eutectic microstructure and abnormal grain growth embedded in eutectic microstructures. The darker phases shown in the BSE contrast are alumina grains and the brighter grains are monazite grains. The hexagonal alumina grains can be both equilateral and equiangular, or it can be equiangular but with different edge lengths, which can appear as elongated grains. Both are common occurrences of flash sintered samples with alumina and monazite.

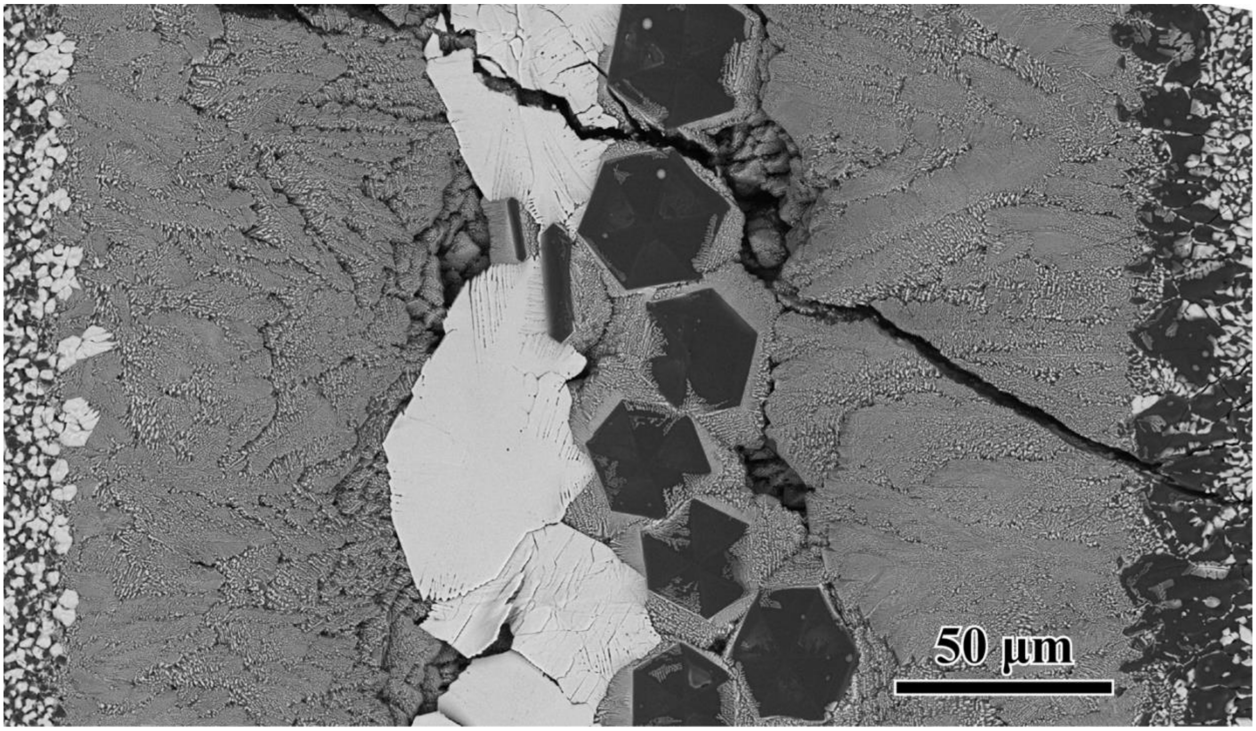

Figure 4.1: shows the typical microstructure of a flash sintered sample under conditions (1450°C, 1050 V/cm, 5mA/mm2, 8.5s)

Because the strong tendency of faceting in alumina crystals is often linked to specific crystallographic orientation in the crystal, EBSD was conducted to find the connection between the shapes and the orientations of the single crystal grains. Figure 4.2 shows the Euler color and pole figures of the alumina crystal. When the shape of the alumina crystal is closer to equilateral and equiangular, the orientation of the crystal represents its lattice structure, with the z-axis coming out of the viewing plane and the basal plane as the grain surface. When the alumina grain is more and more elongated, the orientation of the crystal deviates more and more from the Z axis. Figure 4.2 demonstrates this tendency with pole figures generated from the EBSD results.

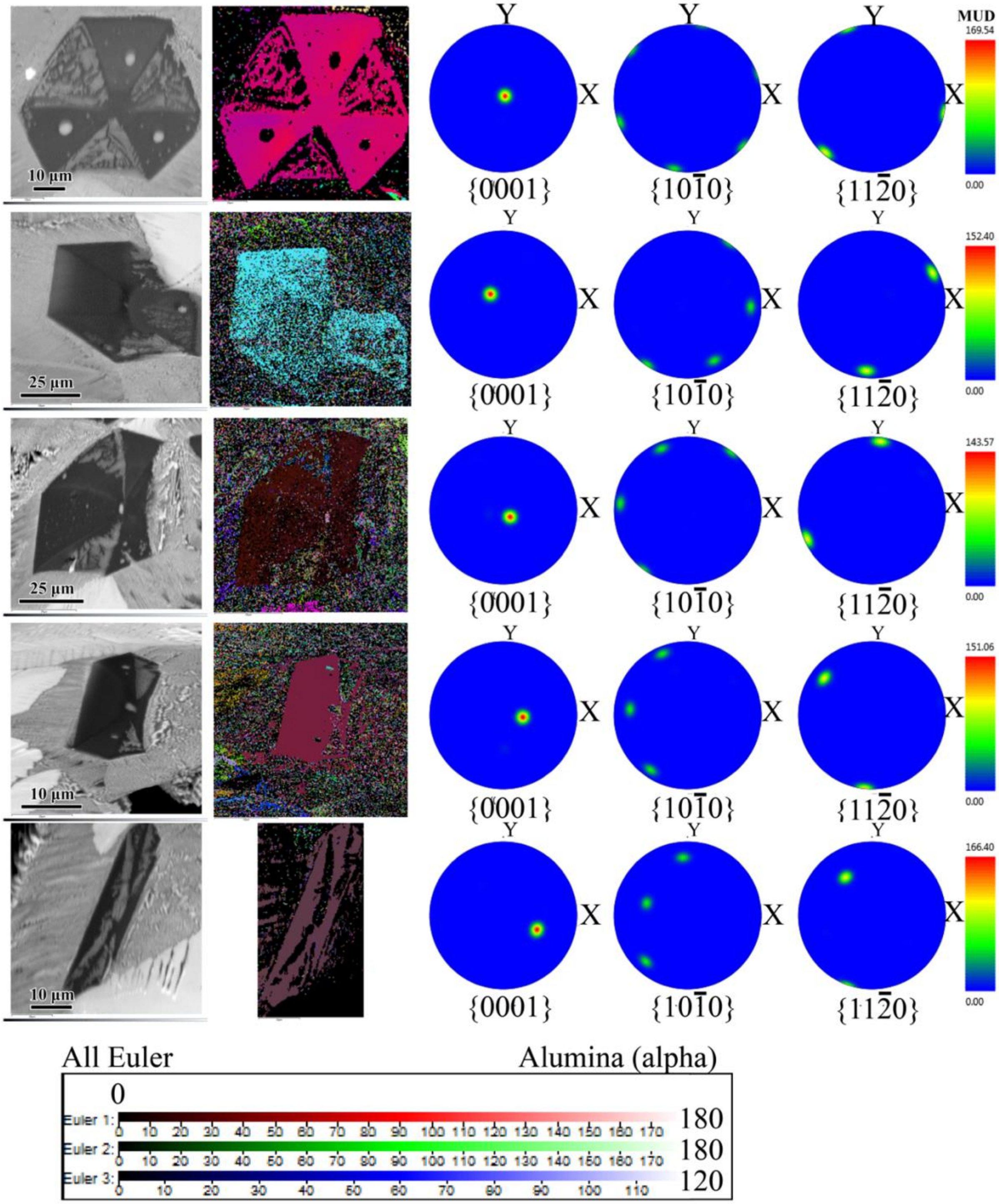

Figure 4.2: shows the EBSD results acquired. The Euler color of (b) is different because the grain is rotated 180°, but the pole figure shows the relative deviation from the regular hexagonal grains.

Overall EBSD results show that the alumina grains are single crystals. In some cases, the surface morphology has a minor effect on the analyzed orientation.

To further study the orientation of the crystals, specifically from the side, several FIB samples were made from the same hexagonal grain. As shown in Figure 4.3, the grain selected is embedded in a matrix of eutectics, which is representative of a random hexagonal sapphire grain. The TEM samples were cut perpendicular to the edges of the hexagon, to include part of the aluminum oxide grain and the eutectic structure next to and underneath it. The second and third sample avoided the ion-beam damaged area from the previous cut and used platinum to protect the top surface. FIB milling images reveals that edges of the hexagonal aluminum oxide grain are not perpendicular to the top surface (Figure 4.4) but have specific angles.

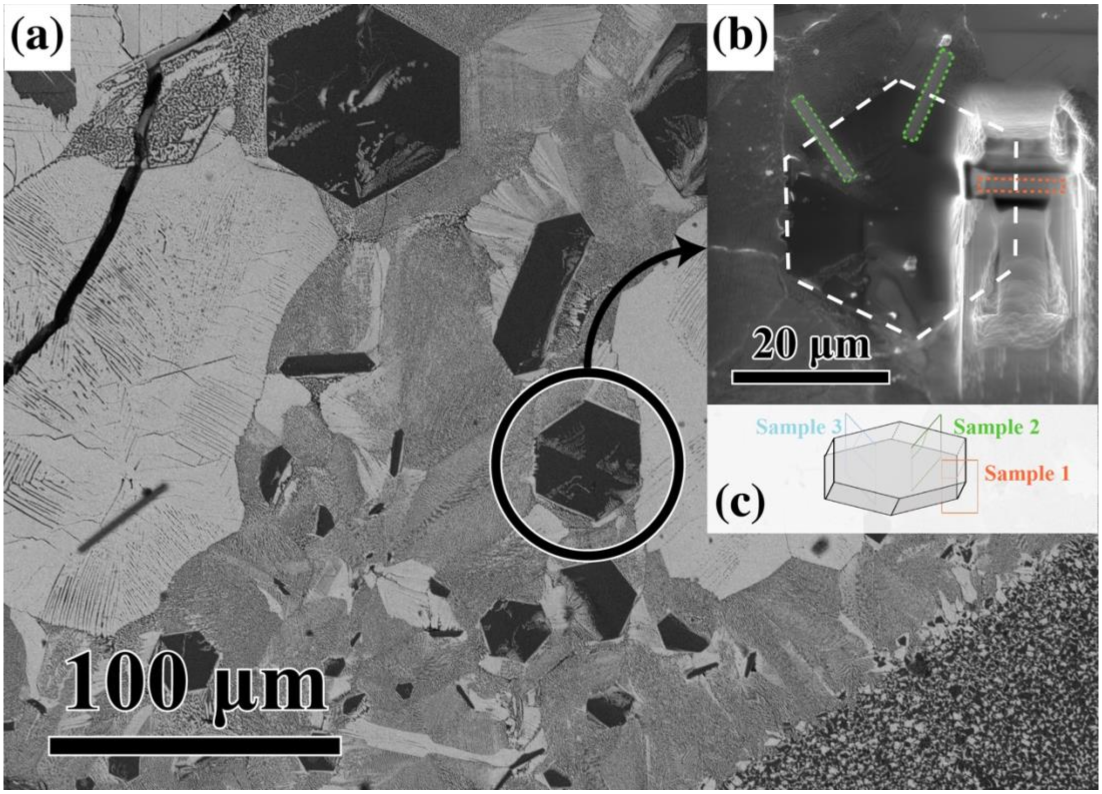

Figure 4.3: (a) A BSE image of the sample after flash sintering and before FIB, there are various sized hexagonal grains; (b) an SEM image of the selected grain with one FIB cut and two FIB locations marked by the Pt protection layer; (c) an illustration of where the TEM samples were obtained

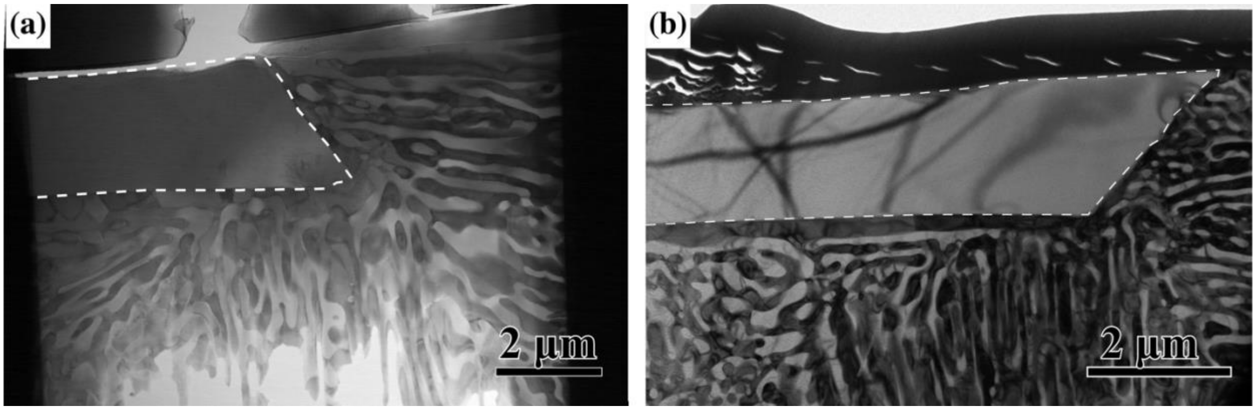

Figure 4.4: (a) STEM image of a cross-section of an alumina grain, showing an obtuse angle between the bottom and side of the grain; (b) TEM image of a cross-section of another alumina grain, showing an accute angle between the bottom and side of the grain.

Low magnification image in Figure 4.4 shows two samples, depending on the angle of the side plane the morphology shows the alumina grain to be either a trapezoid or an inverse trapezoid.

Within one sapphire grain different sides show different angles in respect to the top or bottom surface of the grain. The images below show the diffraction patterns obtained from three TEM samples cut from the same sapphire grain, as well as the diffraction patterns. Within a tilt angle of ±5°, the zone axes of <$\bar{1}$ $\bar{1}$ 2 0> was found, and diffractions obtained. Simulated diffraction patterns are also included to compare with the experimental. Some of the TEM and STEM images below are pieced together from more than 1 images due to limitations in the magnification. The diffraction results show that the edges of the regular hexagon grains are parallel to the a-directions of the hexagonal unit cell.

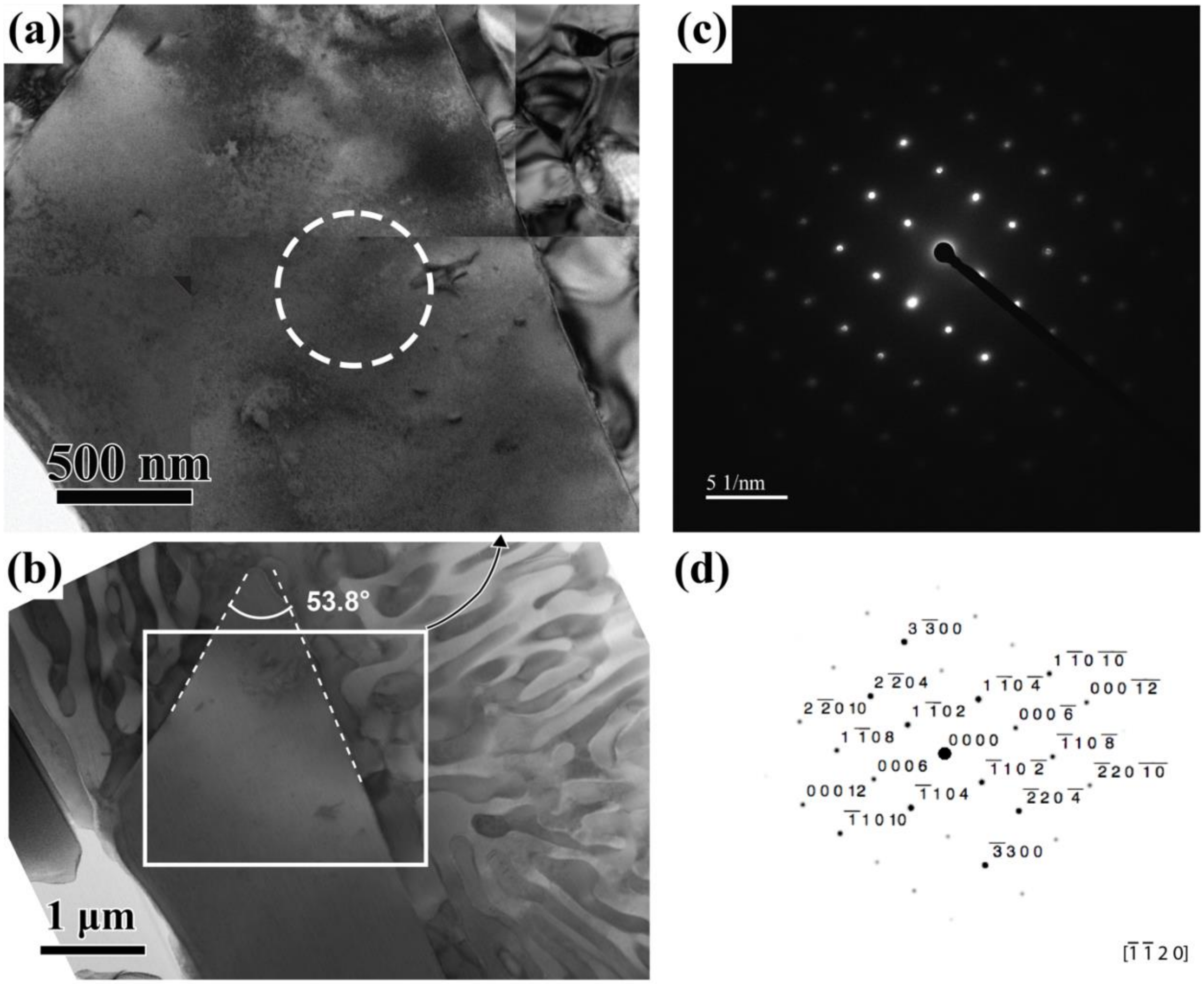

Figure 4.5: (a) BF TEM image (Sample 1 from Figure 4.3) of the alumina grain tilted to the zone axis, with the circle labeling the diffraction location. (b) the lower-magnification STEM image of the same grain, with the side surface angle labeled. (c) experimental diffraction pattern from the selected region, (d) the simulated diffraction pattern that match the experimental result.

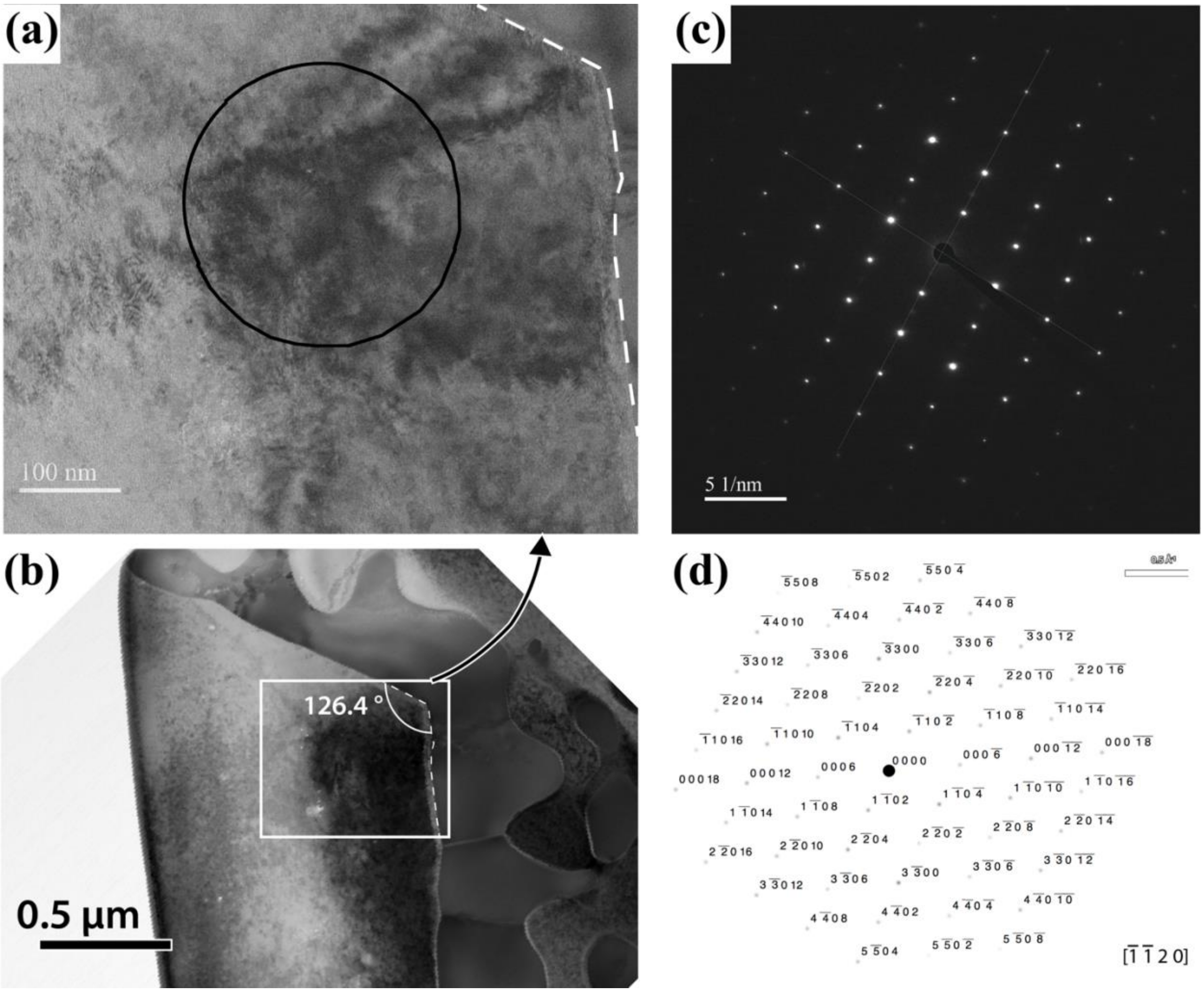

Figure 4.6: (a) BF TEM image (Sample 2 from Figure 4.3) of the alumina grain tilted to the zone axis, with the circle labeling the diffraction location. (b) the lower-magnification STEM image of the same grain, with the side surface angle labeled. (c) experimental diffraction pattern from the selected region, (d) the simulated diffraction pattern that match the experimental result.

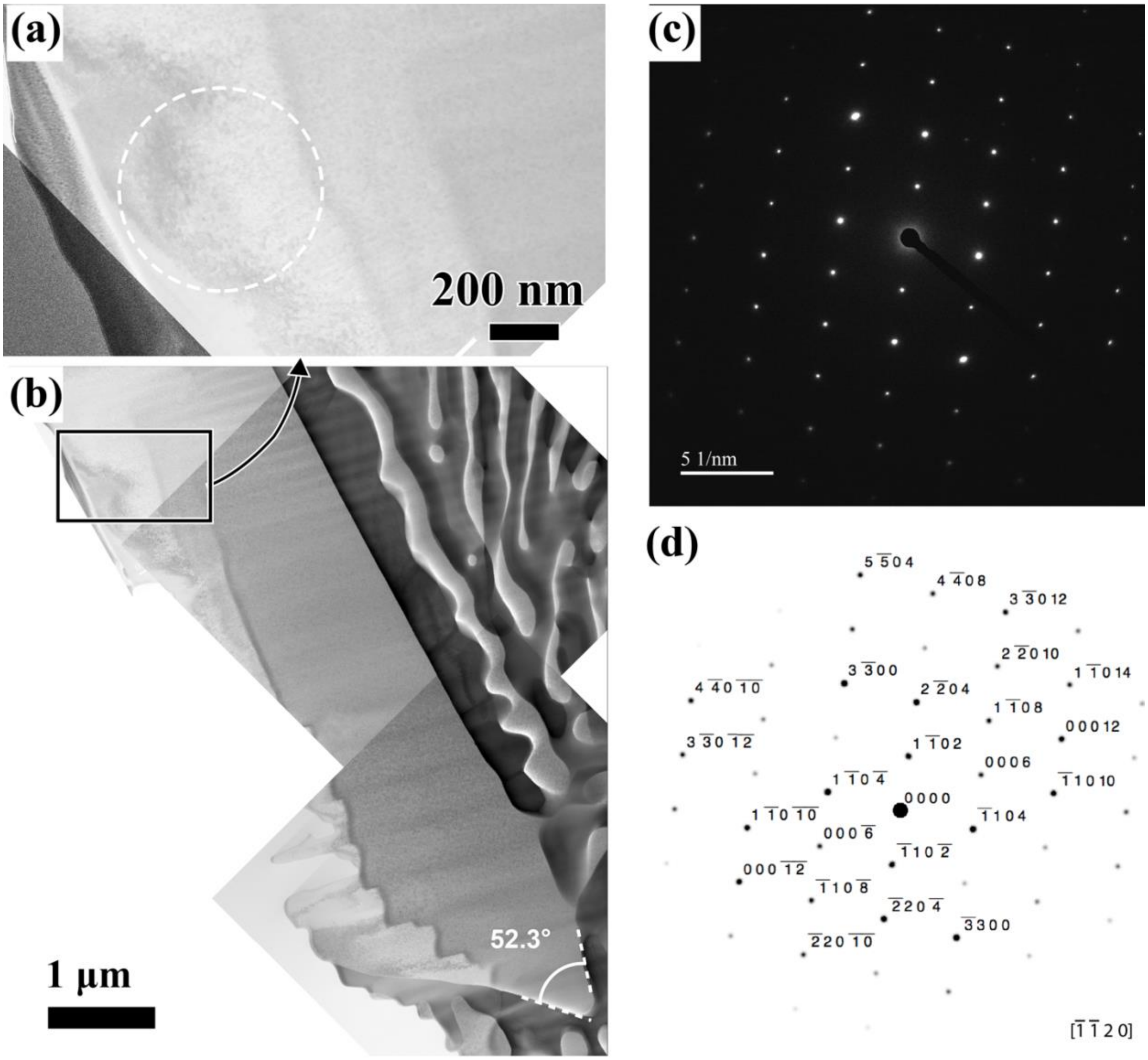

Figure 4.7: (a) BF TEM image (Sample 3 from Figure 4.3) of the alumina grain tilted to the zone axis, with the circle labeling the diffraction location. (b) the lower-magnification STEM image of the same grain, with the side surface angle labeled. (c) experimental diffraction pattern from the selected region, (d) the simulated diffraction pattern that match the experimental result.

It can also be observed that the bottom surface of the alumina grain is often a straight, clean facet, except when the monazite phase is polycrystalline, which can lead to grooved grain boundaries.

In the EBSD results, most of the alumina grains show up as a single crystal, but some TEM diffraction reveal some different orientations in the alumina grain, as shown below.

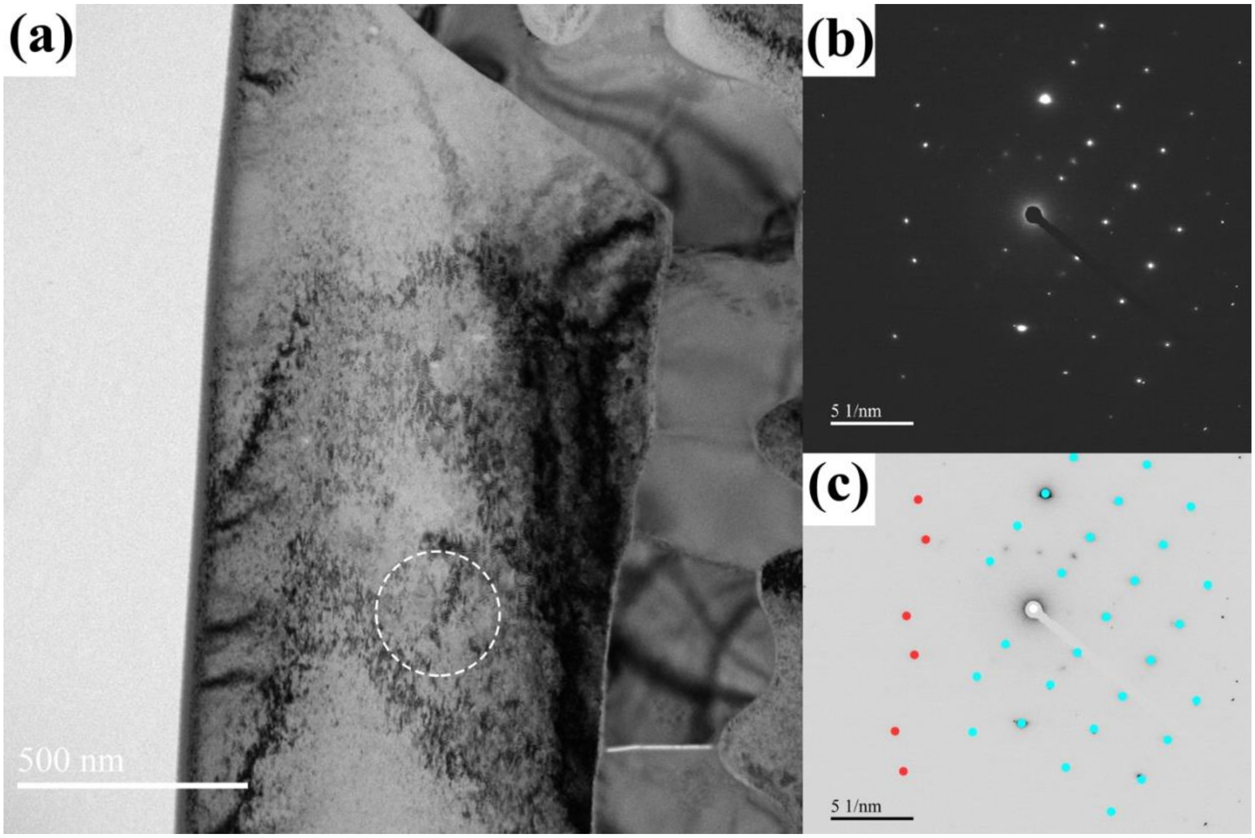

Figure 4.8: (a) BF TEM image (Sample 2 from Figure 4.3) of the alumina grain tilted to the $\{\bar{1}\ \bar{1}\ 2\ 0\}$ zone axis, with the circle labeling the diffraction location. (b) experimental diffraction pattern from the selected region, (c) two sets of diffraction patterns are marked with different colors

In the SEM images, the non-wetting behavior of monazite on the surface of the sapphire crystals is observed. In the hexagonal grains, the surface segregates into two types of features. One type of feature has thin monazite “strands” filling the majority of a triangular area, with alternate triangles containing either almost no monazite or monazite “balling up” into a circle on the surface. The first feature indicates partial wetting between the two phases while the second indicates higher interfacial energy and poor wetting. The two types of features often show up in alternating triangular areas on top of the hexagonal grains, and monazite is on the surface of the grains only, confirmed by FIB milling. Figure 4.9 shows this characteristic of these grains.

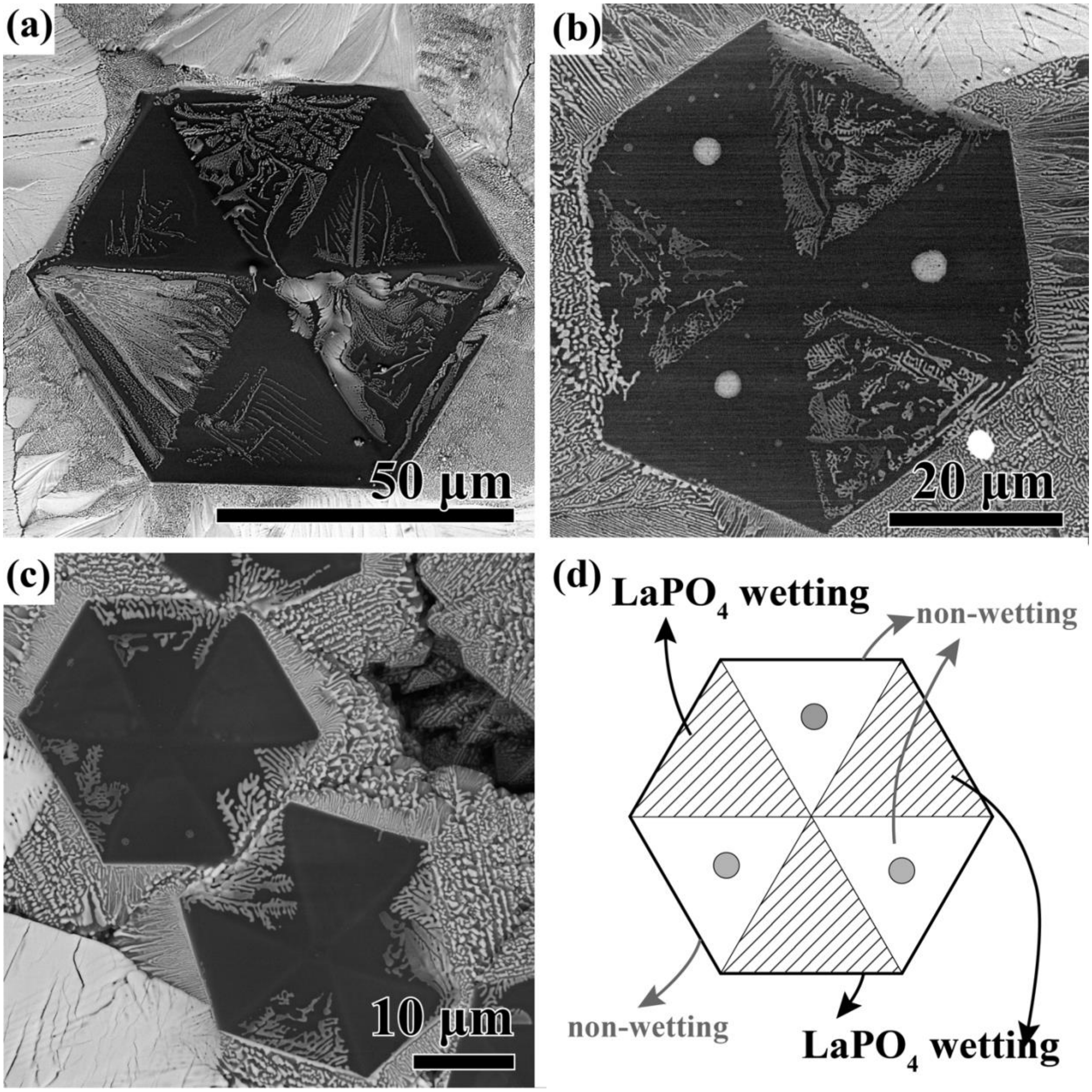

Figure 4.9: (a)-(c) show SEM images of hexagonal sapphire grains commonly found on samples flash sintered with different parameters; (d) shows an illustration of the alternating wetting behavior.

It can also be observed that the direction of the eutectic microstructure immediately adjacent to the sapphire single crystals have specific relationships with the sapphire crystals, as shown in Figure 4.9 (c). The eutectic microstructures next to the "non-wetting" triangles tend to be perpendicular to the hexagon edges while the eutectics next to the "partial wetting" triangles did not show such tendencies.

4.5 Discussions

4.5.1 Grain orientations can be inferred from the grain morphologies

The shape of an equilateral or elongated grain is indicative of the crystalline orientation of the grain. Figure 4.10 illustrates how the different shapes of grains can result from faceting along different angles relative to the equilateral hexagonal grains. The more perpendicular the faceted surface is to the basal plane, the more elongated the grains appear.

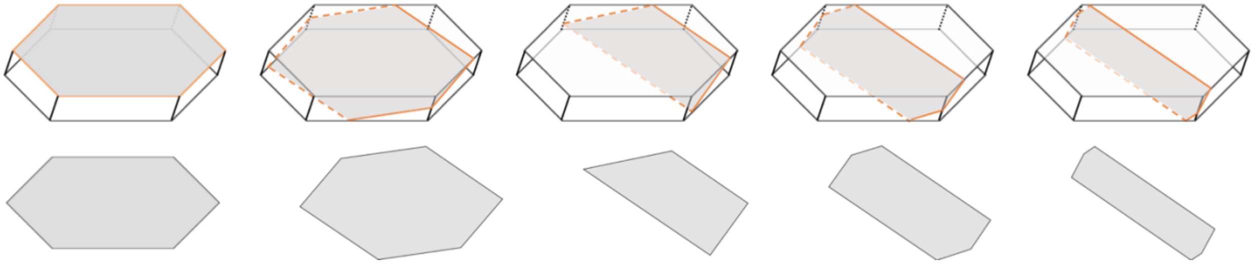

Figure 4.10: Illustrations of how the orientation affects the surface morphology of sapphire grains.

Figure 4.11 shows a full view of one elongated grain, the bottom half of which exposed due to pores and the void around it. On the top slender surface, the SE contrast shows that complicated surface morphology has formed to accommodate the high-energy faceting orientation which led to the elongated shape of this grain. The wider side surface, however, lacks contrast that indicate surface morphology, and thus can be inferred to be one of the low-energy planes.

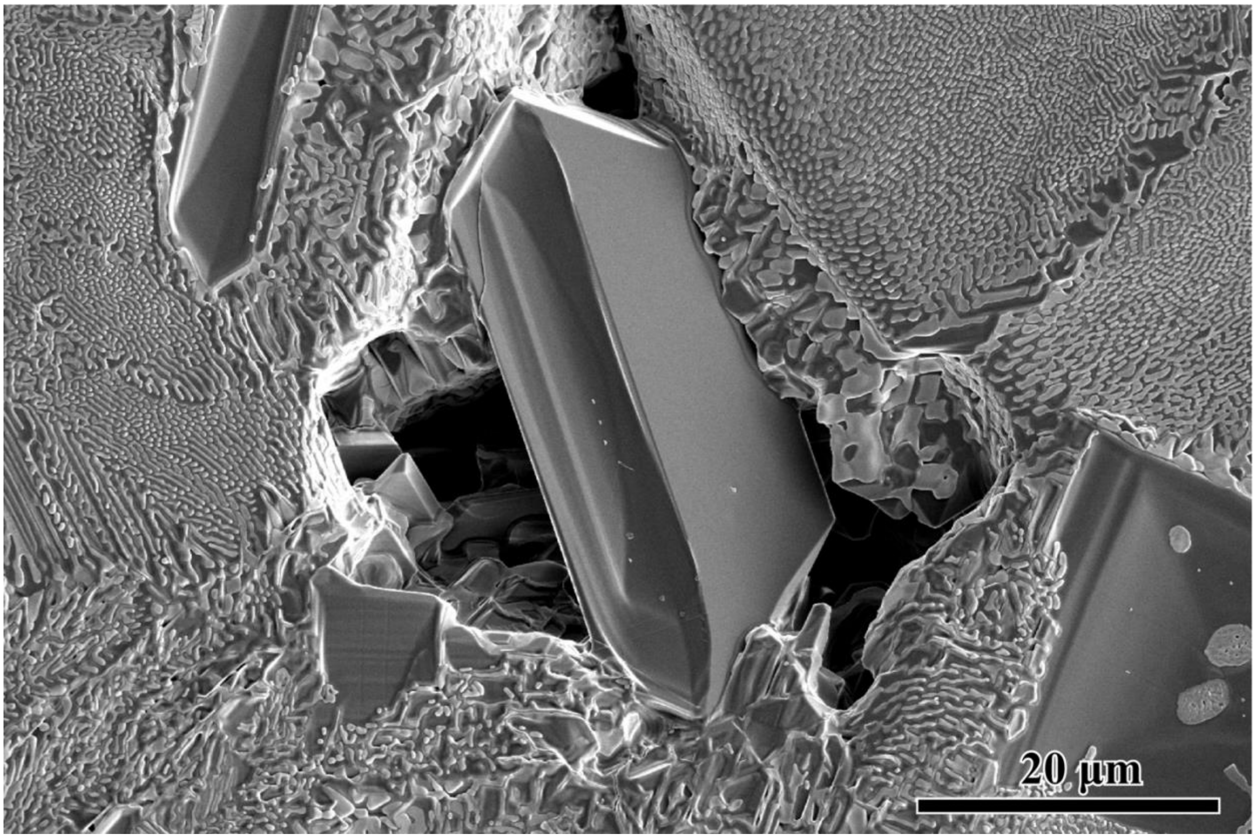

Figure 4.11: An elongated alumina grain, the bottom half of which is exposed by pores.

From the hexagonal alumina grains studied, the aspect ratio of the regular equilateral grains is often larger than 20, leading to a wide and flat polyhedron. The top and bottom surfaces of the alumina grains is often a pinacoid of the form {0 0 0 1}, being a parallel pair of planes. The opposing sides of the crystal can have forms of either domes or sphenoids, which requires further research to confirm. What is known from the electron diffraction, is that the side planes often are the {1 $\bar{1}$ 0 2} pyramidal planes of sapphire. The theoretical angle between the basal plane and the pyramidal planes can be calculated, the angle is 57.6° between (0 0 0 1) and (1 $\bar{1}$ 0 2), and 122.4° between (0 0 0

1) and $(1\ \bar{1}\ 0\ \bar{2})$. The angles measured between the bottom and side planes of the regular hexagonal are 53.8°, 126.4°, and 52.3° for samples 1-3, respectively, which match fairly well. The discrepancies can come from errors induced in the FIB process, or that the side plane is not perfectly aligned with the hexagon edges, potentially to accommodate the monazites around it.

4.5.2 The crystal morphology can be attributed to the difference in growth rates along different orientations

It has been shown in past studies that the growth rate of different planes for aluminum oxide varies greatly, which is the main contributor to platelet growth and grain morphologies in doped alumina. The surface energy between alumina and monazite has not been quantitatively measured or studied regarding specific orientations, and growth rate of different planes have not been quantified either. However, it is reasonable to infer qualitative relationships between the surface energies and growth rate of different planes based on results from this study.

The surface energies of $\{0\ 0\ 0\ 1\}$ and $\{1\ \bar{1}\ 0\ 2\}$ planes are low for sapphire in a monazite or eutectic matrix. This can be concluded from the strong tendency of faceting along these planes. This could also apply to the interfacial energy of sapphire in a monazite or eutectic melt, given the estimated local temperature of the flash sintering process is often above the melting point of either alumina or monazite. The growth rate of $\{1\ \bar{1}\ 0\ 2\}$ planes is inferred to be much faster than that of $\{0\ 0\ 0\ 1\}$ planes, because of the high aspect ratio. This conclusion echoes with the studies done on sapphire in doped compounds and in molten salt.[122–126]

4.5.3 Structural symmetry and surface termination may be the deciding factor of the wetting behavior

The alternating triangular areas of wetting and non-wetting behavior of monazite on sapphire surfaces represent the three-fold symmetry of the alumina unit cell. α-alumina belongs to space group 167 ($R\bar{3}c$), which has a three-fold roto-inversion axis. This three-fold symmetry is expressed by the surface chemistry and surface termination of the sapphire crystal, which decides the wetting behavior of monazite. Reflective diffraction can help verify the surface termination in future experiments.

The preferential wetting behavior also appears on elongated grains, with some surfaces crowded by monazite while others completely clean, as shown in Figure 4.12. This may be attributed to the difference in surface termination also. It is hypothesized that the surface termination of the non-wetting regions are Al-terminated, which is charge neutral and autocompensated, and the wetting regions are O-terminated, as broken bonds for the surface O atoms needs available cations to charge neutralize.[127]

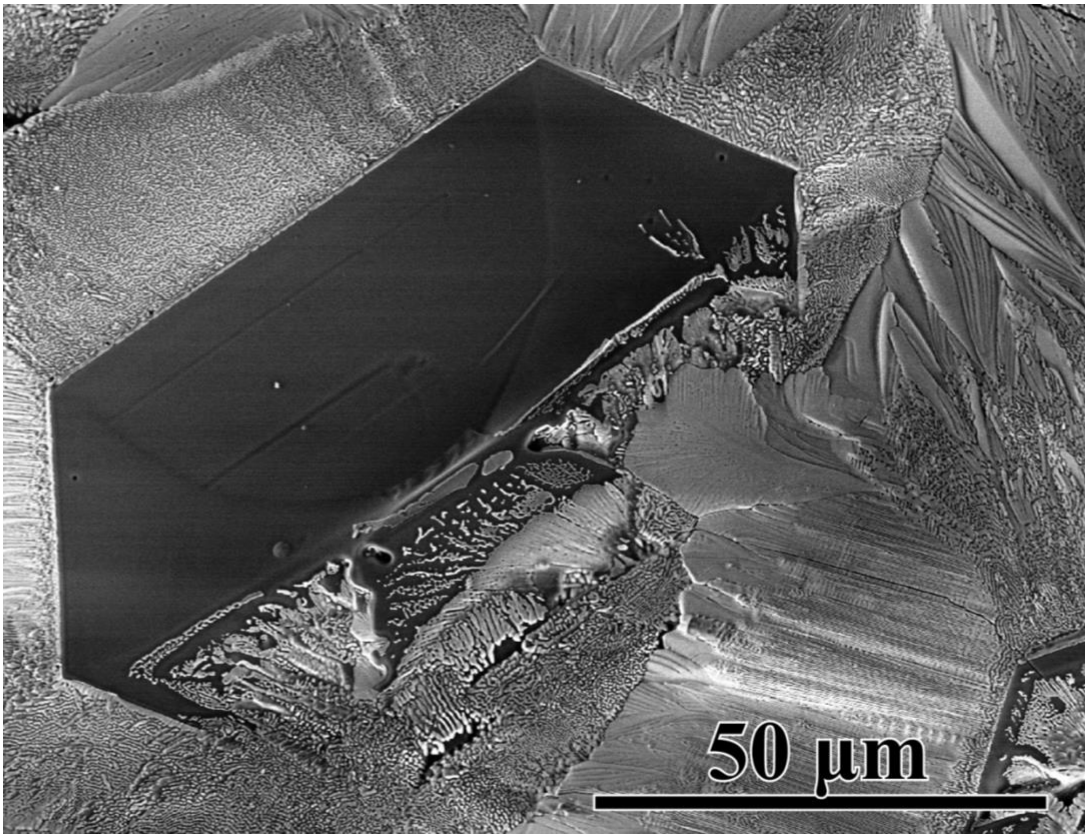

Figure 4.12: An elongated grain showing the preferential wetting of monazite.

4.5.4 Flash sintering can directly make alumina platelets in a composite material

Traditionally, alumina platelets are manufactured first through aqueous synthesis or other means, then added as a reinforcement or a second phase material. The flash sintering process in this study started with a mixture of alumina and monazite powders and directly produced alumina platelets in the composite. This eliminated a separate manufacturing step and has great potential for forming sapphire platelets. Figure 4.13 shows the possible process of sapphire single crystals growing from the melt as well as the $LaPO_4$ large grains.

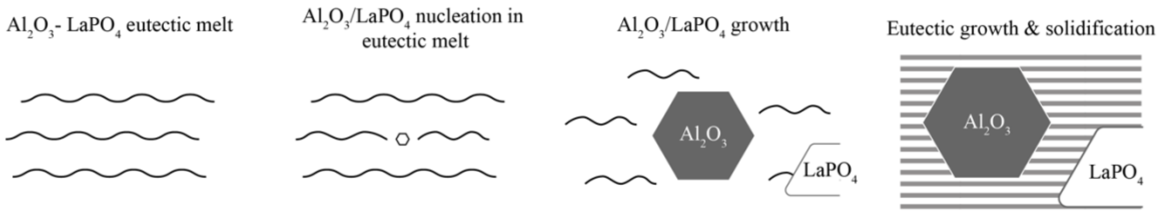

Figure 4.13 Schematics of the sapphire grains growing from a eutectic liquid during flash sintering

4.6 Conclusions

- The morphology of the hexagonal alumina grains can be attributed to the crystalline orientation. When the surface is the basal plane, the grains appears as equilateral and equiangular hexagons; when the surface orientation deviates from the basal plane, the grains appear more and more elongated and less equilateral.
- TEM diffraction confirms the side surfaces of the hexagonal grains are the $\{1\ \bar{1}\ 0\ 2\}$ planes, and the edges on the surface of the hexagon are parallel to the a-axes of the hexagonal unit cell.
- The preferential wetting of monazite on the sapphire surface represents the three-fold symmetry of the crystal structure of α-alumina, which very likely led to specific surface terminations and surface chemistry.

Future work can be done to further understand the specifics of the surface chemistry through reflection electron diffraction or other surface techniques such as XPS. Flash sintering presents a promising method to produce alumina platelets in-situ, which can improve efficiency and reduce cost of adding a strengthening phase.

CHAPTER 5 CONSTRUCTION OF A EUTECTIC PHASE DIAGRAM FROM THE Al_2O_3-$LaPO_4$ MICROSTRUCTURE

5.1 Abstract

Microstructures of the Al_2O_3-$LaPO_4$ composites produced by flash sintering confirms that this is a eutectic-forming system. The construction of a eutectic phase diagram is been explored in this chapter. The solid solubility of the two phases were measured experimentally through EDS in STEM, the eutectic temperature of the system inferred from high-temperature DSC experiments, and eutectic composition of the system deducted from the microstructures of this system. CALPHAD calculations of the system was also conducted but did not produce satisfying results due to a lack of reliable experimental data in the databases.

5.2 Introduction

Methods for determining phase diagrams have been established in the literature, either through experimental means or thermodynamic calculations.[128–130] The thermodynamic calculations reply on Gibbs free energy values from established databases. Thermocalc, one such program for these calculations, is one approach to determine the Al_2O_3-$LaPO_4$ phase diagram. However these programs use databases from experimental systems and data is lacking for the four element system Al-La-P-O. (The Thermocalc database TCOX10 was used, but as will be shown, was insufficient.) Experimental methods that are commonly used to determine phase diagram with melting and crystallization transitions include high temperature differential scanning calorimetry (DSC), thermogravimetric analysis (TGA), and other high temperature analysis such as high temperature electron microprobe x-ray analysis.[131,132] Appropriate thermodynamic measurements are typically at slow heating rates of 5°C to ensure data accuracy in past studies. For experimental studies of binary phase diagrams (or in this case the quasi-binary of Al_2O_3–$LaPO_4$), samples are made of different amounts of the starting constituents, then heated to determine when melting occurs. Melting is an endothermic phenomenon, so it will be displayed as a DSC as a trough. Exothermic events will be displayed as a peak. TGA is often used in connection with DSC to ensure sublimation is not occurring but all element stay as liquids or solids. After that samples are made and cooled to room temperature, microstructural studies can show which phase nucleate first and if any eutectics form.

5.3 Experimental Methods

5.3.1 STEM imaging and EDS analysis

The starting material is a mixture of Al_2O_3-$LaPO_4$ powders, thoroughly mixed and pressed into a dog-bone shaped green body. The samples are made from flash sintering, with specific details discussed in previous chapters. The flash sintered material was then cut by focused ion beam and TEM samples were made through milling. The FIB lamellae were from chosen sites of different samples, either with monazite or alumina abnormal grain growth on the surface. The samples were observed with scanning transmission electron microscopy and EDS data was collected from alumina grains and monazite grains in the sample.

The EDS data was analyzed with the Cliff-Lorimer ratio method. The Cliff-Lorimer ratio states that for a thin sample, the integrated EDS peak intensity and the atomic percentages of two elements satisfy the following relationship:

$$\frac{I_A}{I_B} = k_{A-B}{}^{-1} \cdot \frac{n_A}{n_B} \qquad \text{Equation 5.1}$$

Where I_A and I_B are the EDS intensities of A and B elements, while n_A and n_B are the atomic percentages of A and B elements, respectively. k_{A-B} is the Cliff-Lorimer factor between elements A and B. To study the unknown solid solubility of Al_2O_3 and $LaPO_4$ in each other, a known standard of $LaAlO_3$ is first tested to establish k_{Al-La}. k values between other elements were also established, such as k_{O-La} and k_{O-Al}, which were verified by analyzing results from single-phase $LaPO_4$ and Al_2O_3 samples. Pure single crystal $LaAlO_3$ was purchased commercially (MTI Corp., USA), milled into a FIB lamella and tested under the same condition as the composite materials. All STEM and EDS data were obtained with the JEOL JEM-2800 TEM at IMRI.

5.3.2 High temperature DSC

The sample analyzed is the starting powder of the ceramic composite, three compositions were tested first up to 1550°C: 25-75 vol. % Al_2O_3–$LaPO_4$, 50-50 vol. % Al_2O_3–$LaPO_4$, and 75-25 vol. % Al_2O_3–$LaPO_4$. The samples were tested with thermogravimetric analysis and differential scanning calorimetry (TG/DSC) at IMRI (STA 449 F3 Jupiter®, NETZSCH, Germany). Samples were placed in alumina crucibles and heated to 1550°C with 10°C/minute, then the temperature is held for 20 minutes before cooling with 10°C/minute to room temperature. This test was done in an atmosphere of 28.6% O_2 – 71.4% N_2 simulating air with an empty reference.

High-temperature TG/DSC testing was then done commercially (SETSYS Evolution, KEP technologies, France). Powders of 50-50 vol. % Al_2O_3–$LaPO_4$ were tested. The measurement was run with the powders in a tungsten crucible under helium atmosphere, also with a blank crucible as baseline. The thermo profile used for this test is the following: 25°C to 1450°C at 50°C/minute, 1450°C to 2150°C at 10°C/minute, and dwell at 2150°C for 2 minutes before cooling.

5.3.3 CALPHAD simulation

Calculations of the eutectic phase diagram was based on data from database TCOX10 in ThermoCalc. The Gibbs free energies of Al_2O_3, $LaPO_4$ and the liquid solution phase with various compositions were exported at temperatures from 500 K to 3000 K. Both solid phases are considered intermetallic compounds with no solid solubility. At each temperature, the equilibrium composition of the liquid phase is determined following the common tangent construction with both the solid phases using Matlab, as demonstrated in Figure 5.1.

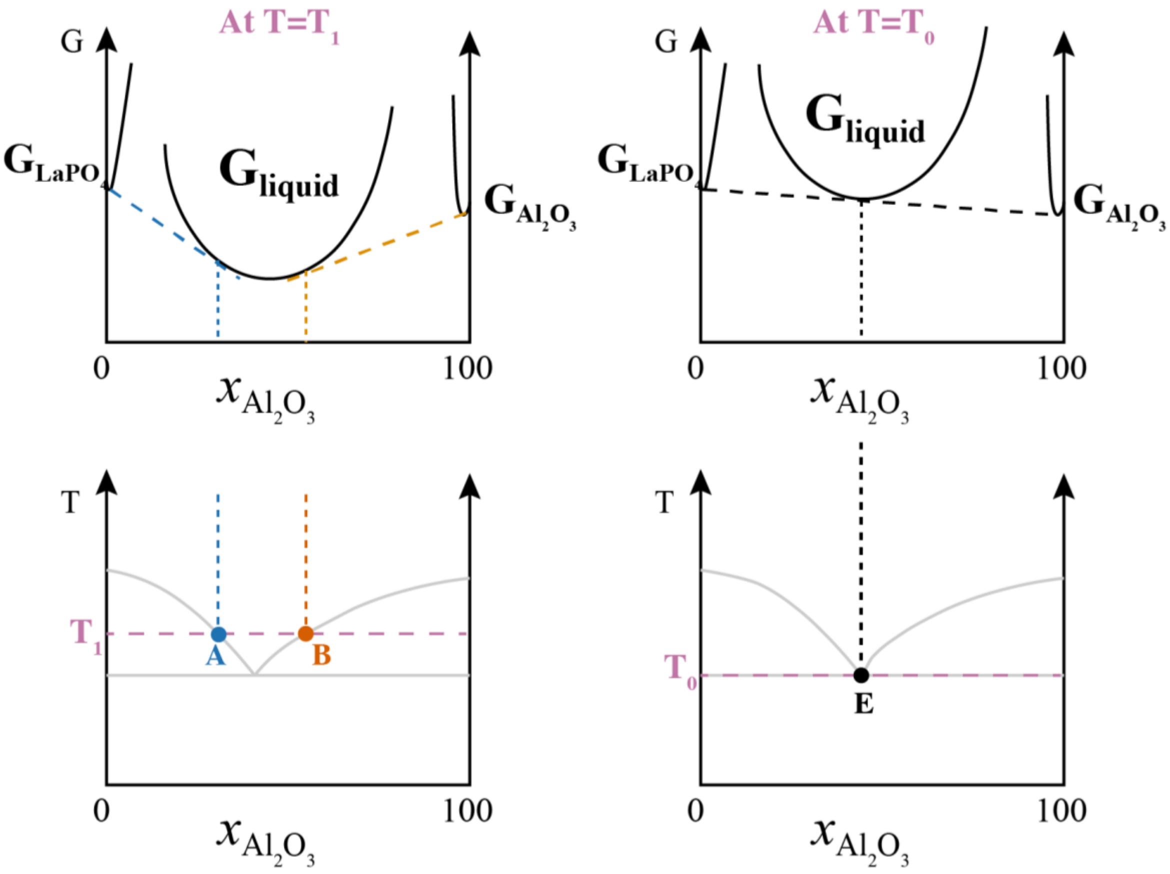

Figure 5.1 An illustration showing the process of deciding the equilibrium composition of a liquid phase at a set temperature. According to the common tangent of the Gibbs free energy curves, points A and B are under equilibrium at T_1; the eutectic point E (T_0) has the same common tangent between the three free energy curves.

To verify the validity of the calculation, the B-FeB phase diagram was calculated with the same method. This system is well-established with no solid solubility in either phase also, therefore a suitable benchmark. Data for this system is exported from the TCFE10 database in ThermoCalc.

5.4 Results

5.4.1 Limited solid solubility

According to the EDS results from $LaAlO_3$ and $LaPO_4$ standards, the following k_{A-B} values were obtained and used for subsequent calculations, as listed in Table 5.1.

Table 5.1 The Cliff-Lorimer ratio k established from single-phase $LaAlO_3$, $LaPO_4$ and Al_2O_3 standards.

Types of k	Value of $k_{A-B} = (\frac{n_A}{n_B})/(\frac{I_A}{I_B})$
$k_{O-La\,(L)}$	5.1
$k_{Al-La\,(L)}$	2.9
$k_{P\,(K)-La\,(L)}$	2.8
k_{O-Al}	1.8

The EDS spectra were acquired from various locations in the sample, as shown in Figure 5.2. There was an average amount of 0.3 at% Al in $LaPO_4$ grains and 0.0 at% La in Al_2O_3 grains, both of which within error range of the EDS system and therefore negligible. There was also no difference in the results from the large grain on the surface and that from the corresponding phase in the eutectic microstructure. It can be concluded that there is negligible solid solubility for either Al in $LaPO_4$ or La in Al_2O_3, if any.

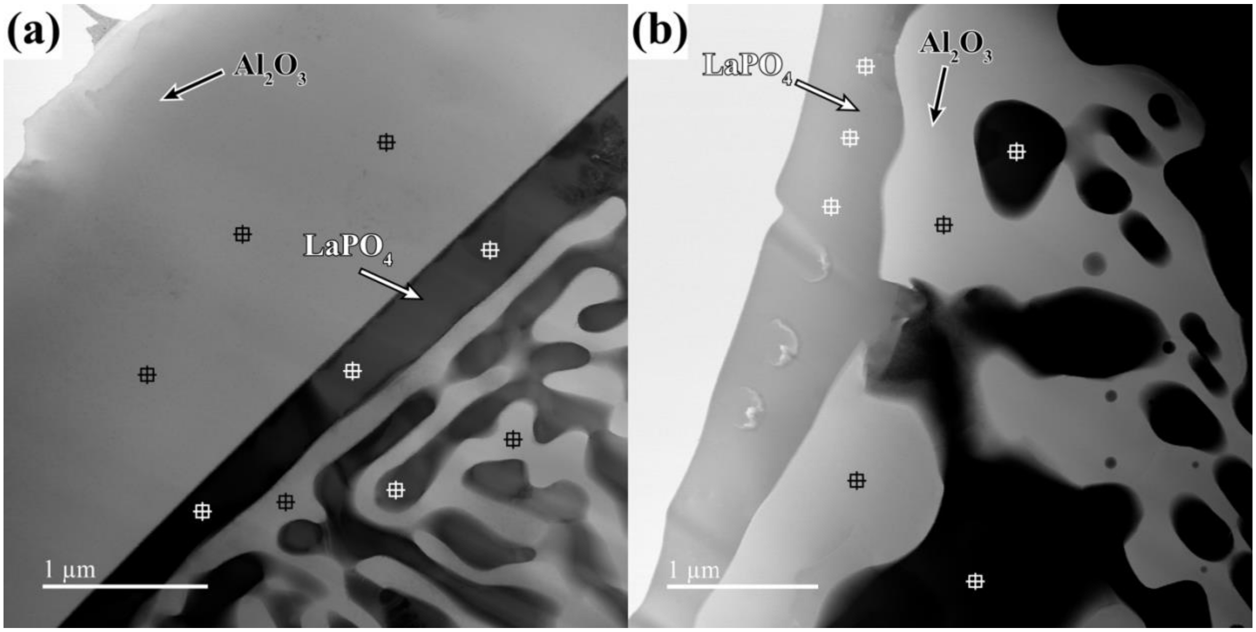

Figure 5.2 STEM images of samples with eutectic microstructure and (a) Al_2O_3 single crystal on the surface and (b) $LaPO_4$ grain on the surface. Point EDS were acquired at various locations, with the markers labeling several examples.

5.4.2 High temperature DSC results

DSC/TGA experiments up to 1550°C did not show any signs of melting in any of the 3 composites tested. At lower temperature of around 300°C, a mass loss of 2-6% was reported with a low endothermic effect for each of the three compositions. At 1205-1260°C, a mass loss of 0-2% was observed in one of the two 50-50 vol. % Al_2O_3–$LaPO_4$ power samples, accompanied by an endothermic effect.

The TG/dTG data from one 50-50 vol. % Al_2O_3–$LaPO_4$ power sample is shown in Figure 5.3 and DSC/TGA data in Figure 5.4 and Figure 5.5. Above 1550°C, 4 endothermic events and 2 mass loss events were recorded in the 50-50 vol. % Al_2O_3–$LaPO_4$ power sample tested. Between 1550°C and 1965°C, a gradual weight loss happens, then an evident mass drop at 1974.4°C, for a total of 13.2% before the sample retained mass until 2020°C. The gradual mass decrease is accompanied by an endothermic effect at 1887.8°C, and the evident mass drop is accompanied by an endothermic effect at 1971.3°C.

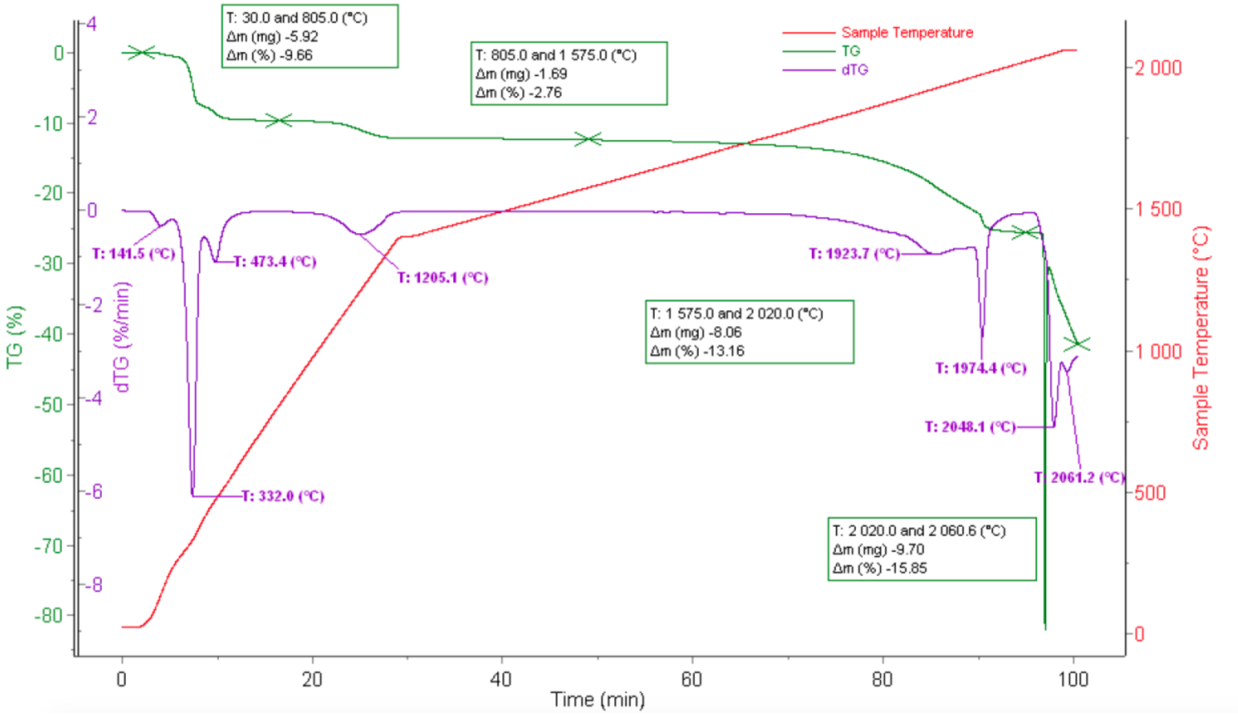

Figure 5.3 TGA and dTG signals recorded versus sample temperature and time during the heating ramp

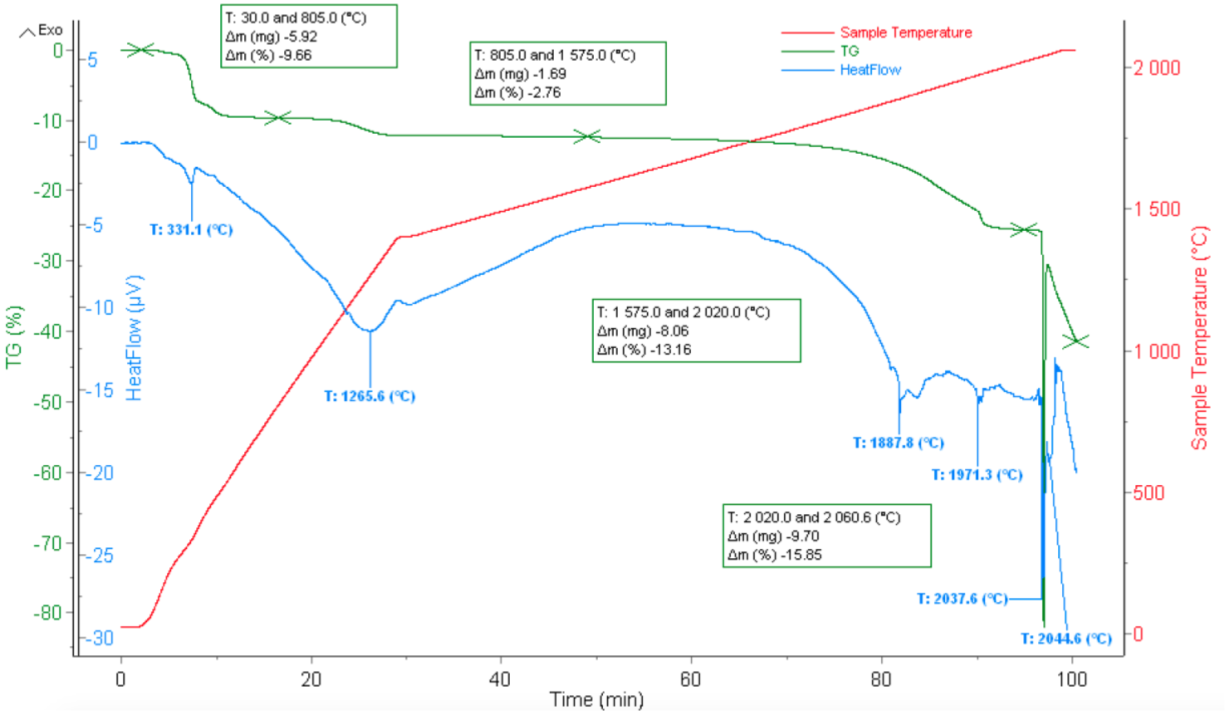

Figure 5.4 TGA and DSC signals recorded versus sample temperature and time during the heating ramp – Initial mass : 61.22mg

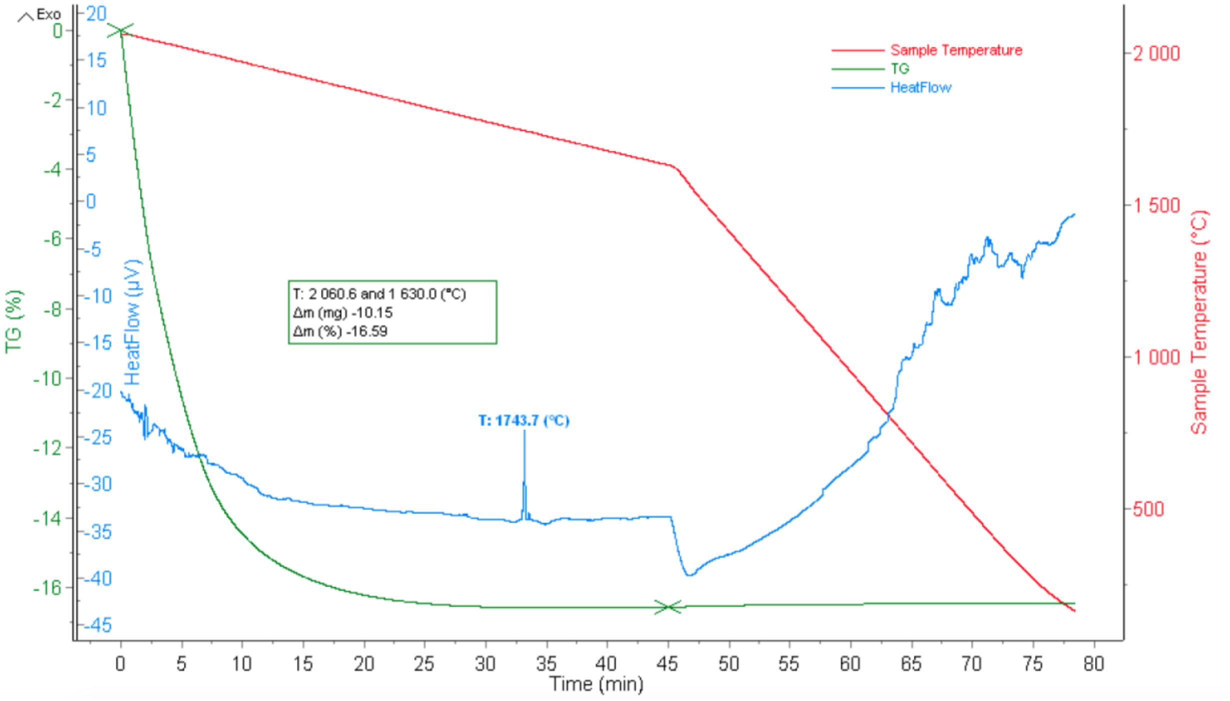

Figure 5.5 TGA and DSC signals recorded versus sample temperature and time during the cooling ramp

As the temperature keeps rising, around 2037°C, a rapid drop in mass can be observed with a large endothermic peak, followed by a rapid mass gain. This is indicative of sublimation or evaporation of the material, which then redeposited onto the rod inside the instrument causing the mass gain. The mass loss resumes and continues through the rest of the test cycle (dwell and cooling), which led to a total weight loss of 97%. The remaining 3% of material was analyzed by SEM EDS and is mainly consisted of SiO_2 and C, with a limited amount of Al, as shown in Figure 5.6.

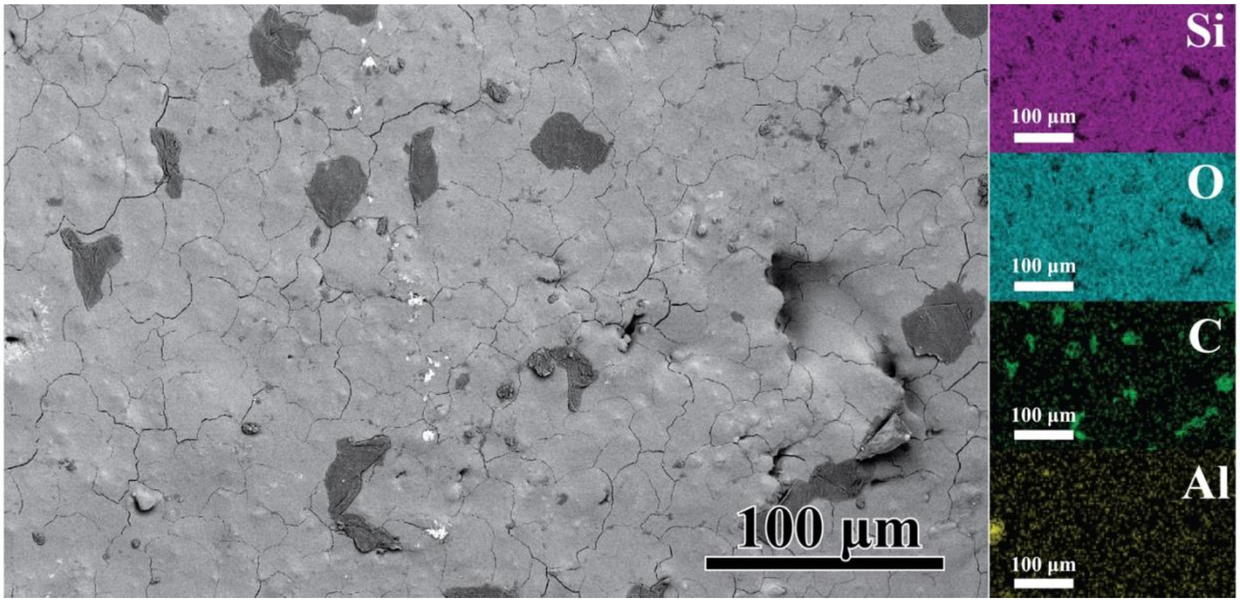

Figure 5.6 BSE image and EDS maps of the residue from the high temperature DSC/TGA measurement

5.4.3 Simulated phase diagrams

As a test, the calculated B-FeB phase diagram was simulated and its comparison with the established diagram from the database are shown in Figure 5.7. The two diagrams match well and verifies the calculation process is effective.

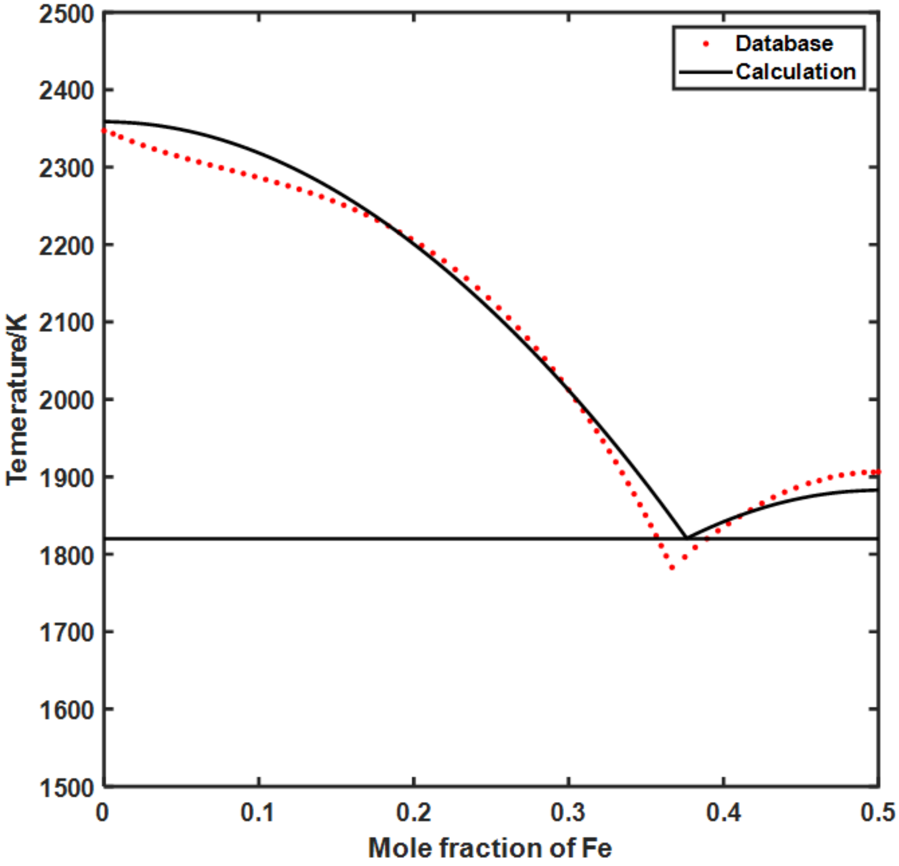

Figure 5.7 Comparison between the established phase diagram of B-FeB from Thermocalc database and the calculated phase diagram from the exported Gibbs free energy

The calculated phase diagram of Al_2O_3-$LaPO_4$ based on exported Gibbs free energy is shown in Figure 5.8. The system is predicted to reach the eutectic melting temperature at 1589.5°C, and the eutectic composition is predicted to be 68–32 vol.% $LaPO_4$–Al_2O_3. This contradicts the microstructure observed after flash sintering experiments for composites with various compositions, which is closer to a 50/50 vol.%, and does not match the high-temperature DSC results either, as discussed later.

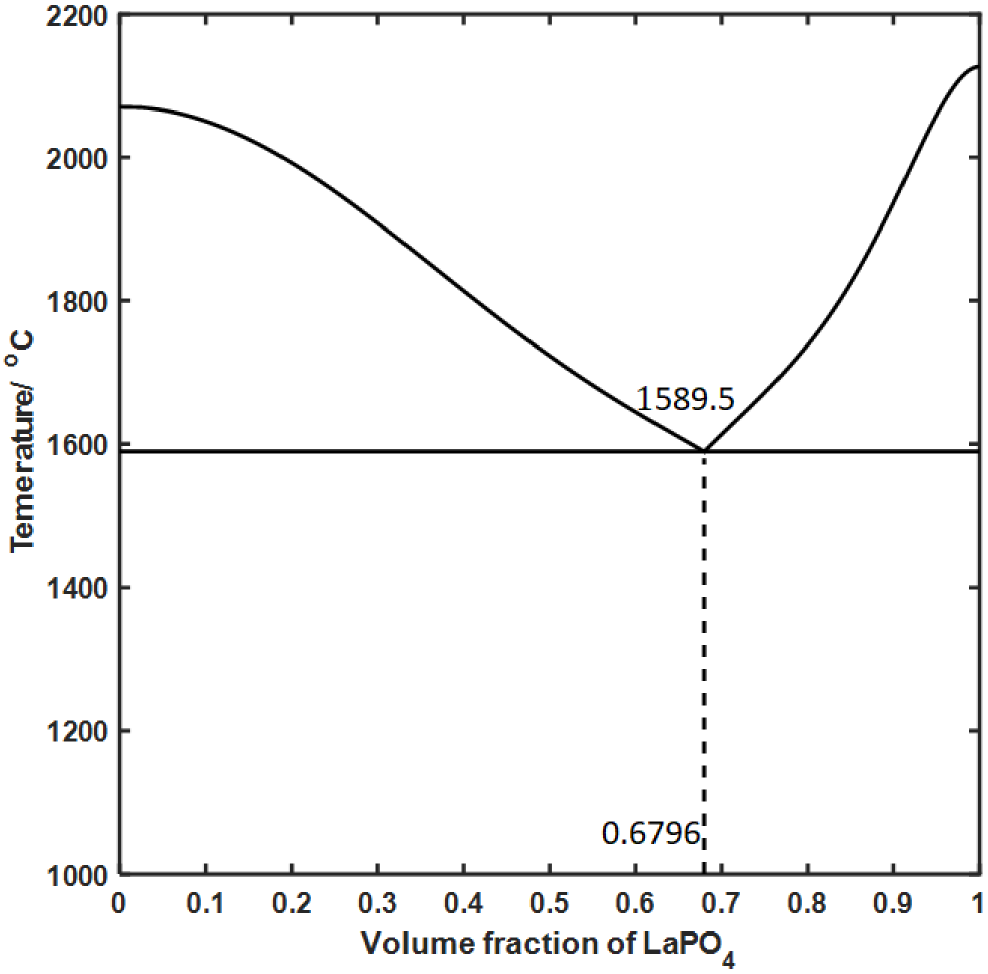

Figure 5.8 The calculated phase diagram of Al_2O_3-$LaPO_4$

5.5 Discussions

5.5.1 Solid solubility of the Al_2O_3-$LaPO_4$ system

The results from this study concluded that there is no detectable solid solubility between Al_2O_3 and $LaPO_4$, which agrees with previous research on this subject.[18] Morgan *et al.*[18] tested the compatibility of Al_2O_3 and $LaPO_4$ up to 1750°C, and confirmed the solubility to be <1%. Moreover, no eutectic or peritectic liquid was observed by

Morgan *et al.*[18] up to 1750°C, which confirms the eutectic microstructure found in this study formed at a temperature even higher.

5.5.2 Eutectic temperature of the Al_2O_3-$LaPO_4$ system

The calculated eutectic temperature was incorrect, which is likely due to the inaccurate Gibbs free energy data from the database. Thermodynamic data for multi-element ceramic systems (in this case with 4 elements La-Al-P-O) is commonly lacking or inaccurate. However, the eutectic temperature may be inferred from the high-temperature DSC data. In theory, a eutectic melt is an endothermic reaction without mass loss or mass gain, and the endothermic event at 1887.8°C in the DSC data best fits this description. According to the DSC results, there are two endothermic events above 1750°C and below 2037.6°C (temperature of sublimation). At 1971.3°C a rapid mass drop accompanies the endothermic event, and at 1887.8°C there is only gradual weight loss. Due to the lower rate of weight loss (dTG), a temperature close to 1887.8°C is more likely to be the eutectic temperature of the Al_2O_3-$LaPO_4$ system.

Other events detected by the DSC data may be explained as well. Monazite $LaPO_4$ often contains impurity phases that have excess phosphorous which have low-melting points. A common impurity phase is $La(PO_3)_3$ which melts at around 1235°C[133]. This can explain the activities between 1205.1°C and 1265.6°C. During cooling of the system, there is an exothermic event at 1743.7°C which may be the recrystallization of SiO_2. Not only did the EDS results point to the remaining existence of SiO_2 in the system, but also because the melting point of SiO_2 is around 1710-1730°C, within reasonable error range. It is possible that SiO_2 as an impurity is introduced during high temperature testing, as there are parts in the instrument that are silica.[134]

5.5.3 Eutectic composition of the Al_2O_3-$LaPO_4$ system

The eutectic composition of the Al_2O_3-$LaPO_4$ system is inferred to be around 50-50 vol.% Al_2O_3-$LaPO_4$ based on microstructural analyses of the eutectic. Figure 3.7 shows the microstructure produced when the composition of the system deviates from the eutectic composition: hypereutectic and hypoeutectic systems will produce grains of the proeutectic phase. Figure 3.6 shows that with 50-50 vol.% Al_2O_3-$LaPO_4$ there is no proeutectic grains from either phase, and Figure 3.11(c) shows the same behavior with lower magnification. It can be inferred that 50-50 vol.% Al_2O_3-$LaPO_4$ (43.8-56.2 wt% Al_2O_3-$LaPO_4$ or 64.1-35.9 at% Al_2O_3-$LaPO_4$) is very close to the eutectic composition, if not exactly.

3D sectioning of the eutectic structure below the surface was done to explore how homogeneous the structure was, in case proeutectic phases solidified within the bulk of the material. No proeutectic grains were found in any of the cross-sections and confirms the bulk of the flash sintered region is consisted of only eutectic microstructures. A video of the 3D sectioned material can be found here.

5.5.4 Reconstructed eutectic phase diagram

It’s known in past literature that the melting temperature of Al_2O_3 is 2030°C and 2070°C for monazite.[105,106] Based on results from this study, the eutectic phase diagram of Al_2O_3-$LaPO_4$ can be constructed as shown in Figure 5.9, with solubility below the limits of EDS detection.

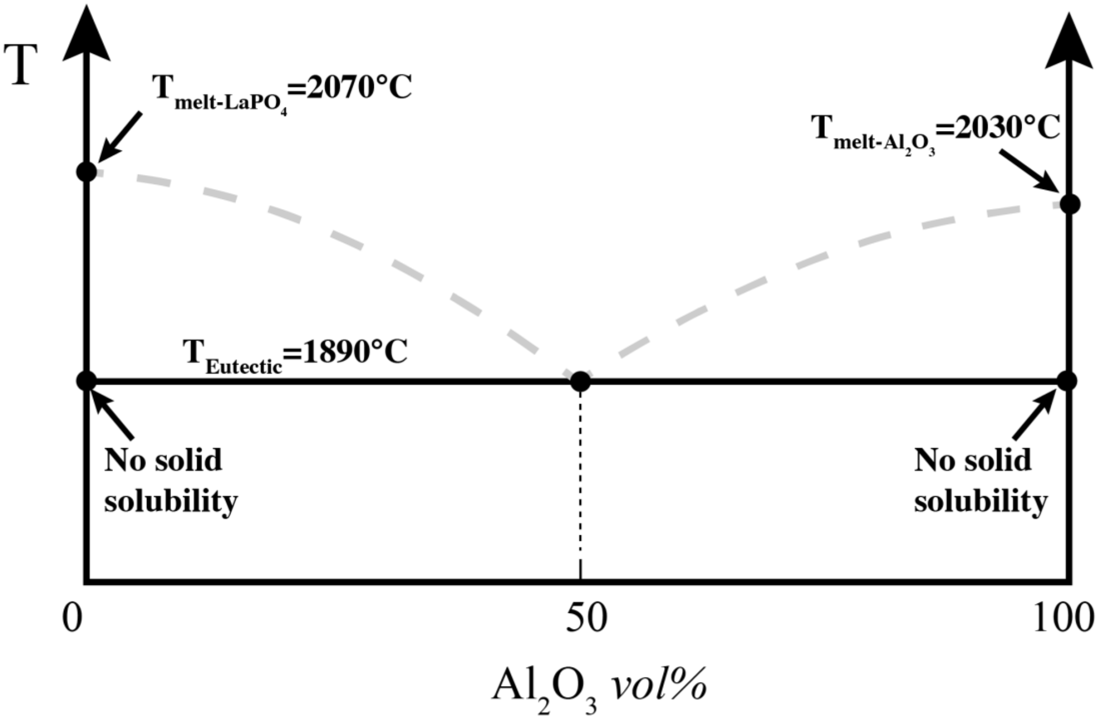

Figure 5.9 Constructed eutectic phase diagram for Al_2O_3-$LaPO_4$, dashed liquidous likes are only an illustration of possible curvature.

5.6 Conclusions

- There is no significant solid solubility between Al_2O_3-$LaPO_4$ even at elevated temperatures above 1750°C.
- Eutectic temperature of the Al_2O_3-$LaPO_4$ system is likely 1890°C.
- The eutectic composition of the Al_2O_3-$LaPO_4$ is approximately 50-50 vol.% Al_2O_3-$LaPO_4$ (43.8-56.2 wt% Al_2O_3-$LaPO_4$).
- Sublimation of Al_2O_3-$LaPO_4$ can happen above 2020°C, specifically at 2037.6°C in this study.

CHAPTER 6 MECHANICAL PROPERTIES OF THE EUTECTIC MICROSTRUCTURE

6.1 Abstract

The mechanical properties of the microstructures of Al_2O_3-$LaPO_4$ produced by flash sintering are evaluated in this chapter. Specifically, hardness values of eutectic microstructures with different layer thickness and corresponding polycrystalline microstructures were measured and calculated. The hardness for eutectic microstructures were superior compared to the polycrystalline microstructures, and there was no obvious difference between the hardness values of eutectics with different layer thicknesses. The hardness measured for this system exhibit characteristics of reverse indentation size effect, where higher indenting loads lead to higher measured values.

6.2 Introduction

The mechanical properties of ceramic materials with eutectic microstructures are often superior to the conventional polycrystalline microstructures.[115,135,136] Different mechanisms can contribute to the improvement of hardness and fracture toughness. For example, eutectic microstructures of the Al_2O_3-ZrO_2 composites deflect cracks through the interface, and form rod-like pull out features when the material fails.[136] Usually, these eutectic microstructures are formed by completely melting two immiscible phases, which requires very high temperatures and non-reactive containers.

$LaPO_4$ as the potential matrix for a ceramic composite material, is known to form debonding weak interfaces and improve the fracture toughness of the composite Al_2O_3-

$LaPO_4$ compared to a Al_2O_3 single phase.[18,137] Al_2O_3-$LaPO_4$ composites with eutectic microstructures therefore has great potential for superior mechanical properties.

6.3 Experimental Methods

Flash sintering was conducted on a 50-50 vol.% $LaPO_4$-Al_2O_3 dog-bone sample at a furnace temperature of 1450°C with an electric field of 1100 V/cm, 25 mA/mm^2 that was held for 12 s. On the surface of the sample, $LaPO_4$ and Al_2O_3 grains with abnormal grain growth were produced, embedded in a matrix of eutectic microstructures. In order to expose the eutectic microstructures, the sample surface was ground down and polished to 0.5 μm using diamond lapping films (Ted Pella, Inc., USA). After polishing, the surface exposed had no large single-phase grains and were consisted of either polycrystalline grains or eutectic microstructures.

The Hardness (HV) measurement was done using a microhardness indenter (Micromet5101, Buehler, USA). Vickers indentation was conducted with loads of 10 gf, 50 gf, 100 gf, and 200 gf. The areas of indentations were illustrated in Figure 6.1. There was no visible difference in the microstructural features longitudinally, although the widths of the channeled region vary – the width of the fine eutectic structures range from 360 μm to 440 μm longitudinally.

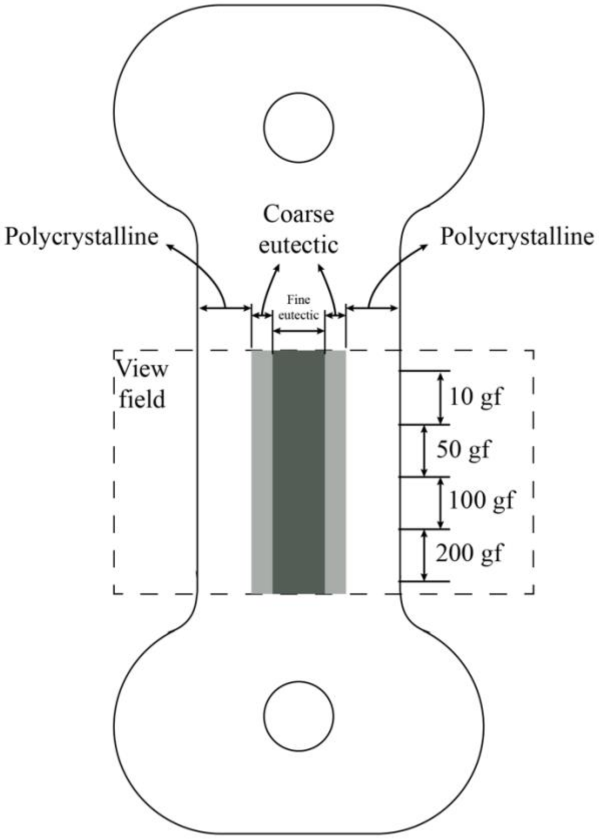

Figure 6.1 Sketch of polished flash-sintered dog-bone sample, the regions with polycrystalline and eutectic microstructures are labeled. Indentations of different loads were done along the longitudinal direction.

Hardness was then calculated using the following equation:

$$HV = 0.0018544 \times \frac{P}{\overline{D}^2} \qquad \text{Equation 6.1}^{138,139}$$

where HV is the Vickers hardness value in GPa, P is the force in N, and $\overline{D}$ is the mean diagonal length of the indentations in mm $(D_1 + D_2)/2$. Examples of indentations done on eutectic and polycrystalline microstructures are shown in Figure 6.2.

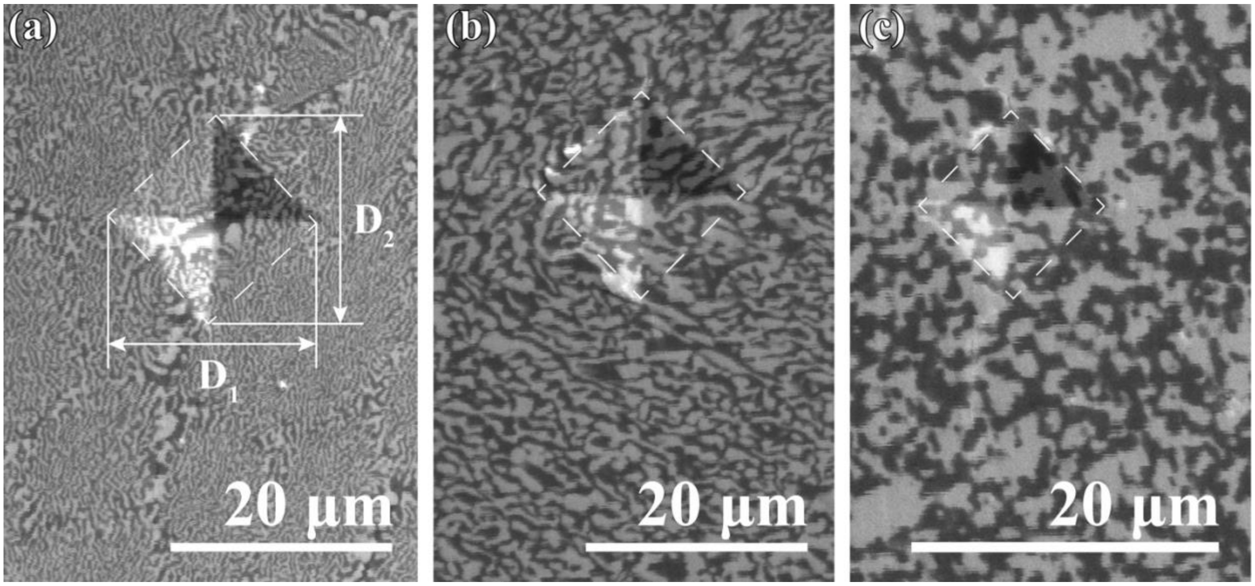

Figure 6.2 Examples of Vickers indentation on various microstructures: (a) fine eutectic microstructure (100 gf), (b) coarse eutectic microstructure (100 gf), and (c) polycrystalline microstructure (10 gf).

6.4 Results

6.4.1 Predicted Vickers hardness for 50-50 vol.% $LaPO_4$-Al_2O_3

According to past literature, the Vicker's hardness value of Al_2O_3 is 16.5 GPa, and 5.7 GPa for $LaPO_4$[22]. The hardness of 50-50 vol.% $LaPO_4$-Al_2O_3 can be predicted by the upper and lower bounds from the rule of mixtures.

Upper-bound value $$HV_{U-composites} = f_1 \cdot HV_1 + (1 - f_1) \cdot HV_2$$ Equation 6.2[138]

Lower-bound value $$HV_{L-composites} = (\frac{f_1}{HV_1} + \frac{1-f_1}{HV_2})^{-1}$$ Equation 6.3[138]

Where $f_1 = 50\%, HV_1 = 16.5\ GPa, and\ HV_2 = 5.7 Pa$. The calculated Vickers hardness for the composite is within 8.47~11.1 GPa.

6.4.2 Measured Vickers hardness for 50-50 vol.% $LaPO_4$-Al_2O_3

The microstructures on the polished surface and the corresponding Vickers hardness results obtained are shown in Figure 6.3. An overview of the whole sample surface is shown in the log-magnification SEM image of Figure 6.3 (g). In the images, the darker phase is Al_2O_3 and the brighter phase is $LaPO_4$. Figure 6.3 (d) shows the microstructure of the center-most region of the sample, which is a fine eutectic microstructure with thicknesses on the scale of ~100 nm. Figure 6.3 (i) show the hardness values of the indents acquired according to their lateral positions relative to this fine eutectic region. The origin of the x axis in Figure 6.3 (i) is set to the left edge of the fine eutectics, negative x values represent indents to the left and positive x values represent indents to the right. Both the left and right edges of this center most region are labeled with black dashed lines in Figure 6.3 (h) and black dotted lines in Figure 6.3 (i). Outside of this fine eutectics region are regions with coarse eutectics on both sides. The widths of these coarse eutectic areas vary and they are labeled with white dashed lines in Figure 6.3 (h), and colored dotted lines in Figure 6.3 (i). The boundaries in Figure 6.3 (i) are color-coded to match the legends of the corresponding indents. The layer thicknesses of these coarser eutectics range from sub-micron scale to a few microns. Despite the difference in layer thicknesses between the fine and coarse eutectic microstructures, no prominent differences in the hardness values were observed, as hardness values within the colored boundaries show in Figure 6.3 (i).

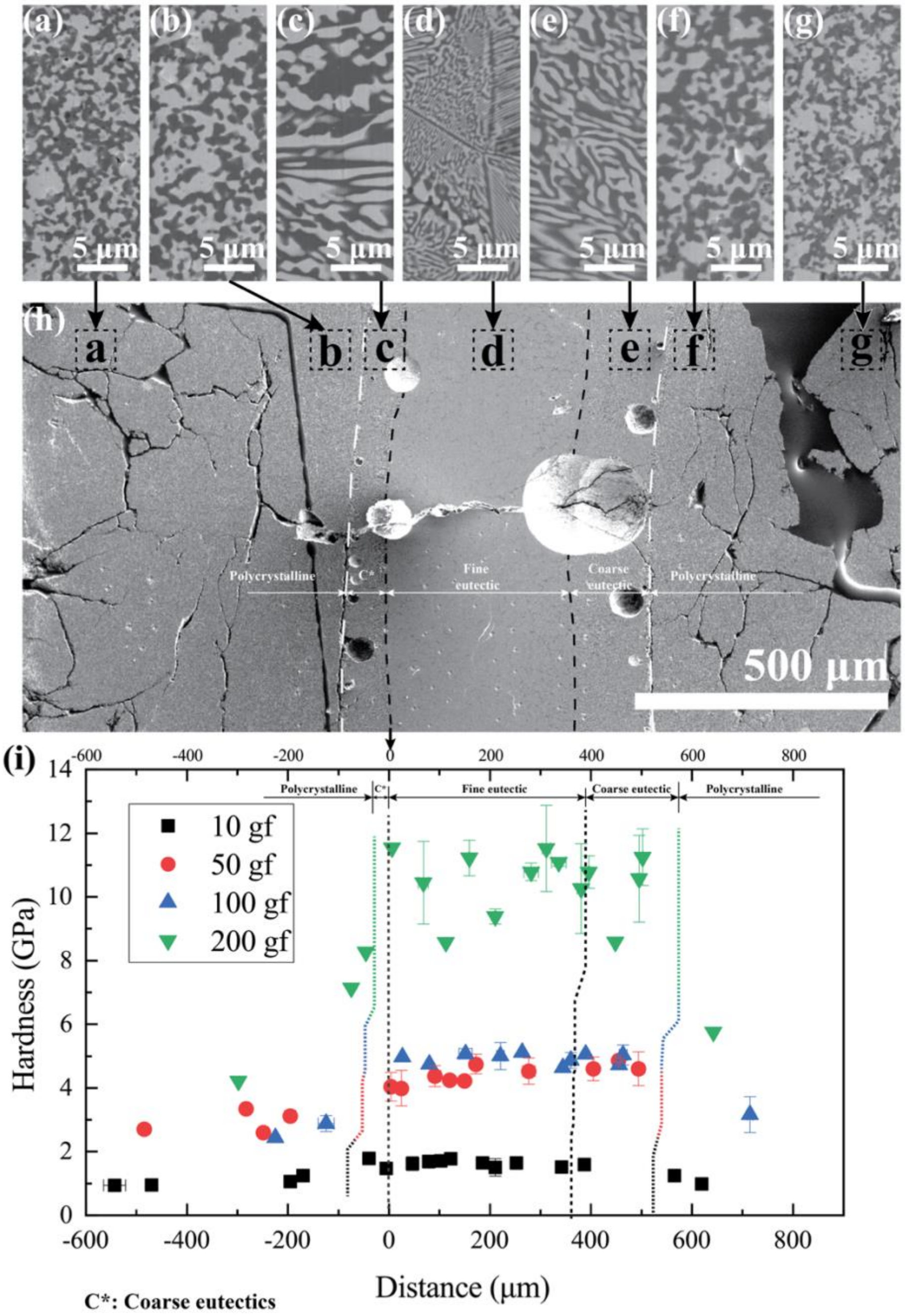

Figure 6.3 (a)-(h) SEM images the polished surface. Images (a)-(g) were taken from different locations across the channeled region, as labeled in (h). From the edge to the center (a)-(d) or (g)-(d), the microstructures observed were polycrystalline grains (with decreasing grain sizes), coarse eutectics, and fine eutectics. (i) shows measured hardness value in relation to the locations of the indent, the microstructure of which are labeled. Boundaries of the microstructures are marked by dotted lines in (h) and (i).

Farther from the center region, polycrystalline microstructure can be observed, as shown in Figure 6.3 (b) and (f). As the microstructure grows farther away from the center region, the grain sizes of the polycrystalline structure decrease, shown by Figure 6.3 (a) and (g). Hardness values measured under the same load in these polycrystalline regions (Figure 6.3 (a), (g) and (b) (f)) were nearly the same despite the grain size change, as shown in Figure 6.3 (i) outside of the colored boundaries.

Comparing the hardness measured from the polycrystalline regions and the eutectic regions, the hardness values obtained from latter were drastically higher than former, almost double in some cases.

It can also be observed that the boundaries between the polycrystalline region and the eutectic microstructure (the white dashed lines) are susceptible to crack propagation, as seen in Figure 6.3 (h).

6.4.3 Reverse indentation size effect

Comparing the hardness values obtained from different indentation loads, a reverse indentation size effect (ISE) can be observed. As presented in Figure 6.4, the hardness values increase as the load increases for the same microstructure. The overall hardness of eutectic microstructures is higher than the polycrystalline structures, and the average measured hardness value measured with 200 gf approaches the upper-bound of the predicted value from the rule of mixtures.

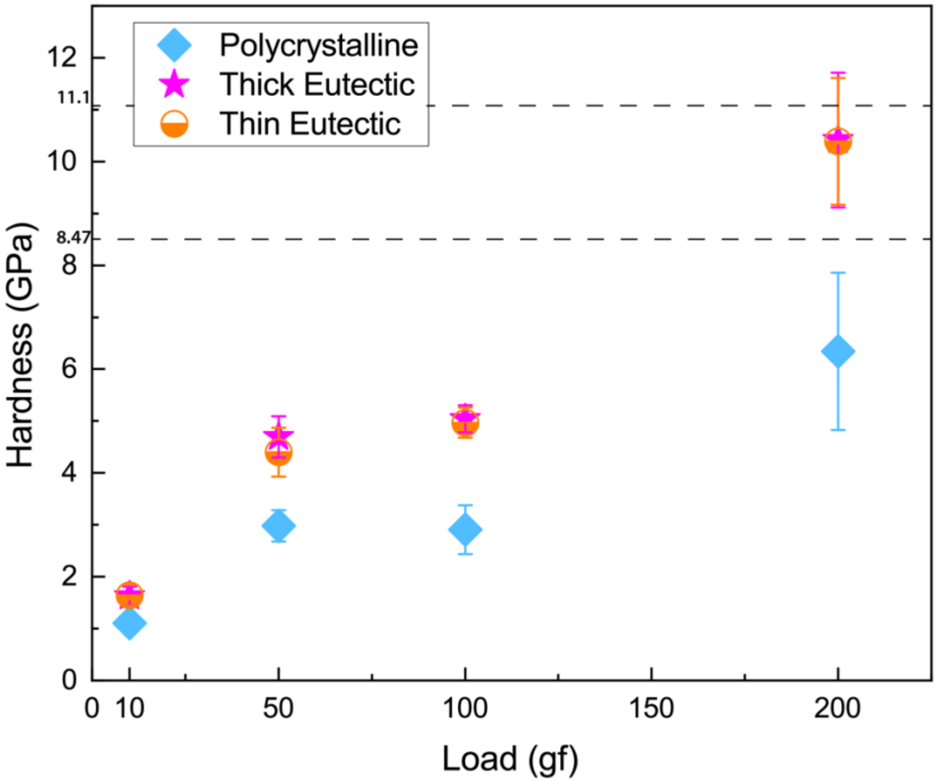

Figure 6.4 Measured Vickers hardness value as a function of the applied load for various microstructures of the composite system.

6.5 Discussions

6.5.1 Challenges of indentation on single phase samples

In this study, attempts were made to indent single phase samples of $LaPO_4$ and Al_2O_3. A large amount of spalling was found on both samples at a low load (25 gf for $LaPO_4$ and 200 gf for Al_2O_3). They were both sintered at above 1500°C for over 5 hours, and cooled in the furnace after sintering. This rules out thermal stress as the cause for spalling. Spalling can also be attributed to fast loading rates of the indenter, but the issue was not resolved even after the indenter was adjusted to 1 mm/minute. Both samples were reported to be only >93% dense, which may indicate that closed porosity play a big role in spalling.

6.5.2 Theoretical models of the reverse ISE behavior

Past literature has reported reverse ISE on other ceramic materials,[139–142] two theoretical models can be applied to describe the behavior: the Indentation-induced cracking (IIC) model and Meyer's law.

The IIC model proposes that ISE effects can be described by the following equation when it is a brittle material:[143]

$$HV = K\left(\frac{P^{5/3}}{D^3}\right) \qquad \text{Equation 6.4}$$

Where HV is the Vickers hardness value, P is the load and D is the mean diameter of the indents. By plotting ln HV against $ln\,(\frac{P^{5/3}}{D^3})$, their relationship can be fitted linearly as shown in Figure 6.5.

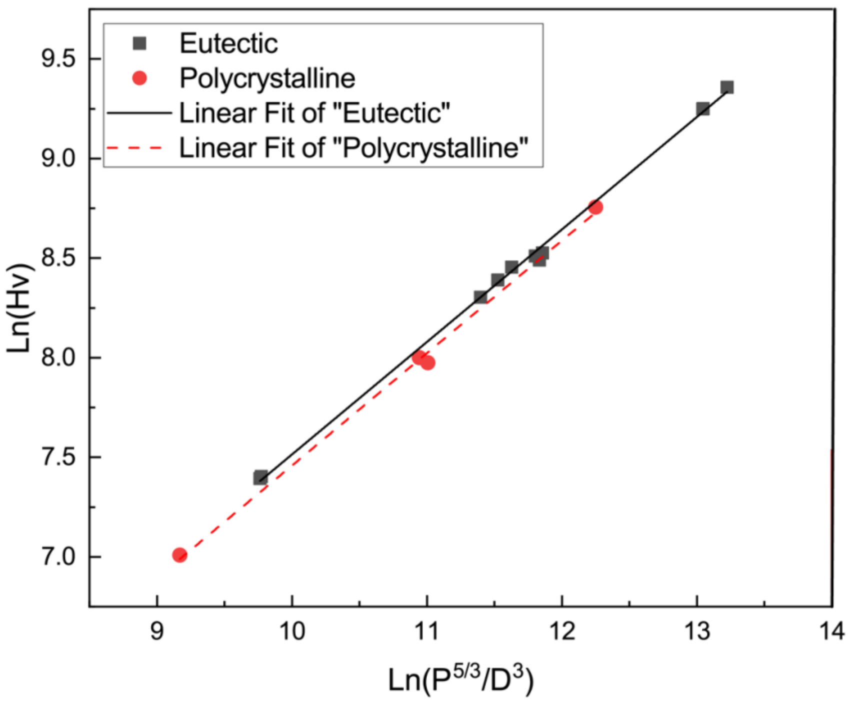

Figure 6.5 Plot of *ln HV* against $ln\ (\frac{P^{5/3}}{D^3})$, linear fit was extracted for data from each microstructure.

The relationship can be empirically expressed as $\ln HV = \ln K + b \cdot \ln\left(\frac{P^{5/3}}{D^3}\right)$, $\ln K$ and b being the extrapolated intercept and slope values, respectively (shown in Figure 6.5). The $\ln K$ and b values calculated from the linear fit for the polycrystalline and eutectic microstructures are shown in Table 6.1.

Table 6.1 value of $\ln\ K$ and b for polycrystalline and eutectic microstructures

	$\ln K$	b
Polycrystalline microstructure	1.808±0.216	0.565±0.0198
Eutectic microstructure	1.865±0.0922	0.565±0.00783

The relationship between HV, P, and D is therefore:

$$HV = K\left(\frac{P^{5/3}}{D^3}\right)^b \qquad \text{Equation 6.5}$$

Comparing Equation 6.4 and Equation 6.5, it can be concluded because b≠1, the parameter K is dependent on the load P, therefore the IIC model cannot be applied to this material system to predict a load-independent hardness value.[140] The authors of the IIC model also attributed reverse ISE to indentation cracking,[143] but cracking has not been prominent or consistent in this study. Conclusions can be made that cracking is not the main reason for the reverse ISE in this system.

The second model used to characterize reverse ISE is Meyer's law.[144] The form of Myer's law can be expressed as:

$$P = AD^n \qquad \text{Equation 6.6}$$ [145]

By plotting $\ln P$ and $\ln d$, values of A and n can be explored. Figure 6.6 shows the scatter plot of $\ln P$ and $\ln dD$ from the different microstructures, which does not show a clear linear trend, however. It has been reported in the past that linear fitting of Meyer's law can be segmented into more than one parts, for example, Sangwal *et al.*[140] discovered that by fitting separately at low loads (P ≤ 50 g) and high loads (P ≥ 50) Meyer's law gives the best-fit plots. However, data from P > 200 g is lacking for this study to decide what the relationship between P and D is at higher loads, and whether it is suitable to fit values from P ≥ 200 g with a separate linear fit.

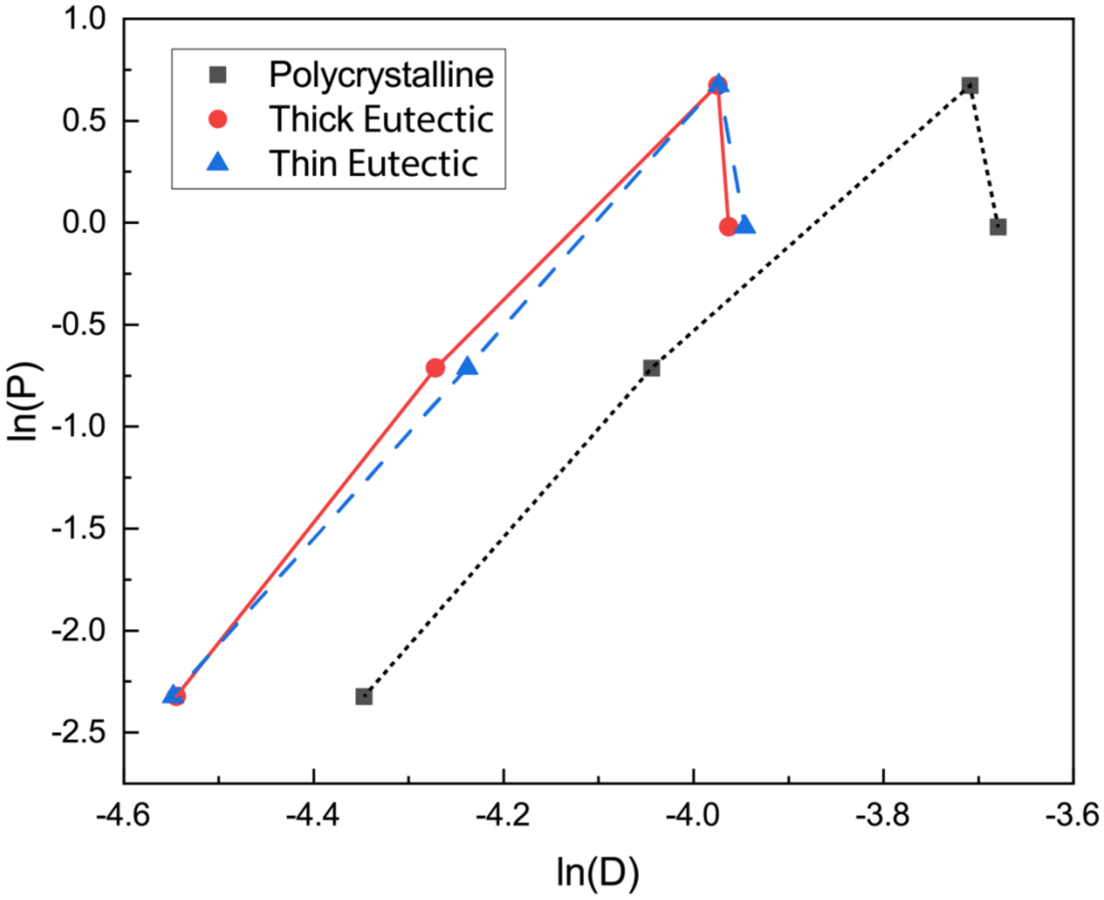

Figure 6.6 ln P plotted with ln D according to Meyer's law.

6.6 Conclusions

- The hardness of eutectic microstructures is superior to that of the polycrystalline structures.
- In this study, the hardness of eutectic microstructures with different layer thickness showed no prominent differences.
- Micro-hardness measurements of the 50-50 vol.% $LaPO_4$-Al_2O_3 system follow the reserve ISE, with lower hardness values at smaller loads.

CHAPTER 7 CONCLUSIONS AND FUTURE WORK

7.1 Conclusions

The effects of flash sintering on composite ceramic materials were investigated in this work. Results from flash sintering $LaPO_4$-8YSZ composites show the catalytic effects of 8YSZ in assisting flash sintering, which echoes with previous experimental work.[31,87,146,147] Single phase $LaPO_4$ first tried to be flash sintered in this work, did not flash on its own, while addition of 8YSZ enabled flash sintering of $LaPO_4$-8YSZ composites. Single phase α-Al_2O_3 did not flash sinter on its own either within limitations of our equipment. $LaPO_4$-Al_2O_3 composites, however, could be flash sintered despite the lack of flash for single phases. This can potentially be attributed to the hetero-interfaces in the composites.

Flash sintering of the $LaPO_4$-Al_2O_3 composites happen through extensive channeling in the material, producing a highly heterogeneous microstructure. Within the channeled region, eutectic microstructures of $LaPO_4$-Al_2O_3 were observed, establishing this system to be eutectic-forming at high temperatures. Local temperatures reached during flash sintering were estimated through calculation.

Various experimental parameters of flash sintering were investigated, including electric field densities, electric current densities and hold times after the flash phenomena, and how they affect the microstructures. With higher electric currents (≥ 5 mA/mm^2 in this study), there are large grains of $LaPO_4$ and hexagonal sapphire crystals produced in the channeled region. The eutectic microstructure appears more regular and ordered as well, compared to materials processed by lower electric current (2 mA/mm^2). With an electric current of 2 mA/mm^2, no grains with abnormal grain growth were observed, and the primary microstructure in the channel region was composed of eutectic microstructures with randomly oriented irregular eutectics.

The crystallinity and symmetry of the Al_2O_3 large sapphire crystals produced by flash sintering were studied. The Al_2O_3 grains were mainly single crystals with strong faceting tendencies, the majority of them appear equiangular, shaped as either equilateral hexagon grains or elongated hexagons. Electron microscopy characterization revealed that the shapes of the large grains are indicative of their orientation and faceting of the Al_2O_3 large grains strongly prefer low-energy planes such as the basal or pyramidal plane. The size of the sapphire crystals can be tailored by adjusting the parameters of flash sintering also.

The mechanical properties of the eutectic microstructures produced by flash sintering were measured. The hardness of eutectic microstructure were almost doubled from the polycrystalline microstructures. For both polycrystalline and eutectic microstructures, the hardness value measured showed strong dependence on the load applied, where reverse indentation size effect was observed.

This study also proposed a constructed phase diagram for this eutectic-forming $LaPO_4$-Al_2O_3 system, with negligible solid solubility, an eutectic temperature between 1880°C and 2037°C, and a eutectic composition close to 50-50 vol% $LaPO_4$-Al_2O_3.

7.2 Future work

Future work is still needed to further the understanding of the flash sintering process in composites and to better determine why two phase systems can more easily flash compared to their individual components.

Synchrotron experiments of the flash sintering process for $LaPO_4$-Al_2O_3 could be used to verify the occurrence of melting in-situ. It could also estimate the local temperatures during flash with the help of a marker material such as platinum, at least up to melting temperature of platinum.

High temperature DSC experiments between 1880°C and 2030°C with a slower scanning rate could help better determine the nature of the endothermic events and more exactly pinpoint the eutectic melting temperature. The eutectic composition of the system could be better simulated if databases with more accurate thermodynamic data for the constituents is available in the future.

Further TEM work on the interfaces between $LaPO_4$-Al_2O_3, could tease out if there are specific orientation relationships and be used to characterize the interfacial energy between the two phases, as well as any grain boundary segregation. The study of interfacial energies of specific crystalline planes and controlled experiments on analyzing the growth rate of the low-energy planes can shed light on the fundamental mechanisms for microstructural development in this system.

To determine the surface termination and surface chemistry of the sapphire crystals, characterization techniques such as atomic scale scanning tunneling microscopy measurements, low-energy electron diffraction, and reflection high-energy electron diffraction could be conducted.

REFERENCES

1. de Faoite D, Browne DJ, Chang-Díaz FR, Stanton KT. A review of the processing, composition, and temperature-dependent mechanical and thermal properties of dielectric technical ceramics. J Mater Sci. 2012;47(10):4211–4235.

2. Shukla P, Robertson S, Wu H, Telang A, Kattoura M, Nath S, et al. Surface engineering alumina armour ceramics with laser shock peening. Mater Des. 2017;134523–538.

3. Ni H, Guo Y, Wang L, Guo Y, Zhan W, Lu G. Facile synthesis of highly thermal-stable doped alumina with high surface area by low temperature solid-state reaction. Powder Technol. 2017;31522–30.

4. Morgan PED, Clarke DR, Jantzen CM, Barker AB. High-Alumina Tailored Nuclear Waste Ceramics. J Am Ceram Soc. 1981;64(5):249–258.

5. Orlova AI, Ojovan MI. Ceramic Mineral Waste-Forms for Nuclear Waste Immobilization. Materials (Basel). 2019;12(16):2638.

6. Stefanovsky S V, Yudintsev S V. Titanates, zirconates, aluminates and ferrites as waste forms for actinide immobilization. Russ Chem Rev. 2016;85(9):962–994.

7. Pandey AK, Biswas K. Effect of hydrothermal treatment on tribological properties of alumina and zirconia based bioceramics. Ceram Int. 2016;42(2):2306–2316.

8. Wang H, Du R, Shi R, Liu J. Novel composite electrolytes of $Zr_{0.92}Y_{0.08}O_{2-\alpha}$(8YSZ)-low melting point glass powder for intermediate temperature solid oxide fuel cells. Materials (Basel).;11(7):.

9. Zou J, Lin Q, Cheng C, Zhang X, Jin Q, Jin H, et al. High-performance limiting current oxygen sensor comprised of highly active $La_{0.75}Sr_{0.25}Cr_{0.5}Mn_{0.5}O_3$ electrode. Sensors (Switzerland).;18(7):.

10. Arinicheva Y, Bosbach DA, Roth G. Monazite-type ceramics as nuclear waste form: crystal structure, microstructure and properties. Forschungszentrum Jülich GmbH, Zentralbibliothek.;

11. Clavier N, Podor R, Dacheux N. Crystal chemistry of the monazite structure. J Eur Ceram Soc. 2011;31(6):941–976.

12. Errandonea D, Gomis O, Rodríguez-Hernández P, Muñoz A, Ruiz-Fuertes J, Gupta M, et al. High-pressure structural and vibrational properties of monazite-type $BiPO_4$, $LaPO_4$, $CePO_4$, and $PrPO_4$. J Phys Condens Matter. 2018;30(6):065401.

13. Ajili L, Ferhi M, Sdiri N, Abassi N, Horchani-Naifer K, Férid M. Proton conductivity in SiO_2-$LaPO_4$ composites. J Alloys Compd. 2019;788604–614.

14. Meldrum A, Boatner LA, Ewing RC. A comparison of radiation effects in crystalline ABO_4-type phosphates and silicates. Mineral Mag. 2000;64(2):185–194.

15. Norby T, Truls N. Solid-state protonic conductors: Principles, properties, progress and prospects. Solid State Ionics. 1999;125(1):1–11.

16. Morgan PED, Marshall DB, Housley RM. High-temperature stability of monazite-alumina composites. Mater Sci Eng A. 1995;195(C):215–222.

17. Guo L, Yan Z, Yu Y, Yang J, Li M. CMAS resistance characteristics of $LaPO_4$/YSZ thermal barrier coatings at 1250°C–1350°C. Corros Sci. 2019;154111–122.

18. Morgan PED, Marshall DB. Ceramic composites of monazite and alumina. J Am Ceram Soc. 1995;78(6):1553–1563.

19. Marshall DB, Morgan PED, Housley RM. Debonding in multilayered composites of zirconia and $LaPO_4$. J Am Ceram Soc. 2005;80(7):1677–1683.

20. Zhang C, Fei J, Guo L, Yu J, Zhang B, Yan Z, et al. Thermal cycling and hot corrosion behavior of a novel $LaPO_4$/YSZ double-ceramic-layer thermal barrier coating. Ceram Int. 2018;44(8):8818–8826.

21. Ren X, Guo S, Zhao M, Pan W. Thermal conductivity and mechanical properties of YSZ/$LaPO_4$ composites. J Mater Sci. 2014;49(5):2243–2251.

22. Min W, Miyahara D, Yokoi K, Yamaguchi T, Daimon K, Hikichi Y, et al. Thermal and mechanical properties of sintered $LaPO_4$-Al_2O_3 composites. Mater Res Bull. 2001;36(5–6):939–945.

23. Min W, Daimon K, Matsubara T, Hikichi Y. Thermal and mechanical properties of sintered machinable $LaPO_4$–ZrO_2 composites. Mater Res Bull. 2002;37(6):1107–1115.

24. Men D, Mecartney ML. Superplasticity and machinability in a four-phase ceramic. Mater Res Bull. 2012;47(8):1925–1931.

25. Hay R., Boakye E, Petry M. Effect of coating deposition temperature on monazite coated fiber. J Eur Ceram Soc. 2000;20(5):589–597.

26. Kuo D-H, Kriven WM. Chemical stability, microstructure and mechanical behavior of $LaPO_4$-containing ceramics. Mater Sci Eng A. 1996;210(1–2):123–134.

27. Badolia A, Sarkar R, Pal SK. Reactive alumina–$LaPO_4$ composite as machinable bioceramics. Bull Mater Sci. 2015;38(4):975–983.

28. Sujith SS, Arun Kumar SL, Mahesh K V., Peer Mohamed A, Ananthakumar S. Sintering and Thermal Shock Resistance Properties of LaPO4Based Composite Refractories. Trans Indian Ceram Soc. 2014;73(2):161–164.

29. Badolia A, Sarkar R, Pal SK. Lanthanum Phosphate Containing Machinable Alumina Ceramics for Bio-Medical Applications. Trans Indian Ceram Soc. 2014;73(2):115–120.

30. Zhang C, Fei J, Guo L, Yu J, Zhang B, Yan Z, et al. Thermal cycling and hot corrosion behavior of a novel LaPO4/YSZ double-ceramic-layer thermal barrier coating. Ceram Int. 2018;44(8):8818–8826.

31. Dychtoń K, Drajewicz M, Pytel M, Rokicki P, Nowotnik A. Yttria-stabilized zirconia–alumina composite sintering temperature effect on thermal diffusivity. J Therm Anal Calorim. 2016;126(1):1–7.

32. Raj R, Cologna M, Francis JSC. Influence of externally imposed and internally generated electrical fields on grain growth, diffusional creep, sintering and related phenomena in ceramics. J Am Ceram Soc. 2011;94(7):1941–1965.

33. Marshall D. Ceramics for future power generation technology: fiber reinforced oxide composites. Curr Opin Solid State Mater Sci. 2001;5(4):283–289.

34. Sudre OH, Marshall DB, Morgan PED. Monazite-based thermal barrier coatings. Washington, DC, United States patent US6863999. March 8, 2005.

35. Rajeswari K, Hareesh US, Subasri R, Chakravarty D, Johnson R. Comparative evaluation of spark plasma (SPS), microwave (MWS),two stage sintering (TSS) and conventional sintering (CRH) on the densification and micro structural evolution of fully stabilized zirconia ceramics. Sci Sinter. 2010;42(3):259–267.

36. Laberty-Robert C, Ansart F, Deloget C, Gaudon M, Rousset A. Dense yttria stabilized zirconia: sintering and microstructure. Ceram Int. 2003;29(2):151–158.

37. Wang C-J, Huang C-Y, Wu Y-C. Two-step sintering of fine alumina–zirconia ceramics. Ceram Int. 2009;35(4):1467–1472.

38. Sujith SS, Arun Kumar SL, Mangalaraja RV, Peer Mohamed A, Ananthakumar S. Porous to dense LaPO4 sintered ceramics for advanced refractories. Ceram Int. 2014;40(9):15121–15129.

39. Agrafiotis C, Tsoutsos T. Energy saving technologies in the European ceramic sector: a systematic review. Appl Therm Eng. 2001;21(12):1231–1249.

40. Nagano S, Watari K. Energy Assessment of Ceramic Fabrication Processes. J Ceram Soc Japan. 2005;113(1314):179–184.

41. Tikul N, Srichandr P. Assessing the environmental impact of ceramic tile production in Thailand. J Ceram Soc Japan. 2010;118(1382):887–894.

42. Pan MJ, Randall C. A brief introduction to ceramic capacitors. IEEE Electr Insul Mag. 2010;26(3):44–50.

43. Ohtaki KK, Heravi NJ, Leadbetter JW, Morgan PED, Mecartney ML. Extended solubility of Sr in $LaPO_4$ monazite. Solid State Ionics. 2016;293(3):44–50.

44. Cologna M, Rashkova B, Raj R. Flash sintering of nanograin zirconia in <5 s at 850°C. J Am Ceram Soc. 2010;93(11):3556–3559.

45. Charalambous H, Jha SK, Lay RT, Cabales A, Okasinski J, Tsakalakos T. Investigation of temperature approximation methods during flash sintering of ZnO. Ceram Int. 2018;44(6):6162–6169.

46. Yu M, Grasso S, Mckinnon R, Saunders T, Reece MJ. Review of flash sintering: materials, mechanisms and modelling. Adv Appl Ceram. 2017;116(1):24–60.

47. Hao X, Liu Y, Wang Z, Qiao J, Sun K. A novel sintering method to obtain fully dense gadolinia doped ceria by applying a direct current. J Power Sources. 2012;21086–91.

48. Muccillo R, Muccillo ENS. Electric field-assisted flash sintering of tin dioxide. J Eur Ceram Soc. 2014;34(4):915–923.

49. Zapata-Solvas E, Bonilla S, Wilshaw PR, Todd RI. Preliminary investigation of flash sintering of SiC. J Eur Ceram Soc. 2013;33(13–14):2811–2816.

50. Jha SK, Raj R. The effect of electric field on sintering and electrical conductivity of Titania. J Am Ceram Soc. 2014;97(2):527–534.

51. Cologna M, Francis JSC, Raj R. Field assisted and flash sintering of alumina and its relationship to conductivity and MgO-doping. J Eur Ceram Soc. 2011;31(15):2827–2837.

52. Biesuz M, Sglavo VM. Liquid phase flash sintering in magnesia silicate glass-containing alumina. J Eur Ceram Soc. 2017;37(2):705–713.

53. Todd RI. Flash Sintering of Ceramics: A Short Review. In: Lee B, Gadow R, Mitic V, editors. Proceedings of the IV Advanced Ceramics and Applications Conference. Paris: Atlantis Press; 2017. p1–12.

54. Zhang Y, Nie J, Luo J. Effects of phase and doping on flash sintering of TiO_2. J Ceram Soc Japan. 2016;124(4):296–300.

55. M'Peko J-C, Francis JSC, Raj R. Field-assisted sintering of undoped $BaTiO_3$: Microstructure evolution and dielectric permittivity. J Eur Ceram Soc. 2014;34(15):3655–3660.

56. Kok D, Yadav D, Sortino E, McCormack SJ, Tseng K-P, Kriven WM, et al. α-Alumina and spinel react into single-phase high-alumina spinel in <3 seconds during flash sintering. J Am Ceram Soc. 2018;102(2):644–653.

57. Liu D, Gao Y, Liu J, Liu F, Li K, Su H, et al. Preparation of Al_2O_3–$Y_3Al_5O_{12}$–ZrO_2 eutectic ceramic by flash sintering. Scr Mater. 2016;114108–111.

58. Naik KS, Sglavo VM, Raj R. Flash sintering as a nucleation phenomenon and a model thereof. J Eur Ceram Soc. 2014;34(15):4063–4067.

59. Downs J a. Mechanisms of flash sintering in cubic zirconia. University of Trento; 2013.

60. Todd RI, Zapata-Solvas E, Bonilla RS, Sneddon T, Wilshaw PR. Electrical characteristics of flash sintering: thermal runaway of Joule heating. J Eur Ceram Soc. 2015;35(6):1865–1877.

61. Raj R. Joule heating during flash-sintering. J Eur Ceram Soc. 2012;32(10):2293–

2301.

62. Groza JR, Zavaliangos A. Sintering activation by external electrical field. Mater Sci Eng A. 2000;287(2):171–177.

63. Muccillo R, Muccillo ENS. Shrinkage control of yttria-stabilized zirconia during ac electric field-assisted sintering. J Eur Ceram Soc. 2014;34(15):3871–3877.

64. Muccillo R, Muccillo ENS, Kleitz M. Densification and enhancement of the grain boundary conductivity of gadolinium-doped barium cerate by ultra fast flash grain welding. J Eur Ceram Soc. 2012;32(10):2311–2316.

65. Grasso S, Saunders T, Porwal H, Cedillos-Barraza O, Jayaseelan DD, Lee WE, et al. Flash spark plasma sintering (FSPS) of pure ZrB2. J Am Ceram Soc. 2014;97(8):2405–2408.

66. Biesuz M, Sglavo VM. Flash sintering of alumina: Effect of different operating conditions on densification. J Eur Ceram Soc. 2016;36(10):2535–2542.

67. Saunders T, Grasso S, Reece MJ. Ultrafast-Contactless Flash Sintering using Plasma Electrodes. Sci Rep. 2016;6(May):1–6.

68. Naik KS, Sglavo VM, Raj R. Field assisted sintering of ceramic constituted by alumina and yttria stabilized zirconia. J Eur Ceram Soc. 2014;34(10):2435–2442.

69. Zhang Y, Nie J, Chan JM, Luo J. Probing the densification mechanisms during flash sintering of ZnO. Acta Mater. 2017;125465–475.

70. Serrazina R, Vilarinho PM, Senos AMOR, Pereira L, Reaney IM, Dean JS. Modelling the particle contact influence on the Joule heating and temperature distribution

during FLASH sintering. J Eur Ceram Soc. 2020;40(4):1205–1211.

71. Chaim R, Estournès C. On thermal runaway and local endothermic/exothermic reactions during flash sintering of ceramic nanoparticles. J Mater Sci. 2018;53(9):6378–6389.

72. Chaim R. Liquid film capillary mechanism for densification of ceramic powders during flash sintering. Materials (Basel). 2016;9(4):19–21.

73. Chaim R, Chevallier G, Weibel A, Estournès C. Grain growth during spark plasma and flash sintering of ceramic nanoparticles: a review. J Mater Sci. 2018;53(5):3087–3105.

74. Dong Y, Chen IW. Predicting the Onset of Flash Sintering. J Am Ceram Soc. 2015;98(8):2333–2335.

75. Dong Y, Chen I -We. Onset Criterion for Flash Sintering. J Am Ceram Soc. 2015;98(12):3624–3627.

76. Cologna M, Francis JSC, Raj R. Field assisted and flash sintering of alumina and its relationship to conductivity and MgO-doping. J Eur Ceram Soc. 2011;31(15):2827–2837.

77. Terauds K, Lebrun JM, Lee HH, Jeon TY, Lee SH, Je JH, et al. Electroluminescence and the measurement of temperature during Stage III of flash sintering experiments. J Eur Ceram Soc. 2015;35(11):3195–3199.

78. Yang D, Raj R, Conrad H. Enhanced sintering rate of zirconia (3Y-TZP) through the effect of a weak dc electric field on grain growth. J Am Ceram Soc.

2010;93(10):2935–2937.

79. Jha SK, Charalambous H, Wang H, Phuah XL, Mead C, Okasinski J, et al. In-situ observation of oxygen mobility and abnormal lattice expansion in ceria during flash sintering. Ceram Int. 2018;44(13):15362–15369.

80. Wellons M. The Stefan-Boltzmann Law. Phys Dep Coll Wooster, Wooster, Ohio.;44691.

81. Rigaku. Automated multipurpose X-ray diffractometer (XRD) with Guidance software. . https://www.rigaku.com/en/products/xrd/smartlab (accessed August 30, 2019).

82. IMRI facilities. . https://www.imri.uci.edu/content/imri-facilities (accessed August 30, 2019).

83. Nolze G. Euler angles and crystal symmetry. Cryst Res Technol. 2015;50(2):188–201.

84. Oxford Instruments. Microstructure Visualization in SEM. . http://www.ebsd.com/solving-problems-with-ebsd/microstructure-visualization-in-sem (2016, accessed August 30, 2019).

85. Tikul N, Srichandr P. Assessing the environmental impact of ceramic tile production in Thailand. J Ceram Soc Japan. 2010;118(1382):887–894.

86. Raj R, Cologna M, Prette ALG, Sglavo VM, Luiz A, Prette G, et al. Methods of flash sintering. United States patent US008940220. 2015.

87. Kok D, Jha SK, Raj R, Mecartney ML. Flash sintering of a three-phase alumina,

spinel, and yttria-stabilized zirconia composite. J Am Ceram Soc. 2017;100(7):3262–3268.

88. Bichaud E, Chaix JM, Carry C, Kleitz M, Steil MC. Flash sintering incubation in Al_2O_3/TZP composites. J Eur Ceram Soc. 2015;35(9):2587–2592.

89. Yoon B, Avila V, Kathiria R, Jesus LM. Effects of powder dispersion on reactive flash sintering of 8 mol% yttria-stabilized zirconia and $MgAl_2O_4$ composites. Scr Mater. 2020;189117–121.

90. Naik K, Jha SK, Raj R. Correlations between conductivity, electroluminescence and flash sintering. Scr Mater. 2016;1181–4.

91. Liu D, Gao Y, Liu J, Li K, Liu F, Wang Y, et al. SiC whisker reinforced ZrO_2 composites prepared by flash-sintering. J Eur Ceram Soc. 2016;36(8):2051–2055.

92. Gaur A, Sglavo VM. Flash sintering of (La, Sr)(Co, Fe)O_3-Gd-Doped CeO_2 composite. J Am Ceram Soc. 2015;98(6):1747–1752.

93. Francis JSC, Cologna M, Montinaro D, Raj R. Flash sintering of anode-electrolyte multilayers for SOFC applications. J Am Ceram Soc. 2013;96(5):1352–1354.

94. Liu J, Xu X, Liu D, Chen L, Zhao K, An L. Ultrafast formation of Al_2O_3 –$Y_3Al_5O_{12}$ eutectic ceramic by flash sintering. J Am Ceram Soc. 2020;103(8):4051–4056.

95. Davis JB, Marshall DB, Morgan PED. Oxide composites of Al_2O_3 and $LaPO_4$. J Eur Ceram Soc. 1999;19(13–14):2421–2426.

96. Croker MN, Baragar D, Smith RW. Anomalous eutectic growth. J Cryst Growth. 1975;30(2):198–212.

97. Stubican VS, Bradt RC. Eutectic solidification in ceramic systems. Annu Rev Mater Sci. 1981;11(1):267–297.

98. Dong Y, Chen I. Onset Criterion for Flash Sintering. J Am Ceram Soc. 2015;98(12):3624–3627.

99. Zapata-Solvas E, Bonilla S, Wilshaw PR, Todd RI. Preliminary investigation of flash sintering of SiC. J Eur Ceram Soc. 2013;33(13–14):2811–2816.

100. Francis JSC, Raj R. Influence of the field and the current limit on flash sintering at isothermal furnace temperatures. J Am Ceram Soc. 2013;96(9):2754–2758.

101. Jha SK, Lebrun JM, Raj R. Phase transformation in the alumina–titania system during flash sintering experiments. J Eur Ceram Soc. 2016;36(3):733–739.

102. Mosley Frederick H. Experimental determination of emissivity and resistivity of yttria stabilized zirconia at high temperatures. The University of Tennessee, Knoxville; 2008.

103. Tanaka H, Sawai S, Morimoto K, Hisano K. Measurement of spectral emissivity and thermal conductivity of zirconia by thermal radiation calorimetry. J Therm Anal Calorim. 2001;64(3):867–872.

104. Touloukian YS, Dewitt DP. Thermophysical properties of matter - The TPRC Data Series. Volume 8. Thermal radiative properties - nonmetallic solids. 1972.

105. Geller RF, Yavorsky PJ. Melting point of alpha-alumina. J Res Natl Bur Stand (1934). 1945;34(4):395.

106. Hikichi Y, Nomura T. Melting temperatures of monazite and xenotime. J Am Ceram

Soc. 1987;70(10):C-252-C–253.

107. Chaim R. Particle Surface Softening as Universal Behaviour during Flash Sintering of Oxide Nano-Powders. Materials (Basel). 2017;10(2):179.

108. Chaim R, Amouyal Y. Liquid-film assisted mechanism of reactive fash sintering in oxide systems. Materials (Basel). 2019;12(9):1494.

109. Wang J, Xu F, Wheatley RJ, Neate N, Hou X. Yb^{3+} doping effects on thermal conductivity and thermal expansion of yttrium aluminium garnet. Ceram Int. 2016;42(12):14228–14235.

110. Marshall DB, Morgan PED, Housley RM, Cheung JT. High-temperature stability of the Al_2O_3-$LaPO_4$ system. J Am Ceram Soc. 2005;81(4):951–956.

111. Morrissey KJ, Carter CB. Faceted grain boundaries in Al_2O_3. J Am Ceram Soc. 2006;67(4):292–301.

112. Arnold H, Aroyo MI, Bertaut EF, Burzlaff H, Chapuis G. Space-group symmetry. In: Hahn T, Aroyo MI, editors. International Tables for Crystallography. Chester, England: International Union of Crystallography; p.

113. Wang Z-G, Ouyang J-H, Ma Y-H, Wang Y-J, Xie L-Y, Henniche A, et al. Enhanced nucleation undercooling and surface self-nanocrystallization of Al_2O_3-ZrO_2(Y_2O_3) eutectic ceramics. J Eur Ceram Soc. 2019;39(4):1707–1711.

114. Han XJ, Wang N, Wei B. Rapid eutectic growth under containerless condition. Appl Phys Lett. 2002;81(4):778–780.

115. Peña JI, Larsson M, Merino RI, Francisco I de, Orera VM, LLorca J, et al. Processing,

microstructure and mechanical properties of directionally-solidified Al_2O_3–$Y_3Al_5O_{12}$–ZrO_2 ternary eutectics. J Eur Ceram Soc. 2006;26(15):3113–3121.

116. Kim WY, Tanaka H, Kasama A, Hanada S. Microstructure and room temperature fracture toughness of Nb_{ss}/Nb_5Si_3 in situ composites. Intermetallics. 2001;9(9):827–834.

117. An L, Wu S, Chan HM, Harmer MP, Brandon DG. Alumina platelet reinforced reaction bonded aluminum oxide composites: Textured and random. J Mater Res. 1997;12(12):3300–3306.

118. Paek Y-K, Suvaci E, Messing GL. Preparation and Fracture Behavior of Alumina Platelet Reinforced Alumina-Monazite Composites. Mater Trans. 2002;43(12):3262–3265.

119. Seabaugh MM, Kerscht IH, Messing GL. Texture development by templated grain growth in liquid-phase-sintered α-alumina. J Am Ceram Soc. 1997;80(5):1181–1188.

120. Suvaci E, Messing GL. Critical factors in the Templated Grain Growth of textured reaction-bonded alumina. J Am Ceram Soc. 2000;83(8):2041–2048.

121. Suvaci E, Seabaugh MM, Messing GL. Reaction-based Processing of Textured Alumina by Templated Grain Growth. J Eur Ceram Soc. 1999;19(13–14):2465–2474.

122. Dillon SJ, Miller H, Harmer MP, Rohrer GS. Grain boundary plane distributions in aluminas evolving by normal and abnormal grain growth and displaying different

complexions. Int J Mater Res. 2010;101(1):50–56.

123. Billik P, Čaplovičová M, Čaplovič L, Horváth B. Mechanochemical-molten salt synthesis of α-Al<inf>2</inf>O<inf>3</inf> platelets. Ceram Int. 2015;41(7):8742–8747.

124. Song H, Coble RL. Origin and Growth Kinetics of Platelike Abnormal Grains in Liquid-Phase-Sintered Alumina. J Am Ceram Soc. 1990;73(7):2077–2085.

125. Kebbede A, Messing GL, Carim AH. Grain boundaries in titania-doped α-alumina with anisotropic microstructure. J Am Ceram Soc. 1997;80(11):2814–2820.

126. Kaysser WA, Sprissler M, Handwerker CA, Blendell JE. Effect of a Liquid Phase on the Morphology of Grain Growth in Alumina. J Am Ceram Soc. 1987;70(5):339–343.

127. Godin TJ, Lafemina JP. Atomic and electronic structure of the corundum (α-alumina) (0001) surface. Phys Rev B. 1994;49(11):7691–7696.

128. Fabrichnaya O, Zinkevich M, Aldinger F. Thermodynamic assessment of the systems La_2O_3 –Al_2O_3 and La_2O_3 –$Y2O_3$. Int J Mater Res. 2006;97(11):1495–1501.

129. Liu ZR, Shao YH, Yin CM, Kong YH. Measurement of the eutectic composition and temperature of energetic materials. Part 1. The phase diagram of binary systems. Thermochim Acta. 1995;250(1):65–76.

130. Lakiza S, Fabrichnaya O, Wang C, Zinkevich M, Aldinger F. Phase diagram of the ZrO_2–Gd_2O_3–Al_2O_3 system. J Eur Ceram Soc. 2006;26(3):233–246.

131. Lakiza SM, Lopato LM. Stable and Metastable Phase Relations in the System

Alumina-Zirconia-Yttria. J Am Ceram Soc. 2005;80(4):893–902.

132. Grundy AN, Hallstedt B, Gauckler LJ. Thermodynamic assessment of the lanthanum-oxygen system. J Phase Equilibria. 2001;22(2):105–113.

133. Park HD, Kreidler ER. Phase Equilibria in the System La2O3-P2O5. J Am Ceram Soc. 2006;67(1):23–26.

134. Instrumentation S. SetSys Evolution. .

135. Su H, Ren Q, Zhang J, Wei K, Yao B, Ma W, et al. Microstructures and mechanical properties of directionally solidified $Al_2O_3/GdAlO_3$ eutectic ceramic by laser floating zone melting with high temperature gradient. J Eur Ceram Soc. 2017;37(4):1617–1626.

136. Yu W, Zheng Y, Yu Y, Lin F, Su X, Yang P. The reaction mechanism analysis and mechanical properties of large-size Al2O3/ZrO2 eutectic ceramics prepared by a novel combustion synthesis. Ceram Int. 2018;44(11):12987–12995.

137. Marshall DB, Davis JB, Morgan PED, Waldrop JR, Porter JR. Properties of La-monazite as an interphase in oxide composites. Zeitschrift für Met (Materials Res Adv Tech. 1999;90(12):1048–1052.

138. ASTM Standard. Standard Test Method for Microindentation Hardness of Materials. *ASTM International* 2017;E3841–40.

139. Ozturk O, Arebat RAM, Nefrow ARA, Bulut F, Guducu G, Asikuzun E, et al. Investigation of structural, superconducting and mechanical properties of Co/Cu substituted YBCO-358 ceramic composites. J Mater Sci Mater Electron.

2019;30(8):7400–7409.

140. Sangwal K, Surowska B. Study of indentation size effect and microhardness of SrLaAlO 4 and SrLaGaO 4 single crystals. Mater Res Innov. 2003;7(2):91–104.

141. Dogruer M, Karaboga F, Yildirim G, Terzioglu C. Comparative study on indentation size effect, indentation cracks and superconducting properties of undoped and MgB2 doped Bi-2223 ceramics. J Mater Sci Mater Electron. 2013;24(7):2327–2338.

142. Wang L, Asempah I, Li X, Zang SQ, Zhou YF, Ding J, et al. Indentation size effect in aqueous electrophoretic deposition zirconia dental ceramic. J Mater Res. 2019;34(4):555–562.

143. Li H, Bradt RC. The effect of indentation-induced cracking on the apparent microhardness. J Mater Sci. 1996;31(4):1065–1070.

144. Bull SJ, Page TF, Yoffe EH. An explanation of the indentation size effect in ceramics. Philos Mag Lett. 1989;59(6):281–288.

145. Li H, Bradt RC. The microhardness indentation load/size effect in rutile and cassiterite single crystals. J Mater Sci. 1993;28(4):917–926.

146. Biesuz M, Ometto A, Sglavo VM. Flash Sintering of YSZ/Al2O3 Composites: Effect of Processing and Testing Conditions. Materials (Basel). 2021;14(4):1031.

147. Cologna M, Prette ALG, Raj R. Flash-Sintering of Cubic Yttria-Stabilized Zirconia at 750°C for Possible Use in SOFC Manufacturing. J Am Ceram Soc. 2011;94(2):316–319.

APPENDIX A ADDITIONAL MICROSTRUCTURES PRODUCED BY FLASH SINTERING

Micrographs from microstructures produced by flash sintering

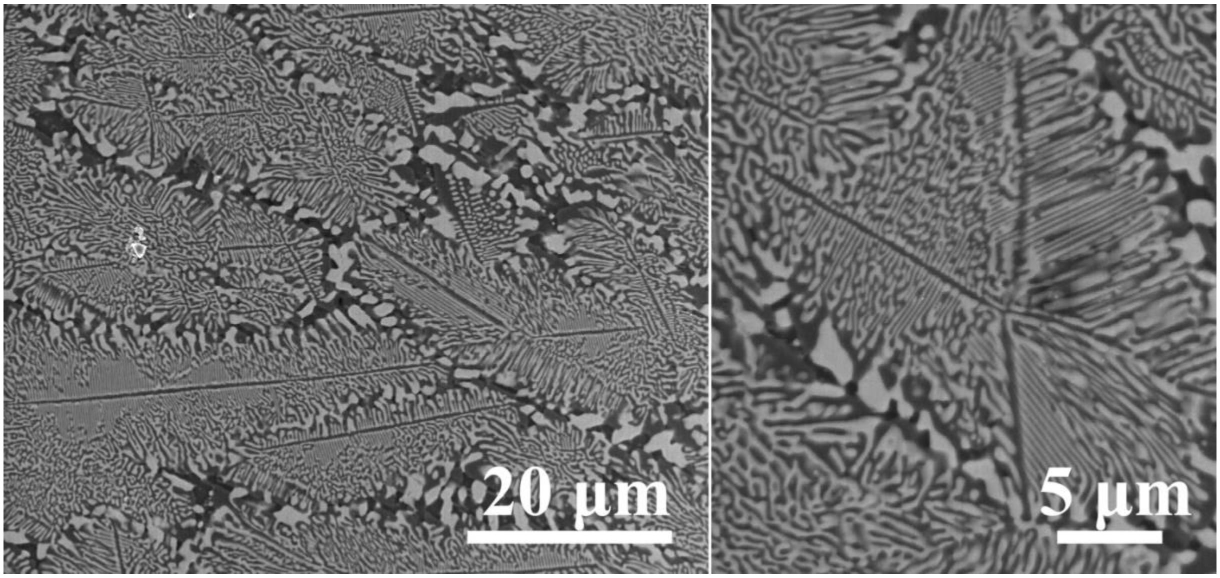

Figure A.1 Thin eutectic microstructure observed by SEM in a 50-50% Al_2O_3-$LaPO_4$ sample flash sintered at 1450°C, 1100V, 25mA/mm^2, held for 10 s. The sample surface is polished so that grains with abnormal grain growth are ground and eutectic microstructures are exposed.

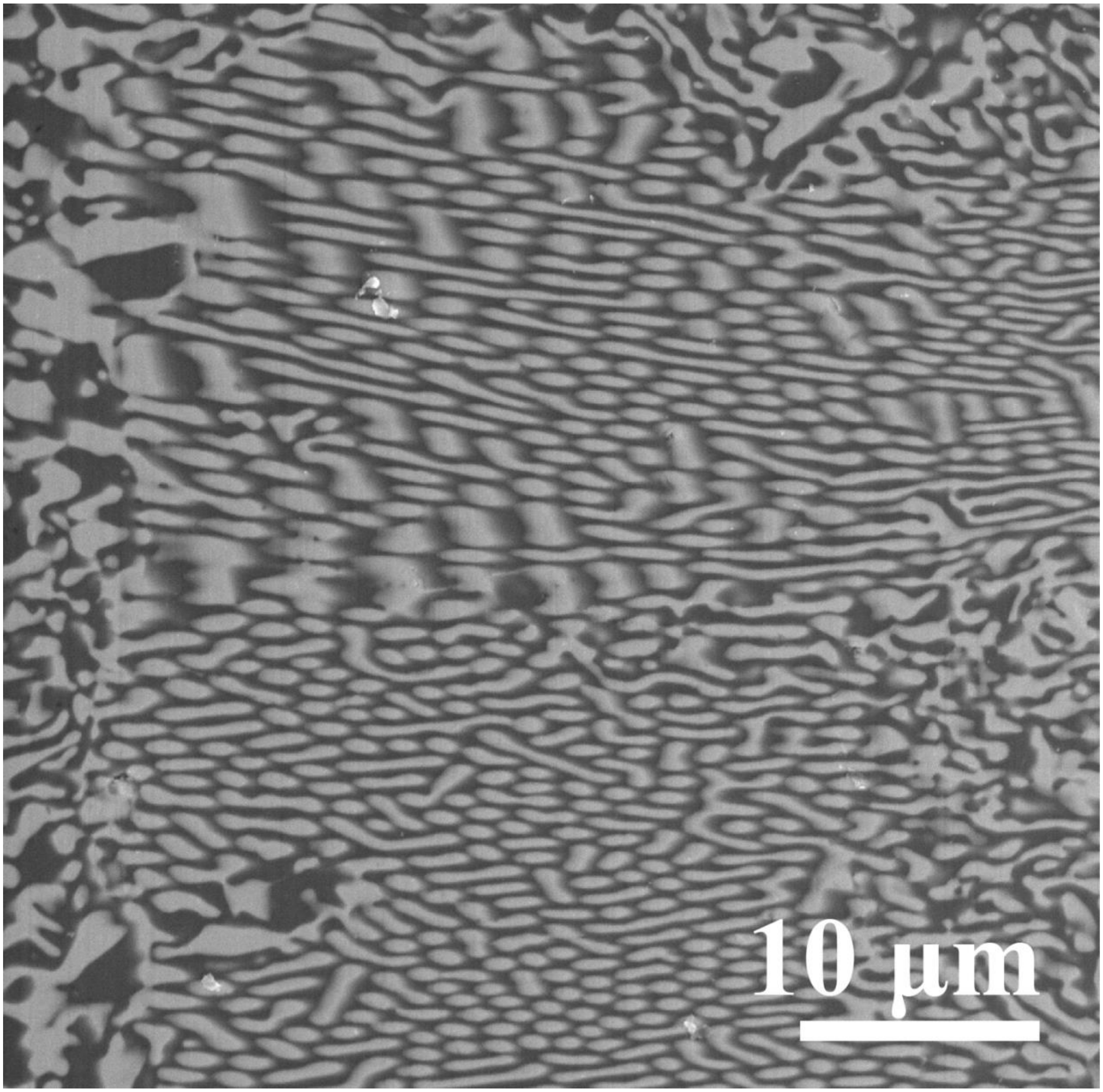

Figure A.2 Eutectic microstructure observed by SEM in a 50-50% Al_2O_3-$LaPO_4$ sample flash sintered at 1450°C, 1100V, 25mA/mm^2, held for 10 s. The sample surface is polished so that grains with abnormal grain growth are ground and eutectic microstructures are exposed. The area observed is close to the edge of the channeling.

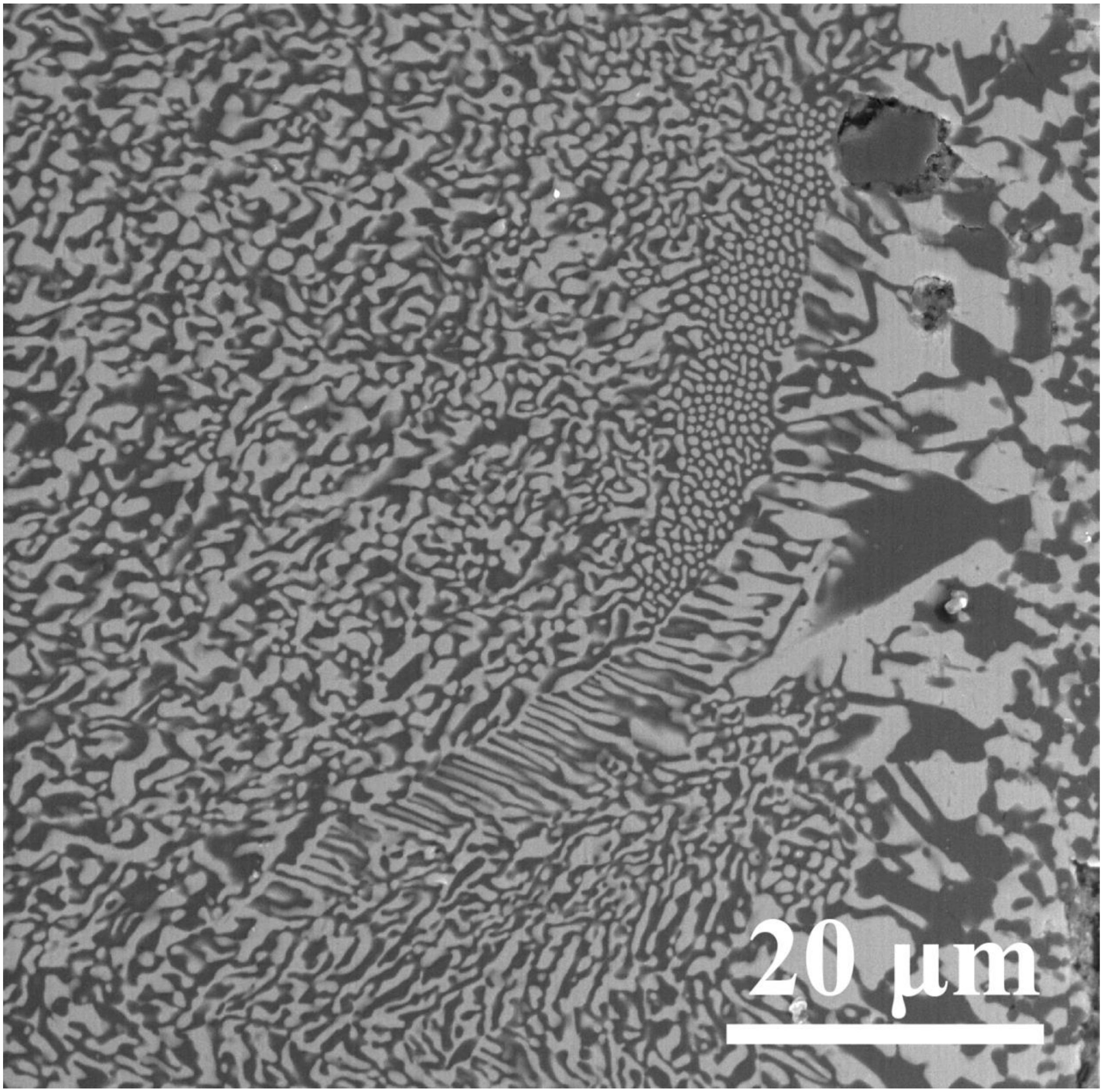

Figure A.3 Eutectic microstructure observed by SEM in a 50-50% Al_2O_3-$LaPO_4$ sample flash sintered at 1450°C, 1100V, 25mA/mm^2, held for 10 s. The sample surface is polished so that grains with abnormal grain growth are ground and eutectic microstructures are exposed. The area observed is the edge of the channeling, polycrystalline microstructure can be observed on the right.

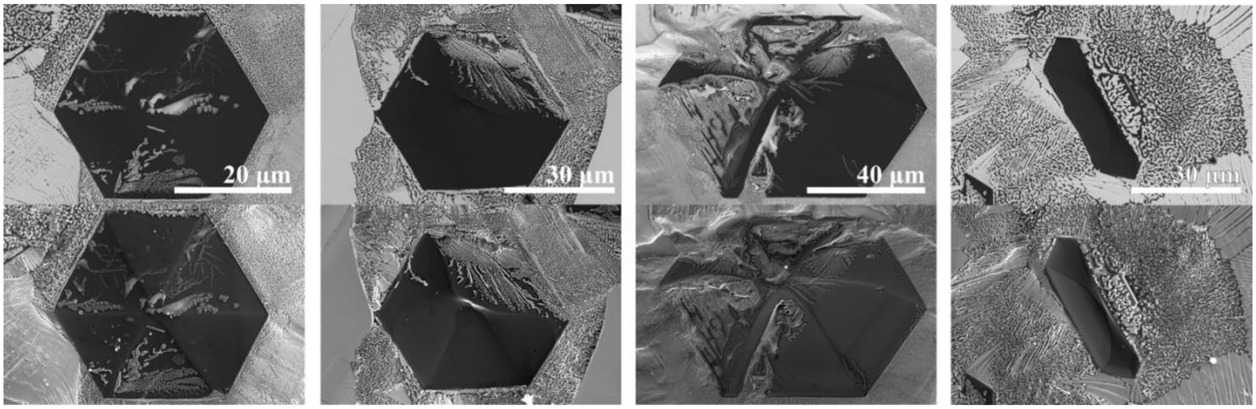

Figure A.4 Various sapphire crystals observed in a 50-50% Al_2O_3-$LaPO_4$ sample flash sintered at 1450°C, 950V, 25mA/mm^2, held for 5.5 s. Top row images were BSE images and bottom row were the same view with SEM images. Areas with darker contrast are Al_2O_3 and brighter contrast are $LaPO_4$.

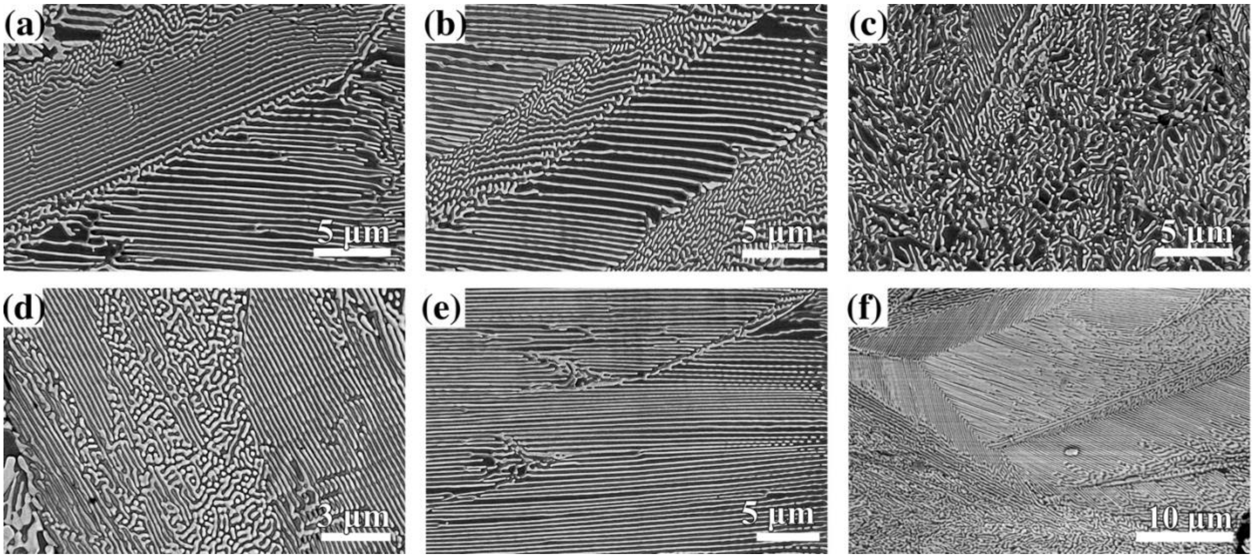

Figure A.5 Eutectic microstructures observed with BSE imaging in the channeled region of 50-50% Al_2O_3-$LaPO_4$ samples flash sintered at 1450°C, 1100V, 25mA/mm^2, (a)-(e) held for 7.5 s, (f) held for 12 s .

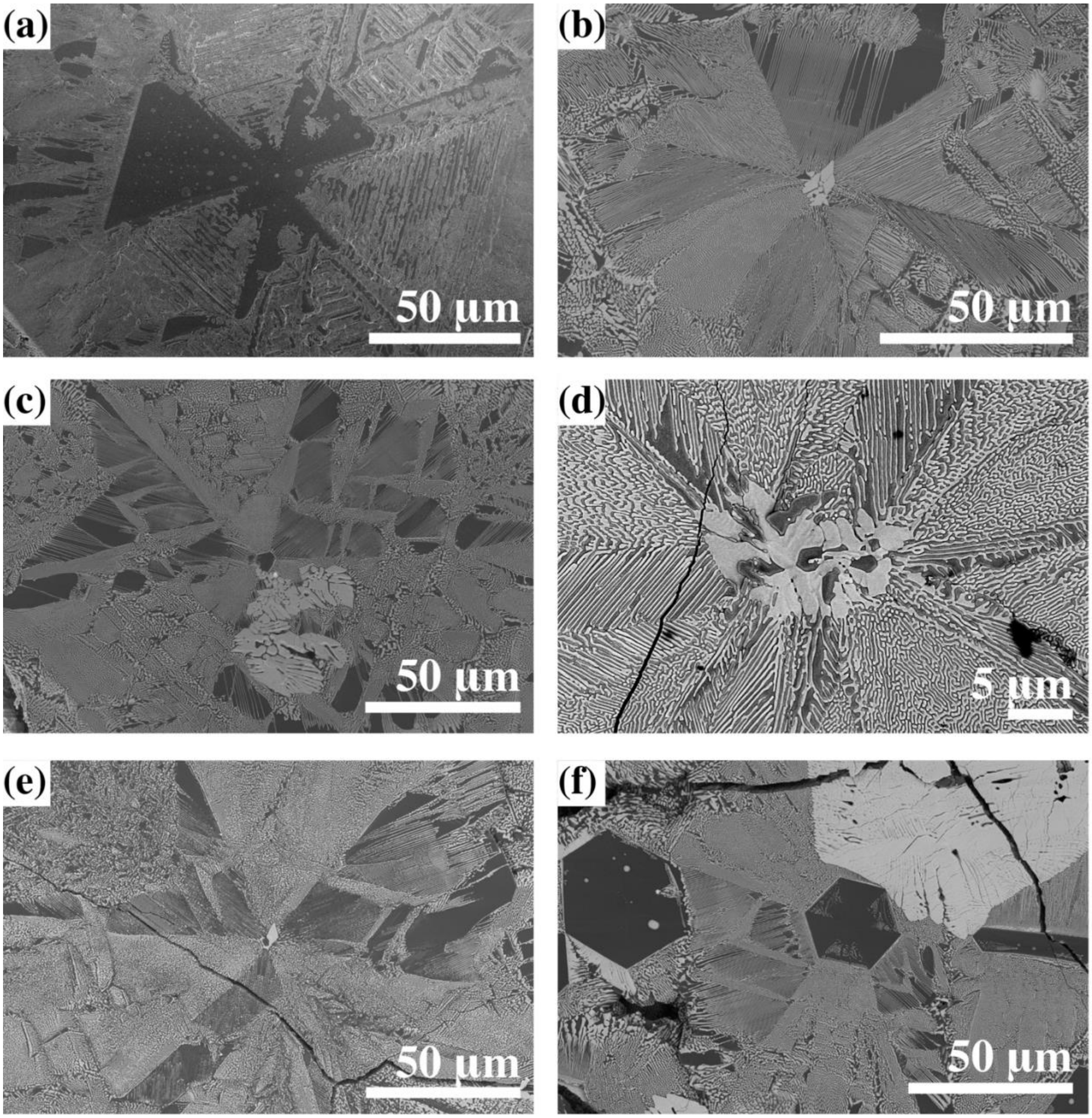

Figure A.6 Eutectic microstructures showing a pattern similar to 3-fold symmetry, when a single crystal is at the center of the pattern. BSE images were obtained in the channeled region of 50-50% Al_2O_3-$LaPO_4$ samples flash sintered at 1450°C, 1100V, 25mA/mm^2, (a)-(d) held for 7.5 s, (e), (f) held for 12 s.

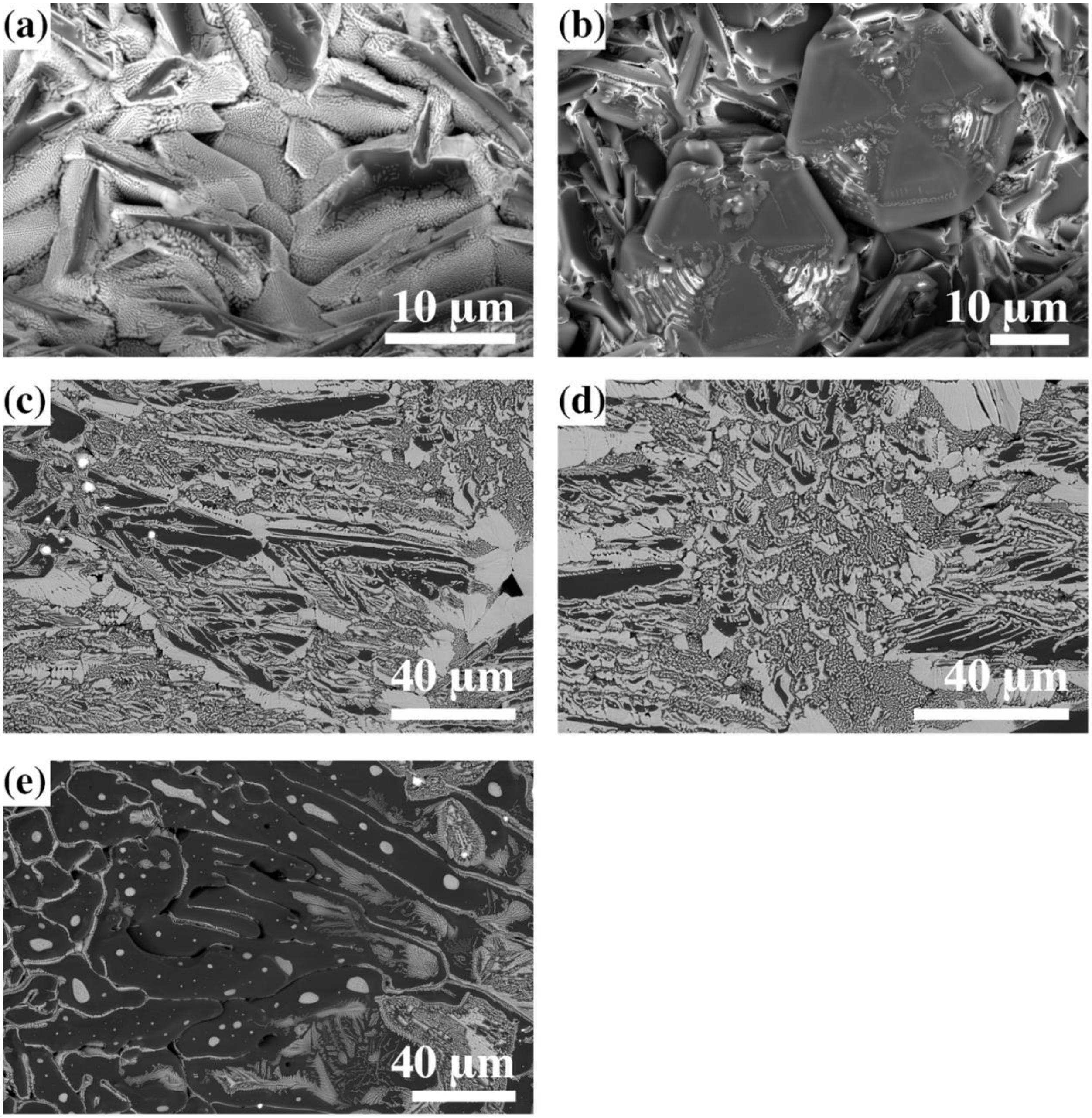

Figure A.7 Other microstructures observed with BSE in the various area of the channeled region of 75-25% Al_2O_3-$LaPO_4$ samples flash sintered at 1450°C, and held for 8 s, (a),(b) flashed with 850 V/cm, 5 mA/mm^2, (c)-(e) flashed with 950 V/cm, 25 mA/mm^2. Majority of the microstructure in the channeled region is similar to Figure 3.7 (b).

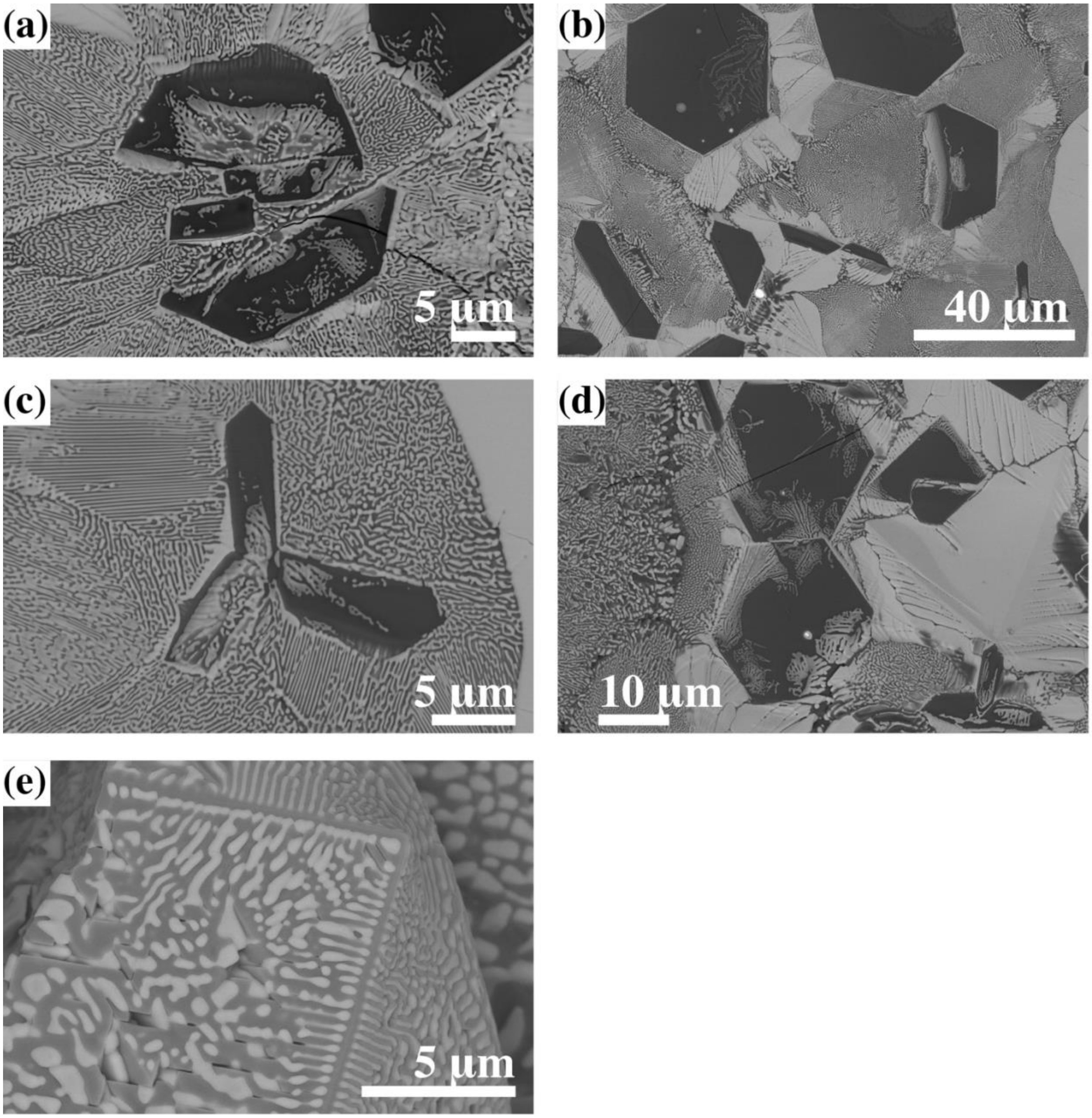

Figure A.8 Majority of the sapphire grains are hexagonal shaped, but there are some other morphologies that exist in the channeled region of flash sintered 50-50% Al_2O_3-$LaPO_4$ samples, as observed by BSE imaging. Flash sintering conditions are: (a) 1450°C, 950 V/cm, 25 mA/mm^2, 5.5 s, (b)-(d) 1450°C, 1050 V/cm, 15 mA/mm^2, 6 s, (e) 1450°C, 1100 V/cm, 25 mA/mm^2, 7.5 s.